

# Appendix C

## Fluid Flow Analyses

### Appendix C Abstract

This appendix documents four models that were used to evaluate the performance of the proposed WIPP shaft seal system design in terms of fluid-flow (gas and brine) within the seal system components and surrounding Disturbed Rock Zone (DRZ). The common hydrogeologic framework used by the models is described in terms of a radially symmetric system centered on the Air Intake Shaft and extending from the repository level upward through the Salado and Rustler Formations. Properties that govern fluid flow within porous media are defined for the seal system components, the host lithologic units, and the DRZ. Laboratory, field, and mechanical modeling studies are utilized to develop a conceptualization of the DRZ, which includes a time-varying permeability within the Salado Formation dependent on depth and rigidity of adjacent seal components. Model 1 is a completely saturated numerical flow model and is used to evaluate brine flow down the shaft from the Rustler Formation to the compacted salt column component during the 200-year period immediately after seal emplacement. Model 2 is a two-phase (gas and brine) numerical flow model used to evaluate gas flow up from the repository to the compacted salt column as well as pressure within the compacted salt column during the same 200-year period. A compacted salt reconsolidation submodel is incorporated, which predicts crushed salt permeability as a function of time, pressure, and depth within the column. Model 3 is a fully saturated numerical flow model and is used to evaluate brine flow upward within the seal system during the time period from 400 to 10,000 years after seal emplacement under ambient formation pressure conditions. Model 4 utilizes simple analytical relationships to analyze the potential brine flow through the shaft seals attributable to a range of nonhydrostatic natural head conditions between the Magenta and Culebra, the two primary water-bearing members of the Rustler Formation. The seal-system performance models were used to examine fluid-flow sensitivity to various assumptions of DRZ continuity, the existence of asphalt within concrete seal components, and different repository pressure loading scenarios.



Page intentionally blank.



## Contents

C1. INTRODUCTION.....	7
C2. DEFINITION OF PERFORMANCE MODELS.....	7
C3. HYDROGEOLOGIC FRAMEWORK.....	9
C3.1 Stratigraphy.....	9
C3.2 Observed Vertical Gradients.....	12
C3.3 Shaft Seal Material Properties.....	13
C3.3.1 Saturated Flow Parameters.....	15
C3.3.2 Two-Phase Flow Parameters.....	16
C3.4 Host-Rock Properties.....	17
C3.4.1 Permeability and Hydraulic Conductivity.....	17
C3.4.2 Porosity.....	23
C3.4.3 Formation Compressibility.....	23
C3.4.4 Two-Phase Properties of the Salado.....	24
C3.5 DRZ Properties.....	25
C3.5.1 Model for Calculating the Effective DRZ Permeability.....	27
C3.5.2 Model DRZ Effective Permeability.....	29
C4. FLOW DOWN FROM THE RUSTLER (MODEL 1).....	31
C4.1 Statement of Problem.....	31
C4.2 Performance Model 1 Description.....	31
C4.2.1 Conceptual Model and Assumptions.....	31
C4.2.2 Numerical Method.....	36
C4.2.3 Model Geometry and Boundary Conditions.....	36
C4.2.4 Model Parameters.....	45
C4.3 Performance Model Results.....	45
C5. GAS MIGRATION AND CONSOLIDATION OF COMPACTED SALT COLUMN (MODEL 2).....	53
C5.1 Statement of Problem.....	53
C5.2 Performance Model 2 Description.....	53
C5.2.1 Conceptual Model and Assumptions.....	53
C5.2.2 Numerical Model.....	55
C5.2.3 Model Geometry and Boundary Conditions.....	56
C5.2.4 Model Parameters.....	63
C5.3 Performance Model Results.....	63
C6.0 FLOW UP FROM THE SALADO (MODEL 3).....	72
C6.1 Statement of Problem.....	72
C6.2 Performance Model Description.....	73
C6.2.1 Conceptual Model and Assumptions.....	73
C6.2.2 Numerical Method.....	75
C6.2.3 Model Geometry and Boundary Conditions.....	75
C6.2.4 Model Parameters.....	76
C6.3 Performance Model Results.....	76
C7. INTRA-RUSTLER FLOW (MODEL 4).....	78



C7.1 Statement of Problem .....	78
C7.2 Performance Model Description .....	78
C7.2.1 Conceptual Model and Assumptions.....	78
C7.2.2 Analytical Approach .....	80
C7.2.3 Model Parameters.....	81
C7.3 Performance Model Results .....	83
C8. REFERENCES.....	88

## Figures

Figure C-1. AIS field permeability results.....	28
Figure C-2. Log-linear model for the calculation of an effective permeability of the DRZ.....	29
Figure C-3a. Full shaft model grid (top).....	37
Figure C-3b. Full shaft model grid (bottom).....	38
Figure C-4. Permeability fields for Run 1 (base case).....	46
Figure C-5. Permeability fields for Run 1 (base case).....	47
Figure C-6. Model 1 flow rates.....	48
Figure C-7. Cumulative flow at 200 years.....	50
Figure C-8. Pressure distributions for Run 1 (base case).....	51
Figure C-9. Pressure distributions for Run 1 (base case).....	52
Figure C-10. Conceptual diagram of compacted salt column performance model components.....	54
Figure C-11. Grid used by the compacted salt column performance model.....	57
Figure C-12. Two specifications of pressure at the base of the shaft.....	62
Figure C-13. Rate of change in log permeability (fractional density) with pressure and depth.....	64
Figure C-14. Reconsolidation surface for the best-fit permeability/fractional density predictor.....	65
Figure C-15. Calculated pressure versus time after seal emplacement at the top, middle, and bottom of the compacted salt column (base case).....	67
Figure C-16. Calculated salt column permeability versus elevation within the column for several times following seal emplacement (base case).....	68
Figure C-17. Calculated pressure versus time after seal emplacement at the top, middle, and bottom of the compacted salt column (Run 2).....	69
Figure C-18. Calculated salt column permeability versus elevation within the column for several times following seal emplacement (Run 2).....	70
Figure C-19. Pressure contours at 75 years for base case and for 95% permeability/fractional density predictor (Run 2).....	71
Figure C-20. Comparison of calculated pressure results for base case and continuous DRZ with no waterstops (Run 6).....	73
Figure C-21. Calculated salt column permeability versus elevation within the column for several times following seal emplacement (Run 6: Rustler flow included, continuous DRZ, no waterstops).....	74
Figure C-22. Cumulative gas flow from the repository to the compacted salt column.....	75



Figure C-23. Permeability fields for Runs 1 through 3 ( $t > 400$ years).....	77
Figure C-24. Intra-Rustler flow conceptual model.....	79
Figure C-25. Effect of an injection well on a unidirectional flow field.....	82
Figure C-26. Sensitivity of flow rate between Culebra and Magenta to head difference (base case).....	84
Figure C-27. Sensitivity of flow-field disturbance to head difference (base case).....	85
Figure C-28. Sensitivity of flow rate between Culebra and Magenta to DRZ radius (continuous DRZ).....	86
Figure C-29. Sensitivity of flow-field disturbance to DRZ radius (continuous DRZ).....	87

## Tables

Table C-1. Summary of Salado Stratigraphic Units Merged into Salado Model Combined Units.....	10
Table C-2. Freshwater Head Estimates in the Vicinity of the Air Intake Shaft.....	13
Table C-3. Bentonite Compacted Clay Parameters .....	13
Table C-4. Asphalt Parameters .....	14
Table C-5. Compacted-Salt Parameters .....	14
Table C-6. Concrete Parameters .....	14
Table C-7. Earthen Fill Parameters.....	15
Table C-8. Capillary Pressure and Relative Permeability Model Parameters for Compacted Clay, Concrete, Reconsolidated Salt, and Earthen Fill.....	15
Table C-9. Summary of Permeability and Hydraulic Conductivity, Porosity, and Compressibility for the Rustler Modeled Lithologic Units .....	18
Table C-10. Summary of Permeability and Hydraulic Conductivity, Porosity, and Compressibility for the Salado Modeled Lithologic Units .....	18
Table C-11. Testing and Analysis Summary for Salado Halite.....	19
Table C-12. Salado Brine Seepage Intervals <sup>(1)</sup> .....	20
Table C-13. Testing Summary for Rustler Formation.....	22
Table C-14. Summary of Literature Values for Formation Porosities.....	23
Table C-15. Salado Two-Phase Properties .....	25
Table C-16. Model DRZ permeability for base-case conceptualization (corrected for model DRZ area).....	32
Table C-17. Full-Shaft Model Vertical Layers.....	39
Table C-18. Full-Shaft Model Radial Gridding.....	43
Table C-19. Performance Model 1 Simulations .....	45
Table C-20. Vertical Layers of the Compacted Salt Column Performance Model .....	58
Table C-21. Compacted Salt Column Performance Model Radial Gridding .....	60
Table C-22. Compacted Salt Column Performance Model Simulations .....	66
Table C-23. Performance Model 3 Simulations .....	76
Table C-24. Comparison of Flow Rates Up the Shaft/DRZ from Simulations that Incorporate the Measured Pressure Conditions.....	78
Table C-25. Regional Darcy Velocities for Culebra and Magenta Members of the Rustler Formation.....	83



Page intentionally blank.



## C1. INTRODUCTION

This appendix describes analyses conducted to quantify the fluid-flow performance of the WIPP shaft seal system design. The appendix is organized in the following manner. First, the statements of the problems to be solved are developed. The problem statements are introduced in terms of performance models. The analysis sections of this appendix are organized in terms of these performance models. For each performance model, the conceptual model is described along with a description of the quantitative method used. Each performance calculation is defined in terms of the relevant assumptions, parameters, and boundary conditions. Finally, results from each performance model are presented. The numerical codes SWIFT II (Version 2F) and TOUGH28W (Version 2.02) have been used in this appendix to quantitatively analyze fluid-flow performance for the WIPP shaft seal system.

The fluid-flow analyses presented in this appendix were performed using SI units. Dimensions, parameter values, and performance model results will be presented in SI units. However, graphical depiction of the models used will be presented in terms of feet above mean sea level (ft msl) to facilitate comparisons with seal system design drawings.

## C2. DEFINITION OF PERFORMANCE MODELS

Evaluation of the fluid-flow performance of the shaft seal system is facilitated through definition of relevant performance models. Each performance model is derived from performance measures that quantify migration of fluids within and through the system. This approach differs in scope from that of the assessment of the WIPP repository. In the latter case, a general system model is developed in an iterative manner. Physical processes that may result in contaminant release are systematically identified and evaluated through results of the system model simulations. The performance models defined in this appendix are specific to performance measures applicable to the shaft seal system. These models were developed through assessment of the physical characteristics of the WIPP shaft sealing system, the surrounding media, and the sealing functions that are described in detail in Section 4 of the main report.

Qualitative design guidance has been developed for the shaft seal system based on the function of the shaft seal system. This guidance seeks (1) to limit the migration of radiological or other hazardous constituents from the repository horizon to the regulatory boundary over a 10,000-year regulatory period and (2) to limit groundwater flow into and through the shaft sealing system. Additional qualitative design guidance arises from special requirements of the compacted salt column. The salt column requires reconsolidation, a process that can be adversely affected by significant pore pressures within the column. This guidance seeks (3) to limit both groundwater and repository-generated gas from flowing into the compacted salt column.

The primary potential source of significant groundwater flow to the shaft sealing system comes from the Rustler Formation. Because of the low permeability of the Salado Formation, it is isolated from active groundwater circulation. However, because the Salado is significantly over-pressured relative to the Rustler Formation (Beauehim et al., 1993), the Salado Formation



represents a possible source of long-term upward flow from the repository horizon through the seal system.

The motivations for limiting brine migration in the seal system are: (1) to limit brine migration from the Rustler to the repository during repressurization of the seal system; (2) to prevent significant pore pressures from building in the compacted salt column and potentially affecting reconsolidation; (3) to limit the interconnection of water-bearing strata in the Rustler; and (4) to limit brine migration upward from the Salado. Likewise, the motivations for limiting gas and brine migration up the seal system from the repository are: (5) to limit upward fluid flow to the accessible environment; and (6) to prevent significant pore pressures from building in the compacted salt column.

These motivations, together with the features and processes that underlie them, can be synthesized into four flow-performance models:

Model 1: Flow Down from the Rustler

Model 2: Gas Migration and Compacted Salt Column Consolidation

Model 3: Flow up from the Salado

Model 4: Intra-Rustler Flow

These performance models are coupled or interdependent. For example, flow from the Rustler (Model 1) could be affected by the consolidation (permeability) of the compacted salt column (Model 2). Likewise, Model 2 performance could be affected by the flow from the Rustler (Model 1). Model 1 will be evaluated first, followed by the analysis of Model 2. Models 3 and 4 will be evaluated separately.

Several analysis assumptions are shared among all the performance models and are listed below.

- Each analysis uses the Air Intake Shaft (AIS) as the shaft analyzed. It is assumed that the AIS analysis is representative of the three other WIPP shafts.
- The stratigraphy used in these performance calculations is consistent with the AIS stratigraphy as presented by Holt and Powers (1990) and as summarized by DOE (1995).
- A radial model geometry is assumed.
- Isothermal conditions are considered. This means that fluid flow driven by temperature gradients is assumed to be negligible.
- Each shaft can be considered independently. This means that it is assumed that no hydraulic interference exists between shafts.
- Flow is considered through the intact rocks, the seal materials, and the disturbed rock zone (DRZ).
- The DRZ can appropriately be described as having its largest permeability at the shaft/DRZ contact and approaching intact permeabilities at its outer extent. The permeability is assumed to vary log-linearly from the shaft/DRZ interface to the outer extent of the DRZ (intact rock).



- For Models 1 and 2, a preclosure period of 50 years is assumed. During the preclosure period, the shaft is held at atmospheric conditions.

The analyses presented in this appendix are deterministic and do not account for the full-range of potential outcomes that may be expected by performing a stochastic analysis allowing parameters to randomly vary across their respective uncertainty ranges. A stochastic analysis of the complete disposal system was conducted by WIPP PA for the 40 CFR 191 Compliance Certification Application of the WIPP (DOE, 1996). This analysis addressed the ranges of seal system parameters as applicable to the behavior of the disposal system. The analyses presented in this report address those parameters that are considered the most uncertain and to which the primary performance measures (flow rates) are most sensitive. These parameters include (1) the permeability of the DRZ, (2) the relationship between compacted salt density and permeability, and (3) the repository gas pressure applied at the base of the shaft seal system. The prediction of brine-flow migration down the shaft system (Model 1) is performed with a saturated flow model, which estimates the flow. In addition, a limited sensitivity analysis was performed, which provided a range in model predictions for variations in what are considered to be important processes. These processes are incorporated in model parameters that address (1) the vertical continuity of the DRZ, (2) the healing rate against the concrete-asphalt waterstops, (3) the relationship between compacted salt density and permeability, and (4) the repository gas pressure applied at the base of the shaft sealing system.

### **C3. HYDROGEOLOGIC FRAMEWORK**

This section discusses the hydrogeologic framework for the hydraulic analysis of the performance of the WIPP shaft seal system. The hydrogeologic framework includes (1) the stratigraphy of the host rocks and how it is conceptualized for the performance models; (2) the ambient fluid pressure profile within the host rocks; (3) and the hydraulic parameters describing the seal system, the host rocks, and the DRZ.

The properties that govern fluid flow within porous media are defined for the seal components, the host lithologic units, and the DRZ. Both single-phase (SWIFT II) and multi-phase (TOUGH28W) fluid flow codes were used in these calculations.

#### **C3.1 Stratigraphy**

The stratigraphy of the host rocks adjacent to the shaft from the repository horizon to the surface is composed of the Salado Formation, the Rustler Formation, the Dewey Lake Redbeds, and the surficial Santa Rosa and Gatuña Formations. Dune sand and caliche overlie the sediments at the surface. The primary water-bearing strata are confined to the Rustler and Salado Formations. Therefore, the discussion of stratigraphy will focus on the Salado and Rustler Formations.

The reference stratigraphy used to develop the performance models in this appendix is based on the shaft mapping of the AIS (Holt and Powers, 1990). The detailed stratigraphy of the Rustler and Salado Formations in the AIS is also summarized in Appendix A of DOE (1995). The detailed stratigraphy will not be discussed here.



The detailed modeling of the discrete stratigraphy present in the Rustler and Salado formations presents a challenge. Several Salado marker beds are very thin, with thicknesses less than 0.5 m in many instances. To reduce the total number of grid cells to a manageable level in the performance models, several individual stratigraphic units were merged into single model combined units. Units were merged together based on proximity, thickness, and lithology. Table C-1 lists the Salado Formation combined units and the individual beds that were merged to form them. Rock properties of the combined stratigraphic units were calculated based on the thickness-weighted arithmetic mean of the rock properties of individual beds composing the combined units. DRZ permeabilities of the combined stratigraphic units were calculated based on the thickness-weighted harmonic mean.

Table C-1. Summary of Salado Stratigraphic Units Merged into Salado Model Combined Units

Combined Unit Name	Combined Unit Thickness (m)	Stratigraphic Unit	Rock Type	Individual Unit Thickness (m)
Unit 1	5.79	MB103	Anhydrite <sup>(1)(2)</sup>	5.03
		MB104	Anhydrite	0.30
		MB105	Anhydrite	0.30
		MB106	Anhydrite	0.15
Unit 2	8.05	MB107	Polyhalite	0.15
		MB108	Polyhalite	0.15
		MB109	Anhydrite <sup>(1)(2)</sup>	7.74
Unit 3	3.57	MB110	Polyhalite	0.34
		MB111	Polyhalite	0.18
		MB112	Polyhalite	0.61
		MB113	Polyhalite	0.30
		MB114	Polyhalite	0.30
		MB115	Polyhalite	1.07
Unit 4	5.79	MB116	Polyhalite	0.76
		MB117	Polyhalite	0.46
		MB118	Polyhalite	0.79
		MB119	Polyhalite	0.61
		MB120	Polyhalite	0.27
		Zone A	Halite <sup>(1)</sup>	3.05

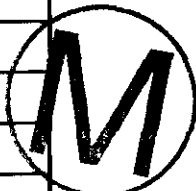


Table C-1. Summary of Salado Stratigraphic Units Merged into Salado Model Combined Units

Combined Unit Name	Combined Unit Thickness (m)	Stratigraphic Unit	Rock Type	Individual Unit Thickness (m)
		MB121	Polyhalite	0.30
		MB122	Polyhalite	0.30
Unit 5	4.72	MB123	Anhydrite	1.98
		MB124	Anhydrite <sup>(1)</sup>	2.74
Unit 6	3.96	Zone B	Halite <sup>(1)</sup>	0.91
		Zone C	Halite <sup>(1)</sup>	2.74
		MB126	Polyhalite	0.30
Unit 7	11.83	MB127	Polyhalite	0.79
		MB128	Polyhalite	1.07
		Zone D	Halite <sup>(1)</sup>	3.20
		Zone E	Halite <sup>(1)</sup>	0.61
		Zone F	Halite <sup>(1)</sup>	0.91
		Zone G	Halite <sup>(1)</sup>	0.61
		Zone H	Halite <sup>(1)</sup>	1.80
		MB129	Polyhalite <sup>(1)</sup>	0.46
		Zone I	Halite <sup>(1)</sup>	1.74
		MB130	Polyhalite	0.64
Unit 8	2.29	MB131	Polyhalite	0.30
		Zone J	Halite <sup>(1)</sup>	1.22
		MB132	Polyhalite	0.30
		MB133	Polyhalite	0.46
Unit 9	4.75	Unnamed	Anhydrite	0.76
		MB134	Anhydrite <sup>(2)</sup>	3.69
		MB135	Anhydrite	0.30

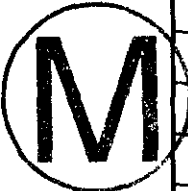


Table C-1. Summary of Salado Stratigraphic Units Merged into Salado Model Combined Units

Combined Unit Name	Combined Unit Thickness (m)	Stratigraphic Unit	Rock Type	Individual Unit Thickness (m)
Unit 10		MB136	Anhydrite <sup>(2)</sup>	4.30
		MB137	Anhydrite	0.40
Unit 11	0.49	MB138	Anhydrite	0.18
		Anhydrite A	Anhydrite	0.30

- (1) Identified brine seepage interval.  
 (2) Anhydrite unit greater than 3 m in thickness.

### C3.2 Observed Vertical Gradients

Heads within the Rustler and between the Rustler and Salado formations are not in hydrostatic equilibrium. Mercer (1983) recognized that heads at the Rustler/Salado transition (referred to as the brine aquifer and not present in the vicinity of the WIPP shafts) indicate an upward hydraulic gradient from that zone to the Culebra. Later, with the availability of more head measurements within the Salado and Rustler, Beauheim (1987) provided additional insight into the potential direction of vertical fluid movement within the Rustler. He reported that the hydraulic data indicate an upward gradient from the Salado to the Rustler.

Formation pressures in the Salado Formation have been decreased in the near vicinity of the WIPP underground facility. The highest, and thought to be least disturbed, estimated formation fluid pressure from hydraulic testing is 12.55 MPa estimated from interpretation of testing within borehole SCP01 in MB139 just below the underground facility horizon (Beauheim et al., 1993). The freshwater head within MB139, based on the estimated static formation pressure of 12.55 MPa, is 1663.6 m (5458 ft) above mean sea level (msl).

Heads in the Rustler have also been impacted by the presence of the WIPP shafts. These impacts in the Culebra were significant in the 1980s, with a large drawdown cone extending away from the shafts in the Culebra (Haug et al., 1987). The undisturbed head of the Rustler/Salado contact in the vicinity of the AIS is estimated to be approximately 936.0 m (3071 ft) msl (Brinster, 1991). The undisturbed head in the Culebra is estimated to be approximately 926.9 m (3041 ft) msl in the vicinity of the AIS (LaVenue et al., 1990). The undisturbed head in the Magenta is estimated to be approximately 960.1 m (3150 ft) msl (Brinster, 1991).

The disturbed and undisturbed heads in the Rustler are summarized in Table C-2. Also included is the freshwater head of MB139 based on hydraulic testing in the WIPP underground. Consistent with the vertical flow directions proposed by previous investigators, estimated vertical gradients in the vicinity of the AIS before the shafts were drilled indicate a hydraulic gradient from the Magenta to the Culebra and from the Rustler/Salado contact to the Culebra. There is also the potential for flow from the Salado Formation to the Rustler Formation.



Table C-2. Freshwater Head Estimates in the Vicinity of the Air Intake Shaft

Hydrologic Unit	Freshwater Head (m asl)		Reference
	Undisturbed	Disturbed	
Magenta Member	960.1 <sup>(1)</sup>	948.8 <sup>(2)</sup>	Brinster (1991)
		(H-16)	Beauheim (1987)
Culebra Member	926.9 <sup>(1)</sup>	915.0 <sup>(2)</sup>	LaVenue et al. (1990)
		(H-16)	Beauheim (1987)
Lower Unnamed Member	—	953.4 <sup>(2)</sup>	Beauheim (1987)
		(H-16)	
Rustler/Salado Contact	936.0 - 940.0 <sup>(1)</sup>	—	Brinster (1991)
Salado MB139	1663.6 <sup>(2)</sup>	—	Beauheim et al. (1993)

- (1) Estimated from contoured head surface plot based primarily on well data collected before shaft construction.  
 (2) Measured through hydraulic testing and/or long-term monitoring.



### C3.3 Shaft Seal Material Properties

The WIPP shaft seal system is composed of four primary materials: compacted clay, compacted salt, salt-saturated concrete, and asphalt. Eathern fill material is specified for the shafts in the near-surface regions. The performance models described in Section 2 require quantitative values for certain properties of the seal materials. These properties may be broadly divided into two categories: saturated flow parameters and two-phase flow parameters. Saturated flow parameters include intrinsic permeability, porosity, and compressibility of the materials, as well as the initial pore pressure of the components. Necessary parameters for two-phase flow will depend on the selection of an appropriate conceptual model for two-phase flow. The following sections describe the process used in the selection of saturated and two-phase flow parameters for the performance models presented in Sections C4, C5, and C6. Values for these parameters are summarized in Tables C-3 through C-8.

Table C-3. Bentonite Compacted Clay Parameters

Parameter	Value
Intrinsic Permeability (m <sup>2</sup> )	5×10 <sup>-19</sup>
Porosity (m <sup>3</sup> /m <sup>3</sup> )	0.24
Pore compressibility (1/Pa)	
Upper Salado clay	1.81×10 <sup>-9</sup>
Lower Salado clay	1.59×10 <sup>-9</sup>
Rustler clay column	1.96×10 <sup>-9</sup>
Initial Pressure (Pa)	101356.5
Initial Water Saturation	0.79

Table C-4. Asphalt Parameters

Parameter	Value
Intrinsic Permeability (m <sup>2</sup> )	1×10 <sup>-20</sup>
Porosity (m <sup>3</sup> /m <sup>3</sup> )	0.01
Pore compressibility (1/Pa)	2.97×10 <sup>-8</sup>
Initial Pressure (Pa)	101356.5
Initial Water Saturation	0.0

Table C-5. Compacted Salt Parameters

Parameter	Value
Intrinsic Permeability (m <sup>2</sup> )	7.9×10 <sup>-13</sup> to 6.3×10 <sup>-21</sup> (1)
Porosity (m <sup>3</sup> /m <sup>3</sup> )	0.05
Pore compressibility (1/Pa)	8.5×10 <sup>-10</sup>
Initial Pressure (Pa)	101356.5
Initial Water Saturation	0.32

(1) Section C5.3.

Table C-6. Concrete Parameters

Parameter	Value
Intrinsic Permeability (m <sup>2</sup> )	
0 to 400 years	1.78×10 <sup>-19</sup>
400 to 10000 years	1.0×10 <sup>-14</sup>
Porosity (m <sup>3</sup> /m <sup>3</sup> )	0.0227
Pore compressibility (1/Pa)	2.64×10 <sup>-9</sup>
Initial Pressure (Pa)	101356.5
Initial Water Saturation	1.0



Table C-7. Earthen Fill Parameters

Parameter	Value
Intrinsic Permeability (m <sup>2</sup> )	1×10 <sup>-14</sup>
Porosity (m <sup>3</sup> /m <sup>3</sup> )	0.32
Pore compressibility (1/Pa)	3.1×10 <sup>-8</sup>
Initial Pressure (Pa)	101356.5
Initial Water Saturation	0.8

Table C-8. Capillary Pressure and Relative Permeability Model Parameters for Compacted Clay, Concrete, Reconsolidated Salt, and Earthen Fill

Parameter	Value
Threshold Pressure (Pa)	$P_t = 5.6 \times 10^{-7} k^{-0.346}$
Lambda ( $\lambda$ )	0.94
Residual Water Saturation	0.2
Residual Gas Saturation	0.2

### C3.3.1 Saturated Flow Parameters

The simplest approximation of flow can be derived from Darcy's Law, an empirical relationship that demonstrates that flow through a porous material depends directly on the hydraulic gradient, fluid viscosity, and material permeability. The hydraulic gradient will depend on the physical system, as will fluid viscosity. For an engineered system such as the WIPP shaft sealing system, it is possible to limit flow by specifying very low material permeabilities. It is recognized that fluid flow through the WIPP shaft sealing system is complex and that a simple Darcy flow analysis will not suffice. Nonetheless, the importance of seal material permeability and the ability to engineer low-permeability materials can be justifiably retained in the performance analysis of the seal system. The specifications for seal materials are discussed in considerable detail in Appendix A. The analyses presented in this appendix focus on the expected behavior of the seal system within the context of each performance model. Because of uncertainty in the consolidation process for crushed salt, deterministic calculations are presented that capture this uncertainty. In all other cases, the selected permeability reflects confidence that the seal components will be constructed in a manner consistent with the specifications put forth in Appendix A. The most probable value for each material permeability was used for the analyses, except as noted otherwise in the text.

Unlike TOUGH28W, SWIFT II requires input of hydraulic conductivity rather than intrinsic permeability. The conversion from permeability to hydraulic conductivity in this report



will use a fluid density of  $1230 \text{ kg/m}^3$ , an acceleration of gravity of  $9.792 \text{ m/s}^2$ , and a fluid viscosity of  $1.8 \times 10^{-3} \text{ Pa} \cdot \text{s}$ . These fluid properties are representative of a WIPP saturated brine.

Material porosity and compressibility relate to the storage capacity of a porous media. Sensitivity studies conducted previously (WIPP PA, 1992–1993) have demonstrated that fluid flow is not significantly impacted by material storage capacity. With the exception of the crushed salt column permeability, the performance measures identified for the shaft seal system relate to fluid flow. As discussed in the previous paragraphs, the uncertainty in the salt column consolidation process is addressed in the relevant performance model. Variations in seal material porosity and compressibility were not included in these analyses. The most probable values for these parameters were selected for use in the performance models (DOE, 1996).

The pressure in the open shafts is atmospheric. It was assumed that the initial pore pressure for all seal materials was also atmospheric. Values for the saturated flow parameters and initial conditions for all seal materials are presented in Tables C-3 through C-7. These values are consistent with the most probable values listed in Appendix PAR of the WIPP Compliance Certification Application (DOE, 1996). Additional details regarding the uncertainty in these parameters are presented as appropriate later in the text.

### **C3.3.2 Two-Phase Flow Parameters**

Two conditions necessitate consideration of two-phase flow within the shaft seal system. The first is that the seal system will be partially saturated with respect to brine at the time of construction. The second relates to the possibility that gas will be generated by the waste forms, and this gas could migrate to the base of the sealed shafts. Modeling a system that has two phases requires knowledge of the two-phase properties, which are characterized by capillary pressure and relative permeability curves for each phase. Ideally, each material will have a set of characteristic curves derived from experimental data. In practice, however, these curves rarely exist for the precise materials being modeled. The curves can be estimated using functional relationships found in the literature (Brooks and Corey, 1966; van Genuchten, 1980; Parker et al., 1987). Webb (1996) performed a literature review of the relationships for determining two-phase characteristic curves. Based on those comparisons, he concluded that no single model best fits all the data, and he further recommended the use of two models for future modeling activities at the WIPP. He referred to these two models as the mixed Brooks and Corey model and the van Genuchten/Parker model. The van Genuchten/Parker model was implemented in the two-phase calculations presented in this appendix.

Based on literature searches, two-phase parameters for the Brooks and Corey model were derived. These parameters were applied to all seal materials, with the exception of asphalt. Parameters necessary for the van Genuchten/Parker model can be derived from those specified for the Brooks and Corey model. The necessary parameters are the threshold pressure, pore size distribution index ( $\lambda$ ), residual water saturation, and residual gas saturation. An empirically derived relationship between threshold pressure and permeability (Davies, 1991) is used for determining the threshold pressure. The values used for two-phase flow parameters are summarized in Table C-8.



The initial saturation condition must also be specified for the seal system. The initial liquid saturation state is derived from the following relationship:

$$S = w\gamma \frac{(1 - \phi)}{\phi} \quad (C-1)$$

where

- $S$  = the liquid saturation
- $\gamma$  = the specific gravity of the material
- $w$  = the moisture content of the material
- $\phi$  = the material porosity.

For all materials, the liquid was assumed to be brine. Porosity and moisture content are engineered parameters specified for each material (DOE, 1996).

The capillary pressure model for asphalt is the only exception to the parameters described above. Asphalt is a hydrophobic material. Using the parameters described for other seal materials and the low brine saturation of the asphalt, this seal component would develop a large suction pressure, attracting water. This behavior is not consistent with a hydrophobic material. Therefore, a linear capillary model is assumed for the asphalt. The model is defined by a zero capillary pressure at all brine saturations.

### **C3.4 Host-Rock Properties**

Because the permeability (or hydraulic conductivity) of the host-rock formations is the most important parameter characterizing the host formations, emphasis will be given to it. Porosity and compressibility used for each rock type will be summarized in tables, but discussion of these parameters and their sources will be limited.

#### **C3.4.1 Permeability and Hydraulic Conductivity**

The following sections discuss the permeability and hydraulic conductivity of the Salado evaporites and each member of the Rustler Formation. The values assumed for both the undisturbed and disturbed formation are presented. Tables C-9 and C-10 summarize the values of permeability and hydraulic conductivity for the Rustler and Salado Formations.

The reported disturbed formation permeabilities represent the permeability of the DRZ at the shaft/DRZ interface. These permeabilities will later be used to calculate the effective DRZ permeability.



Table C-9. Summary of Permeability and Hydraulic Conductivity, Porosity, and Compressibility for the Rustler Modeled Lithologic Units

Lithology	Undisturbed Permeability (m <sup>2</sup> )	Undisturbed Hydraulic Conductivity (m/s)	Disturbed Permeability (m <sup>2</sup> )	Disturbed Hydraulic Conductivity (m/s)	Porosity (fraction)	Rock Compressibility (Pa <sup>-1</sup> )	Pore-Volume Compressibility (Pa <sup>-1</sup> )
Anhydrite <sup>(1)</sup>	1.00×10 <sup>-19</sup>	6.69×10 <sup>-13</sup>	1.00×10 <sup>-19</sup>	6.69×10 <sup>-13</sup>	0.01	2.2×10 <sup>-11</sup>	2.2×10 <sup>-9</sup>
Mudstone 4	3.89×10 <sup>-16</sup>	2.60×10 <sup>-9</sup>	3.89×10 <sup>-13</sup>	2.60×10 <sup>-6</sup>	0.30	9.8×10 <sup>-10</sup>	3.3×10 <sup>-9</sup>
Magenta	1.49×10 <sup>-15</sup>	1.00×10 <sup>-8</sup>	1.49×10 <sup>-14</sup>	1.00×10 <sup>-7</sup>	0.16	1.1×10 <sup>-9</sup>	6.9×10 <sup>-9</sup>
Mudstone 3	1.49×10 <sup>-19</sup>	1.00×10 <sup>-12</sup>	1.49×10 <sup>-16</sup>	1.00×10 <sup>-9</sup>	0.30	9.8×10 <sup>-10</sup>	3.3×10 <sup>-9</sup>
Culebra	2.09×10 <sup>-14</sup>	1.40×10 <sup>-7</sup>	2.09×10 <sup>-13</sup>	1.40×10 <sup>-6</sup>	0.16	1.1×10 <sup>-9</sup>	6.9×10 <sup>-9</sup>
Anhydrite 1/ Mudstone 1	1.00×10 <sup>-19</sup>	6.69×10 <sup>-13</sup>	1.00×10 <sup>-19</sup>	6.69×10 <sup>-13</sup>	0.05	200×10 <sup>-11</sup>	4.5×10 <sup>-10</sup>
Transition/ Bioturbated Clastics	2.24×10 <sup>-18</sup>	1.50×10 <sup>-11</sup>	2.24×10 <sup>-15</sup>	1.50×10 <sup>-8</sup>	0.20	7.9×10 <sup>-11</sup>	3.9×10 <sup>-10</sup>

(1) Anhydrite 5, Anhydrite 4, Anhydrite 3, and Anhydrite 2.

Table C-10. Summary of Permeability and Hydraulic Conductivity, Porosity, and Compressibility for the Salado Modeled Lithologic Units

Lithology	Undisturbed Permeability (m <sup>2</sup> )	Undisturbed Hydraulic Conductivity (m/s)	Disturbed Permeability (m <sup>2</sup> )	Disturbed Hydraulic Conductivity (m/s)	Porosity (fraction)	Rock Compressibility (Pa <sup>-1</sup> )	Pore-Volume Compressibility (Pa <sup>-1</sup> )
Anhydrite >3 m thick	1.00×10 <sup>-19</sup>	6.69×10 <sup>-13</sup>	1.00×10 <sup>-19</sup>	6.69×10 <sup>-13</sup>	0.01	2.23×10 <sup>-11</sup>	2.23×10 <sup>-9</sup>
Anhydrite <3 m thick	1.00×10 <sup>-19</sup>	6.69×10 <sup>-13</sup>	1.00×10 <sup>-15</sup>	6.69×10 <sup>-9</sup>	0.01	2.23×10 <sup>-11</sup>	2.23×10 <sup>-9</sup>
Halite	1.00×10 <sup>-21</sup>	6.69×10 <sup>-15</sup>	1.00×10 <sup>-15</sup>	6.69×10 <sup>-9</sup>	0.01	8.05×10 <sup>-11</sup>	8.05×10 <sup>-9</sup>
Polyhalite	3.00×10 <sup>-21</sup>	2.01×10 <sup>-14</sup>	1.00×10 <sup>-15</sup>	6.69×10 <sup>-9</sup>	0.01	2.23×10 <sup>-11</sup>	2.23×10 <sup>-9</sup>
Vaca Triste	1.49×10 <sup>-19</sup>	1.00×10 <sup>-12</sup>	1.49×10 <sup>-16</sup>	1.00×10 <sup>-9</sup>	0.20	6.6×10 <sup>-10</sup>	3.3×10 <sup>-9</sup>



## Salado Formation

Table C-11 summarizes testing and analysis of test data for the Salado halite. In this appendix, the permeability of the undisturbed halite is assumed to have a value of  $1 \times 10^{-21} \text{ m}^2$ , and the permeability of the disturbed halite is assumed to have a value of  $1 \times 10^{-15} \text{ m}^2$ . The permeability for undisturbed halite is consistent with the cumulative probability distribution for the permeability of far field and depressurized halite given in Gorham et al. (1992). The permeability for disturbed halite was selected based on the probability density function for disturbed halite recommended to PA and included in Appendix D of this document. The basis for the disturbed halite permeability values is derived from field tests within the AIS (Dale and Hurtado, 1996) and other field test programs (Knowles et al., 1996; Stormont, 1990), which are discussed in Section C3.5. The disturbed halite distribution function recommended to PA is log-triangular with a maximum of  $1 \times 10^{-14} \text{ m}^2$  ( $6.7 \times 10^{-8} \text{ m/s}$ ) and a minimum of  $1 \times 10^{-17} \text{ m}^2$ . The permeability of  $1 \times 10^{-15} \text{ m}^2$  is consistent with the Salado disturbed permeability for halite previously used by PA.

The median permeability for undisturbed anhydrite, based on borehole testing, was  $1.0 \times 10^{-19} \text{ m}^2$  (DOE, 1996). The value for the disturbed permeability of the Salado anhydrites was assumed to be  $1 \times 10^{-15} \text{ m}^2$ , which is consistent with the disturbed anhydrite permeability reported by Sandia WIPP Project (WIPP PA, 1992–1993).

The undisturbed polyhalite permeability of  $3.0 \times 10^{-21} \text{ m}^2$  was taken from Lappin et al. (1989) and Saulnier and Avis (1988). Because there was no specific information concerning polyhalite disturbed permeability, it was assumed to be the same as that for halite and anhydrite.

Table C-11. Testing and Analysis Summary for Salado Halite

Lithology	Reference(s)	Permeability ( $\text{m}^2$ )	Hydraulic Conductivity (m/s)	Comments
Undisturbed Halite	Beauheim et al., 1991 Beauheim et al., 1993	$3 \times 10^{-18} - 10^{-21}$	$2 \times 10^{-11} - 6.7 \times 10^{-15}$	Underground testing at the WIPP from 1988 to 1992
	Gorham et al., 1992	$10^{-19} - 10^{-24}$	$6.9 \times 10^{-13} - 6.7 \times 10^{-18}$	Values recommended for PA calculation
Disturbed Halite	Gorham et al., 1992	$10^{-13} - 10^{-18}$	$6.7 \times 10^{-7} - 6.7 \times 10^{-12}$	Values recommended for 1992 PA calculation
	WIPP PA, 1992–1993	$10^{-15} - 10^{-22}$	$6.9 \times 10^{-9} - 6.7 \times 10^{-16}$	Range used for 1992 PA calculations
	Dale and Hurtado, 1996	$10^{-14} - 10^{-17}$	$6.9 \times 10^{-8} - 6.7 \times 10^{-11}$	Testing in the AIS during 1995

The lithology of the Vaca Triste is a halitic siltstone and mudstone. No hydraulic conductivity information was available for the Vaca Triste. In the absence of any specific information, the undisturbed permeability and the disturbed permeability for the Vaca Triste were assumed to be  $1.49 \times 10^{-19} \text{ m}^2$  ( $1.0 \times 10^{-12} \text{ m/s}$ ) and  $1.49 \times 10^{-16} \text{ m}^2$  ( $1.0 \times 10^{-9} \text{ m/s}$ ), respectively. These values are the same as those used for Mudstone 3 in the Rustler, which has a similar lithology.

Within the Salado formation, several brine seepage intervals were noted. Permeabilities for these zones were assigned values of 10 times the base value for each rock type. Porosities and compressibilities were not modified for the brine seepage zones. Table C-12 identifies which Salado stratigraphic units were treated as brine seepage intervals.

Table C-12. Salado Brine Seepage Intervals<sup>(1)</sup>

Stratigraphic Unit
Marker Bed 103
Marker Bed 109
Vaca Triste
Zone A
Marker Bed 121
Union Anhydrite
Marker Bed 124
Zone B
Zone C
Zone D
Zone E
Zone F
Zone G
Zone H
Marker Bed 129
Zone I
Zone J

(1) After US DOE, 1995.



### Rustler Formation

The Rustler Formation consists of five members, which from the oldest to youngest are: the unnamed lower member, the Culebra Dolomite Member, the Tamarisk Member, the Magenta Dolomite Member, and the Forty-niner Member. Many of the members are composed of informal lithologic units. The lower unnamed member has been hydraulically tested in the

vicinity of the AIS (see Table C-13) Because the tests reported in Beauheim (1987) most likely tested the most transmissive portions of the unnamed lower member (i.e., the transition and bioturbated clastic zones), the maximum measured hydraulic conductivity of  $1.5 \times 10^{-11}$  m/s was selected as the hydraulic conductivity for the transition and bioturbated zones units. The lower permeability units of the unnamed lower member, Anhydrite 1 and Mudstone 1, were assigned a permeability consistent with the anhydrite permeability of  $1.0 \times 10^{-19}$  m<sup>2</sup>. Mudstone 2, which underlies the Culebra, was tested in H-16 in the test interval that included the Culebra (Beauheim, 1987). For this reason, the model considers Mudstone 2 and the Culebra as a single unit. The hydraulic conductivity of this unit is discussed with the Culebra.

A disturbed permeability  $2.24 \times 10^{-15}$  m<sup>2</sup> was selected for the bioturbated clastic zone and the transition zone. This value represents a three order of magnitude increase in hydraulic conductivity over the undisturbed value. A disturbed permeability of  $1.0 \times 10^{-15}$  m<sup>2</sup> was assigned to Anhydrite 1 and Mudstone 1, which were considered as a single unit in the model. Rock mechanics calculations presented in Appendix D of this report evaluate DRZ development in the clay units of the Rustler Formation.

The hydraulic conductivity of the Culebra dolomite varies over a wide range (four orders of magnitude) at the WIPP site. This wide variation is due to the presence of both open and filled fractures within the Culebra. The hydraulic conductivity is lowest in regions where the fractures in the Culebra are filled and highest in regions where the fractures are open. The location of the WIPP shafts is in a region of relatively lower hydraulic conductivity.

A value of  $2.09 \times 10^{-14}$  m<sup>2</sup> was selected as the permeability for the Culebra. This value represents the highest site-specific hydraulic conductivity estimated from testing the Culebra in the vicinity of the AIS. The disturbed permeability for the Culebra was assigned a value of  $2.09 \times 10^{-13}$  m<sup>2</sup>. Mechanical calculations presented in Appendix D predict that Rustler dolomites will not develop a DRZ.

The Tamarisk Member of the Rustler Formation includes Anhydrite 2, which directly overlies the Culebra, Mudstone 3, and Anhydrite 3, which underlies the Magenta. Hydraulic testing of the Tamarisk was attempted at H-16 adjacent to the AIS but was unsuccessful (Beauheim, 1987). It was estimated that the transmissivity of the Tamarisk was one to two orders of magnitude lower than the least-transmissive unit successfully tested at H-16. This results in an estimated permeability ranging from  $4.63 \times 10^{-20}$  to  $4.63 \times 10^{-19}$  m<sup>2</sup>.

A value of  $1.0 \times 10^{-19}$  m<sup>2</sup> was selected for the undisturbed permeability of the anhydrite units (Anhydrite 3 and Anhydrite 2) of the Tamarisk. The value for the disturbed permeability of the anhydrite units was taken as  $1.0 \times 10^{-15}$  m<sup>2</sup>, which is consistent with the disturbed anhydrite permeability reported by Sandia WIPP Project (WIPP PA, 1992–1993). Rock mechanics calculations presented in Appendix D of this report predict that Rustler anhydrites do not develop a DRZ adjacent to the shaft. A value of  $1.49 \times 10^{-19}$  m<sup>2</sup> was selected for the undisturbed permeability of Mudstone 3, consistent with Brinster (1991). A disturbed permeability three orders of magnitude higher than the undisturbed value, or  $1.49 \times 10^{-16}$  m<sup>2</sup>, was assumed for Mudstone 3.



Table C-13. Testing Summary for Rustler Formation

Lithology	Reference(s)	Range (m <sup>2</sup> )	Conductivity (m/s)	Comments
Unnamed lower member: bioturbated clastic zone	Beauheim, 1987 Beauheim et al., 1993	$2.24 \times 10^{-18}$ – $1.84 \times 10^{-18}$	$1.5 \times 10^{-11}$ – $1.2 \times 10^{-11}$	Two build-up tests conducted over a 34.1-m interval
Silty mudstone at 238.4 m	Saulnier & Avis, 1988	$1.49 \times 10^{-20}$ – $1.49 \times 10^{-21}$	$1.0 \times 10^{-13}$ – $1.0 \times 10^{-14}$	Pulse testing in Waste Handling Shaft at discrete depth intervals
Silty claystone at 245.4 m	Saulnier & Avis, 1988	$7.47 \times 10^{-21}$ – $8.97 \times 10^{-22}$	$5.0 \times 10^{-14}$ – $6.0 \times 10^{-13}$	
Culebra Dolomite	Beauheim, 1987	$2.09 \times 10^{-14}$ – $1.18 \times 10^{-14}$	$1.0 \times 10^{-7}$ – $7.9 \times 10^{-8}$	Results of two drill-stem tests conducted in H-16
	Avis & Saulnier, 1990	$1.49 \times 10^{-14}$ – $2.84 \times 10^{-15}$	$1.0 \times 10^{-7}$ – $1.9 \times 10^{-8}$	Interpretation from fluid-pressure response in H-16 during drilling of AIS
Tamarisk Member	Avis & Saulnier, 1990	Response insufficient to estimate	Response insufficient to estimate	Interpretation from fluid-pressure response in H-16 during drilling of AIS
Magenta Member	Beauheim, 1987	$5.68 \times 10^{-16}$	$3.8 \times 10^{-9}$	Drill-stem test in H-16
	Avis & Saulnier, 1990	$1.49 \times 10^{-15}$	$1.0 \times 10^{-8}$	Interpretation from fluid-pressure response in H-16 during drilling of AIS
Forty-niner Member (Mudstone 4)	Beauheim, 1987	$2.84 \times 10^{-16}$ to $2.54 \times 10^{-16}$	$1.9 \times 10^{-9}$ – $1.7 \times 10^{-9}$	Testing at H-16
	Beauheim, 1987	$2.39 \times 10^{-15}$	$1.6 \times 10^{-18}$	Testing at H-14
	Avis & Saulnier, 1990	$3.89 \times 10^{-16}$	$2.6 \times 10^{-9}$	Interpretation from fluid-pressure response in H-16 during drilling of AIS



A value of  $1.49 \times 10^{-15} \text{ m}^2$  was selected as the undisturbed permeability for the Magenta. A value of  $1.49 \times 10^{-14} \text{ m}^2$  was selected for the disturbed permeability for the Magenta. This value is one order of magnitude greater than the undisturbed value.

The Forty-Niner member is composed of Anhydrite, Mudstone 4, and Anhydrite 6. At H-16, the permeability of the Forty-Niner Member is attached to Mudstone 4. Table C-3 summarizes hydraulic testing results for the Forty-Niner Member. Because the hydraulic conductivity value interpreted by Avis and Saulnier (1990) derived from a test that stressed a larger volume of rock, and because their hydraulic conductivity is larger than that determined for Mudstone 4 at H-16, a hydraulic conductivity of  $3.89 \times 10^{-16} \text{ m}^2$  was selected as the undisturbed permeability for Mudstone 4. The disturbed hydraulic conductivity for Mudstone 4 was assigned a value of  $3.89 \times 10^{-13} \text{ m}^2$ , which is three orders of magnitude greater than the undisturbed value. The undisturbed and disturbed permeability for the anhydrite units in the Forty-niner (Anhydrite 4 and Anhydrite 5) were assigned values of  $1.0 \times 10^{-19}$  and  $1.0 \times 10^{-15} \text{ m}^2$ , respectively.

### C3.4.2 Porosity

Hydraulic test analyses have been performed on the members of the Rustler Formation (Beauheim, 1987; Saulnier and Avis, 1988; and Avis and Saulnier, 1990). These investigators assumed porosity values consistent with clays and dolomites, which are considered to be the most permeable units within the Rustler. The porosity values for anhydrite and halite were derived primarily from underground testing at the WIPP. The primary references for the anhydrites and halite porosities are Beauheim et al. (1991), Sandia WIPP Project (1992), and Beauheim et al. (1993). The ranges in porosity values used by WIPP investigators are listed in Table C-14. Selected values for the formation porosities fell within the ranges listed in this table (Tables C-9 and C-10).

Table C-14. Summary of Literature Values for Formation Porosities

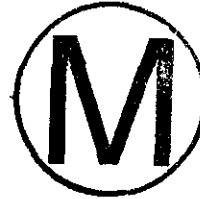
Information/Lithology	Reference(s)	Porosity Range
Salado Halite and Anhydrite	Peterson et al., 1987 Beauheim et al., 1991 WIPP PA, 1992-1993 Beauheim et al., 1993	0.001 to 0.01
Rustler clays and dolomites	Beauheim, 1987 Saulnier & Avis, 1988 Brinster, 1991 Freeze & Cherry, 1979	0.05 to 0.3

### C3.4.3 Formation Compressibility

The compressibility of the mudstone units and the transition/bioturbated clastic unit were calculated using Equation C-2 (Touloukian et al., 1981):



$$C_R = \frac{3(1-2\nu)}{E} \quad (C-2)$$



where:

$C_R$  = rock compressibility, Pa<sup>-1</sup>

$\nu$  = Poisson's ratio, dimensionless

$E$  = Young's modulus, Pa<sup>-1</sup>.

Touloukian et al. (1981) give a Young's modulus of 2.83 GPa and a Poisson's ratio of 0.04 for claystone. These values were assumed to be representative of the mudstones in the Rustler Formation. Substituting these values into Equation C-2 yields a rock compressibility of  $9.8 \times 10^{-10}$  Pa<sup>-1</sup>. Dividing this value by the mudstone porosity of 0.30 results in a pore-volume compressibility of  $3.3 \times 10^{-9}$  Pa<sup>-1</sup>.

The lithology of the transition/bioturbated clastic unit can be described as sandstone, siltstone, and halite-cemented sandstone and siltstone. Compressibility data for this unit are not available; therefore Young's modulus and Poisson's ratio for sandstones and siltstones were taken from Touloukian et al. (1981). The average Young's modulus and Poisson's ratio were 19.0 and 0.24 GPa respectively for sandstone, and 25.2 and 0.18 GPa respectively for siltstone. The values for the two rock types were then averaged to obtain a Young's modulus of 22.1 GPa and a Poisson's ratio of 0.21, assumed to be representative of the transition/bioturbated clastic unit. Using Equation C-2 and the assumed porosity of 0.20 yields a rock compressibility of  $7.9 \times 10^{-11}$  Pa<sup>-1</sup> and a pore-volume compressibility of  $3.9 \times 10^{-10}$  Pa<sup>-1</sup> for this unit.

LaVenue et al. (1990) assumed a rock compressibility of  $1.1 \times 10^{-9}$  Pa<sup>-1</sup> for the Culebra in their regional groundwater flow model. This value was adopted for the rock compressibility of the Culebra and Magenta. Dividing this value by the assumed porosity of 0.16 yields a pore-volume compressibility of  $6.9 \times 10^{-9}$  Pa<sup>-1</sup> for these two units.

The median rock compressibility for anhydrite interpreted from borehole testing was  $2.23 \times 10^{-11}$  Pa<sup>-1</sup> (DOE, 1996), which converts to a pore-volume compressibility of  $2.23 \times 10^{-9}$  Pa<sup>-1</sup> for a porosity of 0.01. Because no information about polyhalite compressibility was available, a value equal to that determined for anhydrite was assumed. A value of  $8.05 \times 10^{-9}$  Pa<sup>-1</sup> was used for pore-volume compressibility for the Salado halite. Rock and pore-volume compressibilities for all lithologic units modeled are summarized in Tables C-9 and C-10.

### C3.4.4 Two-Phase Properties of the Salado

Unsaturated flow properties for Salado halite and anhydrite marker beds were taken from Sandia WIPP Project (WIPP PA, 1992–1993) and are shown in Table C-15 in terms of parameter values for the Brooks-Corey equations for relative permeability and capillary pressure. The required parameters are threshold displacement pressure ( $P_t$ ), residual wetting phase saturation ( $S_{lr}$ ), residual gas saturation ( $S_{gr}$ ), and the pore size distribution parameter ( $\lambda$ ). Threshold displacement pressure ( $P_t$ ) is specified by using the correlation with permeability,  $k$ , suggested by Davies (1991) and documented in Sandia WIPP Project (WIPP PA, 1992–1993). The same parameters were used for both disturbed and undisturbed rock. For the compacted salt column

performance model, it was found that greater numerical stability could be achieved if the TOUGH28W implementations of the Van Genuchten-Parker equations were used for relative permeability and capillary pressure instead of the Brooks-Corey equations. Pressure parameter  $P_o$  in the Van Genuchten-Parker equation for capillary pressure was derived from the Brooks-Corey parameter  $P_c$  in Table C-15 by equating the two formulas at an effective saturation of 0.5.

Table C-15. Salado Two-Phase Properties

Parameter	Salado Halite and Polyhalite	Salado Anhydrite
$P_t$ (MPa)	$5.6 \times 10^{-7} [k(m^2)]^{-0.346}$	$2.6 \times 10^{-7} [k(m^2)]^{-0.346}$
$S_{lr}$	0.2	0.2
$S_{gr}$	0.0	0.0
$\lambda$	0.7	0.7

### C3.5 DRZ Properties

A disturbed rock zone (DRZ) forms around excavations in the bedded halite of the Salado Formation immediately upon passage of the mining tools, and progressively develops over time with the unloading of the formation as it creeps into excavations (Stormont, 1990). Van Sambeek et al. (1993) refer to the DRZ that forms upon mining as the "initial DRZ" and the DRZ that forms as a result of creep deformation and stress redistribution as the "secondary DRZ." The DRZ extends radially out from the shaft wall into the host formation. The DRZ is expected to have the following characteristics: (1) increased porosity resulting from micro- or macro-fracturing, (2) increased fluid (gas or liquid) permeability, (3) decreased brine saturation, (4) decreased load-bearing capacity, and (5) decreased lithostatic pressure (Stormont, 1990; Van Sambeek et al., 1993). Because of these properties, the DRZ could act as a vertical flow path for brine and gas around a shaft seal. It is important to characterize the extent of the DRZ around the shaft excavations and its time-dependent properties (especially permeability).

Laboratory, field, and modeling studies have been performed to determine the mechanics of DRZ development. DRZ development has been documented in almost all horizontal rectangular excavations of the WIPP underground facility through gas permeability testing (Stormont et al., 1987; Stormont, 1990), visual observations (Borns and Stormont, 1988), and by other methodologies (Holcomb, 1988). Laboratory testing of salt cores has also provided significant insight into DRZ development. Hansen and Mellegard (1979) found that dilatancy is favored by conditions of low confining stress and high deviatoric stress, which characterize the region near an excavation. Laboratory testing has shown that a halite DRZ is self-healing given the proper stress conditions; Brodsky (1990) showed that artificially damaged cores could be healed with certain confining pressures and time.

Two hydraulic testing programs have been conducted within WIPP shafts. The earliest hydraulic testing program was conducted in the Waste Handling Shaft (Saulnier and Avis, 1988). More recently, hydraulic testing was performed to determine the extent of the DRZ in the AIS.



Six boreholes, three at each of two levels, were used to determine both gas and brine permeabilities (Dale and Hurtado, 1996).



### Waste Handling Shaft Hydraulic Testing

The objective of the hydraulic testing conducted in the Waste Handling Shaft (Saulnier and Avis, 1988) was to identify the DRZ using permeability testing. This testing used a three-packer system capable of simultaneously testing the permeability in three zones at three different radial distances from the shaft. Four levels were tested, two in the unnamed lower member of the Rustler (depths 238.4 m [782 ft] and 245.4 m [805 ft] below ground surface [bgs]), which coincide with the transition and bioturbated clastic zones), one just below the Rustler/Salado contact in halite (at a depth of 259.1 m [850 ft] bgs), and one in Salado halite, anhydrite, and polyhalite (at a depth of 402.3 m [1320 ft] bgs). The results from these tests showed no correlation between permeability and radial distance from the shaft at any level and did not identify the DRZ. A potential reason the DRZ was not clearly identified in the Waste Handling Shaft was the location of the test intervals. For three of the test intervals, the test closest to the shaft was located 1 m (3.2 ft) from the excavation. One test conducted in the Waste Handling Shaft (W850W) tested a zone located within 0.3 m (1 ft) of the shaft liner. The test zone closest to the shaft for test W850W extended from the outer edge of the shaft liner to a distance of 1.25 m (4.08 ft) from the shaft. This zone included the liner/DRZ interface and the DRZ. Saulnier and Avis (1988) report that testing of this zone proved futile because the zone could not be pressurized. They concluded that the test zone included an open fracture or a gap representing the liner/DRZ interface.

### Air Intake Shaft Hydraulic Testing

Permeability testing was conducted to determine the radial extent of the DRZ in the Salado Formation surrounding the AIS. Testing was conducted at two levels within the AIS (Level A at 345.9 m [1135 ft] and Level C at 626.4 m [2,055 ft] bgs). At each of the two levels tested, three 10-cm (4-in.) diameter boreholes were drilled at a spacing of 120° into the formation at a 6° angle below the horizontal. The boreholes were drilled to a depth of approximately 6 m (20 ft). All six boreholes were gas-flow tested prior to the performance of brine testing. It is expected that the regions of the DRZ closest to the shaft wall have the greatest dilation and are likely the most desaturated (i.e., have brine saturations significantly less than 1.0). As the permeability of the DRZ approaches the intact permeability at greater radial distances, it is expected that the brine saturation of the DRZ approaches unity. Gas-flow tests were performed to determine the extent of the desaturated region (and, in so doing, define the radius where brine testing can be performed), to identify the relative permeability to gas of the DRZ, and to bracket the DRZ threshold pressure.

The distance within the boreholes at which the brine-permeability tests were conducted was based on the results of the gas-permeability testing. For gas-flow testing, a four-packer test tool was initially set so that the first test zone started at 6 in. from the shaft wall and extended an additional 15 in. into the formation. If gas flow was observed at that depth, the test tool was inserted an additional 2 to 4 in. and another test was performed. The process was repeated until a test with no observable gas flow was obtained. Brine-flow testing was performed approximately 5 to 6 in. beyond the distance at which no gas flow was observed. The objective of the brine-

permeability tests was to bracket the Salado permeability as a function of radial distance away from the shaft face in brine-saturated portions of the Salado. It was assumed that if the gas-permeability estimate was above  $1.0 \times 10^{-21} \text{ m}^2$ , the formation was not completely saturated with respect to brine. Once the gas permeability decreased to less than or equal to  $1.0 \times 10^{-21} \text{ m}^2$ , the formation was assumed to be at high brine saturations. The intact salt permeability was assumed (based on repository horizon testing) to be approximately  $1.0 \times 10^{-21} \text{ m}^2$ . This order of magnitude value for intact permeability was confirmed with the brine testing in the AIS. The gas permeability testing system threshold was  $1.0 \times 10^{-23} \text{ m}^2$ .

### C3.5.1 Model for Calculating the Effective DRZ Permeability

From the results of the field testing in the AIS it was determined that the permeability of the Salado halite can vary over orders of magnitude across the DRZ. An effective permeability of the DRZ can be estimated through the definition of a functional relationship for the change in permeability as a function of radial distance in the DRZ. The AIS field data provide insight into the variation of permeability in the DRZ and the extent of the DRZ. Figure C-1 plots the AIS brine and gas permeability results along with several lines demonstrating potential relationships of DRZ permeability as a function of radial distance and the extent of the DRZ.

This interpretation is taken from Dale and Hurtado (1996); the details are not provided here. The AIS field data support the assumption that the DRZ permeability is greatest in the DRZ near the excavation face and decreases radially outward away from the shaft wall. Figure C-1 shows that a log-linear model of permeability as a function of radial distance is reasonable, based on the field results. A log-linear variation in permeability is also consistent with radial variation in dilatant strain predicted in the DRZ. Figure C-2 is a schematic of a shaft with a DRZ of inner radius  $r_i$  and outer radius  $r_o$ . It is assumed that the permeability  $k_i$  at  $r_i$  is several orders of magnitude higher than the intact undisturbed permeability  $k_o$  defined at  $r_o$ . A log-linear model is assumed to describe the DRZ permeability as a function of radial distance, and used to calculate an effective DRZ permeability. Field data are limited, and a precise functional relation for the radial change in permeability is not known. However, this model captures results of available field data and incorporates the largest calculated extent of the DRZ.

An equation was derived to calculate the effective DRZ permeability assuming that the change in permeability within the DRZ is log-linear. For a given  $r_i$ ,  $k_i$ ,  $r_o$ , and  $k_o$ , an effective DRZ permeability can be calculated that accounts for both the decrease in DRZ permeability and the increase in flow area as a function of radial distance away from the excavation. The equation for the effective DRZ permeability is:

$$k_{\text{DRZ}} = \frac{2}{r_o + r_i} \left[ \left( \frac{r_o [\ln(k_o) - \ln(k_i)] - \Delta r}{[\ln(k_o) - \ln(k_i)]^2} \right) k_o - \left( \frac{r_i [\ln(k_o) - \ln(k_i)] - \Delta r}{[\ln(k_o) - \ln(k_i)]^2} \right) k_i \right] \quad (\text{C-3})$$

where  $\Delta r$  is equal to the outer DRZ radius minus the inner DRZ radius.

Figure C-1 demonstrates that this relationship (dotted lines) provides a reasonable representation of the field permeability test results for both the upper and lower zones of the AIS.

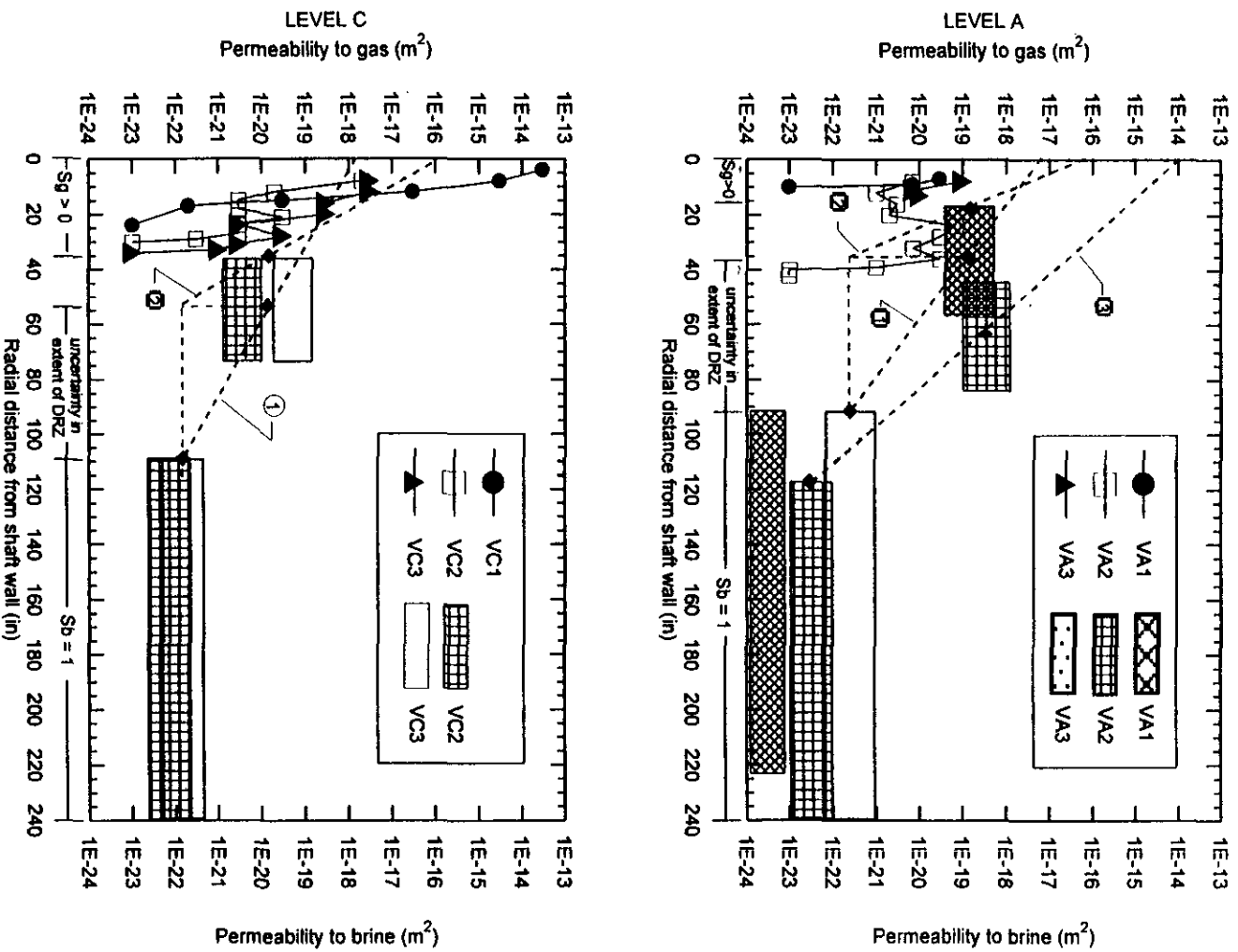
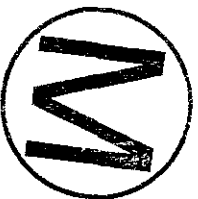
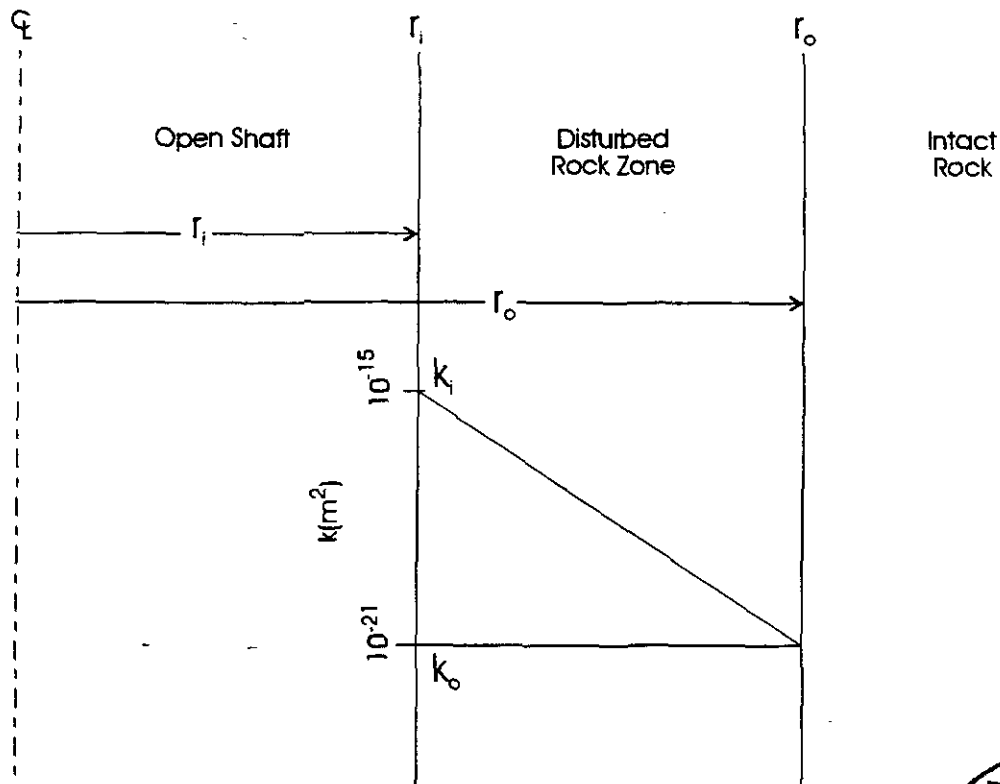


Figure C-1. AIS field permeability results.





- $k_i$  Represents Maximum Dilation
- $k_o$  Represents Intact Conditions
- $r_i$  Excavation Face, Inner Radius of DRZ
- $r_o$  Outer Radius of DRZ

Figure C-2. Log-linear model for the calculation of an effective permeability of the DRZ.

### C3.5.2 Model DRZ Effective Permeability

Rock mechanics calculations have been performed to predict the DRZ extent in both the Rustler and Salado formations. These calculations are presented in Appendix D of this report. The extent of the DRZ within the Rustler Formation is a function of rock type and depth. Mechanical calculations presented in Appendix D indicate no DRZ for anhydrites and dolomites, and a DRZ extent that increases with shaft depth for mudstones. The DRZ extent for the Rustler mudstones was interpolated from values given in Appendix D. For the base case assumption, the anhydrites were assumed to have no DRZ, consistent with the mechanical calculations presented in Appendix D. However, for the base-case model conceptualization, the Magenta and Culebra dolomites were assigned a DRZ. This was done to account for the fact that both of these dolomites are naturally fractured and the mechanical calculations did not account for the

presence of fractures. The extent of the DRZ for dolomite was set equal to one shaft radius. The DRZ in the Rustler is assumed not to heal as a function of time.

The DRZ extent within the Salado halite is calculated as a function of depth, shaft seal material, and time. In the Salado, the halite DRZ is at a maximum at closure and heals as a function of time. Healing occurs quickest with increased depth of burial and increased stiffness (bulk modulus) of the shaft seal material. Calculations of the radial extent of the halite DRZ for times 0, 10, 25, 50, and 100 years after shaft closure are provided in Appendix D. Plots of the halite DRZ extent adjacent to the various seal materials are also shown in Appendix D.

For halite, the effective DRZ permeability was calculated with Equation C-3 using the extent of the halite DRZ from Appendix D and the disturbed halite permeability at the shaft/DRZ interface. The effective permeability of the DRZ, as calculated using Equation C-3, is controlled by the permeability at the shaft/DRZ interface ( $k_i$ ). For these calculations,  $k_i$  is assumed to remain constant and at its maximum value as long as a DRZ is predicted. In reality, it is expected that as the DRZ heals (halite),  $k_i$  will also decrease in magnitude. Therefore the calculation of the effective DRZ permeability is considered conservative.

Also presented in Appendix D are mechanical calculations that predict the DRZ in anhydrite Salado interbeds as a function of interbed thickness. These calculations show that for an anhydrite interbed thickness less than approximately 0.8 m, the anhydrite interbeds develop a DRZ approximately 1 m in extent. Previous estimates predicted that Salado anhydrite units with a thickness of less than 3 m have a DRZ extending 1 m from the shaft. For the base-case conceptualization, anhydrite units equal to or greater than 3 m in thickness were assigned no DRZ.

Because the anhydrite and polyhalite DRZs do not heal, the values calculated for DRZ extent do not change with time for these units. The DRZ extent for polyhalite for all times was assumed to be equal to the halite DRZ extent for the open shaft time period. Effective DRZ permeabilities based on Equation C-3 were adjusted for the difference between model DRZ areas, which do not vary (12% of shaft radius), and the variable DRZ areas described above.

Mechanical calculations predict that anhydrites within the Rustler and several within the Salado do not form a DRZ. These predictions do not account for damage induced during shaft construction, such as blasting damage. Because field data are not available for the DRZ in the Rustler members and Salado anhydrites, the models assume that the DRZ may be configured as "continuous" or "discontinuous." The discontinuous DRZ assumption utilizes only intact permeability values for Salado anhydrites and Rustler members. The continuous DRZ assumes these lithologies are damaged, and permeabilities are adjusted accordingly.

The model grids in this appendix do not include a discrete interface zone between shaft seal materials and the DRZ. This is because the model grids presented were based on the assumption that a continuous DRZ would be considered in all simulations. In the base-case conceptualization, a discontinuous DRZ is modeled consistent with mechanical predictions. However, in all cases the models are also run considering a continuous DRZ.

Mechanical calculations presented in Appendix D indicate that the DRZ surrounding the concrete-asphalt waterstops becomes discontinuous through healing of the salt within 2 years after emplacement. In the modeling in this appendix, it is assumed that the waterstops



effectively intersect the DRZ at 2 years after seal emplacement. Table C-16 gives the permeability values used for the base case conceptualization of the DRZ.

At the Rustler/Salado contact, unsaturated Rustler brine can potentially enter the Salado DRZ. Seepage of Rustler groundwater into the Salado DRZ could result in dissolution of Salado salt. It has been postulated that this type of dissolution would produce a direct conduit from the Rustler/Salado contact to the lower Salado sealing system. Approximately  $1.4 \times 10^{-4} \text{ m}^3$  (0.3 kg) of salt are required to fully saturate  $10^{-3} \text{ m}^3$  (1 kg) of Culebra groundwater (Siegel et al., 1991). The potential for creation of such a conduit will be treated within Performance Model 1.

## **C4. FLOW DOWN FROM THE RUSTLER (MODEL 1)**

### **C4.1 Statement of Problem**

The shaft seal system is designed to limit migration of fluids within the sealed shaft. Using the approximation of a completely saturated seal system, this calculation examined the potential for flow and quantity of flow that migrates from the Rustler and Salado down the shaft during early times. The performance measures (results) from this model are brine flow rate and cumulative brine volume over a 200-year time frame after repository closure. These performance measures are presented at (1) the Rustler/Salado interface, (2) the top of the compacted salt column, and (3) the base of the compacted salt column.

### **C4.2 Performance Model 1 Description**

#### **C4.2.1 Conceptual Model and Assumptions**

To investigate the potential for vertical flow down from the Rustler through the shaft seal system, a full-shaft saturated-flow model was used. The focus of this calculation was to estimate the amount of brine flowing down through the shaft seal system to reach the top of the compacted salt column and, potentially, the repository.

Conceptually, flow down the seal system is an early-time issue. Over time, pressures at depth in the seal system will equilibrate to far-field pressures, which are significantly over-pressured with respect to the Rustler, and the downward driving force will reverse its direction. However, because the Rustler will repressurize more rapidly than the Salado, there is a potential for downward flow during the seal repressurization period. To characterize this period, the flow system has been conceptualized as a shaft seal system and an adjacent DRZ surrounded by host rocks. The primary assumptions are listed below:

- This calculation assumed that the primary water-producing zones above the Salado Formation are within the Rustler Formation. As a result, this calculation did not include supra-Rustler units.
- The calculation assumed brine-saturated flow conditions. This assumption (1) did not account for the time required or volume of liquid required to saturate the seal components and (2) overestimated brine transmissivities over the time period where the DRZ and seals would be variably saturated.



Table C-16. Model DRZ Permeability for Base-Case Conceptualization (Corrected for Model DRZ Area)

Row	Unit	Intrinsic Permeability (m <sup>2</sup> )					
		Time=0 Yr	Time=2 Yr	Time=10 Yr	Time=25 Yr	Time=50 Yr	Time=100 Yr
1	Anhydrite5	1.00×10 <sup>-19</sup>	1.00×10 <sup>-19</sup>	1.00×10 <sup>-19</sup>	1.00×10 <sup>-19</sup>	1.00×10 <sup>-19</sup>	1.00×10 <sup>-19</sup>
2	Anhydrite5	1.00×10 <sup>-19</sup>	1.00×10 <sup>-19</sup>	1.00×10 <sup>-19</sup>	1.00×10 <sup>-19</sup>	1.00×10 <sup>-19</sup>	1.00×10 <sup>-19</sup>
3	Mudstone4	5.99×10 <sup>-13</sup>	5.99×10 <sup>-13</sup>	5.99×10 <sup>-13</sup>	5.99×10 <sup>-13</sup>	5.99×10 <sup>-13</sup>	5.99×10 <sup>-13</sup>
4	Mudstone4	5.99×10 <sup>-13</sup>	5.99×10 <sup>-13</sup>	5.99×10 <sup>-13</sup>	5.99×10 <sup>-13</sup>	5.99×10 <sup>-13</sup>	5.99×10 <sup>-13</sup>
5	Anhydrite4	1.00×10 <sup>-19</sup>	1.00×10 <sup>-19</sup>	1.00×10 <sup>-19</sup>	1.00×10 <sup>-19</sup>	1.00×10 <sup>-19</sup>	1.00×10 <sup>-19</sup>
6	Magenta	6.06×10 <sup>-14</sup>	6.06×10 <sup>-14</sup>	6.06×10 <sup>-14</sup>	6.06×10 <sup>-14</sup>	6.06×10 <sup>-14</sup>	6.06×10 <sup>-14</sup>
7	Anhydrite3	1.00×10 <sup>-19</sup>	1.00×10 <sup>-19</sup>	1.00×10 <sup>-19</sup>	1.00×10 <sup>-19</sup>	1.00×10 <sup>-19</sup>	1.00×10 <sup>-19</sup>
8	Anhydrite3	1.00×10 <sup>-19</sup>	1.00×10 <sup>-19</sup>	1.00×10 <sup>-19</sup>	1.00×10 <sup>-19</sup>	1.00×10 <sup>-19</sup>	1.00×10 <sup>-19</sup>
9	Mudstone3	2.75×10 <sup>-16</sup>	2.75×10 <sup>-16</sup>	2.75×10 <sup>-16</sup>	2.75×10 <sup>-16</sup>	2.75×10 <sup>-16</sup>	2.75×10 <sup>-16</sup>
10	Anhydrite2	1.00×10 <sup>-19</sup>	1.00×10 <sup>-19</sup>	1.00×10 <sup>-19</sup>	1.00×10 <sup>-19</sup>	1.00×10 <sup>-19</sup>	1.00×10 <sup>-19</sup>
11	Anhydrite2	1.00×10 <sup>-19</sup>	1.00×10 <sup>-19</sup>	1.00×10 <sup>-19</sup>	1.00×10 <sup>-19</sup>	1.00×10 <sup>-19</sup>	1.00×10 <sup>-19</sup>
12	Culbera/Mudstone2	8.50×10 <sup>-13</sup>	8.50×10 <sup>-13</sup>	8.50×10 <sup>-13</sup>	8.50×10 <sup>-13</sup>	8.50×10 <sup>-13</sup>	8.50×10 <sup>-13</sup>
13	Anhydrite1/Mudstone1	1.00×10 <sup>-19</sup>	1.00×10 <sup>-19</sup>	1.00×10 <sup>-19</sup>	1.00×10 <sup>-19</sup>	1.00×10 <sup>-19</sup>	1.00×10 <sup>-19</sup>
14	Transition/Bioturbated Clastics	4.94×10 <sup>-15</sup>	4.94×10 <sup>-15</sup>	4.94×10 <sup>-15</sup>	4.94×10 <sup>-15</sup>	4.94×10 <sup>-15</sup>	4.94×10 <sup>-15</sup>
15	Transition/Bioturbated Clastics	4.94×10 <sup>-15</sup>	4.94×10 <sup>-15</sup>	4.94×10 <sup>-15</sup>	4.94×10 <sup>-15</sup>	4.94×10 <sup>-15</sup>	4.94×10 <sup>-15</sup>
16	Transition/Bioturbated Clastics	4.94×10 <sup>-15</sup>	4.94×10 <sup>-15</sup>	4.94×10 <sup>-15</sup>	4.94×10 <sup>-15</sup>	4.94×10 <sup>-15</sup>	4.94×10 <sup>-15</sup>
17	Transition/Bioturbated Clastics	4.94×10 <sup>-15</sup>	4.94×10 <sup>-15</sup>	4.94×10 <sup>-15</sup>	4.94×10 <sup>-15</sup>	4.94×10 <sup>-15</sup>	4.94×10 <sup>-15</sup>
18	Transition/Bioturbated Clastics	4.94×10 <sup>-15</sup>	4.94×10 <sup>-15</sup>	4.94×10 <sup>-15</sup>	4.94×10 <sup>-15</sup>	4.94×10 <sup>-15</sup>	4.94×10 <sup>-15</sup>
19	Transition/Bioturbated Clastics	4.94×10 <sup>-15</sup>	4.94×10 <sup>-15</sup>	4.94×10 <sup>-15</sup>	4.94×10 <sup>-15</sup>	4.94×10 <sup>-15</sup>	4.94×10 <sup>-15</sup>
20	Salado Halite	3.64×10 <sup>-16</sup>	3.64×10 <sup>-16</sup>	3.62×10 <sup>-16</sup>	3.59×10 <sup>-16</sup>	3.55×10 <sup>-16</sup>	3.49×10 <sup>-16</sup>
21	Salado Halite	3.68×10 <sup>-16</sup>	3.68×10 <sup>-16</sup>	1.10×10 <sup>-16</sup>	4.05×10 <sup>-17</sup>	1.00×10 <sup>-21</sup>	1.00×10 <sup>-21</sup>

C-32



Table C-16. Model DRZ Permeability for Base-Case Conceptualization (Corrected for Model DRZ Area)

Row	Unit	Intrinsic Permeability (m <sup>2</sup> )					
		Time=0 Yr	Time=2 Yr	Time=10 Yr	Time=25 Yr	Time=50 Yr	Time=100 Yr
22	Salado Halite	3.70×10 <sup>-16</sup>	3.70×10 <sup>-16</sup>	1.08×10 <sup>-16</sup>	3.88×10 <sup>-17</sup>	1.00×10 <sup>-21</sup>	1.00×10 <sup>-21</sup>
23	Salado Halite	3.72×10 <sup>-16</sup>	3.72×10 <sup>-16</sup>	1.07×10 <sup>-16</sup>	3.80×10 <sup>-17</sup>	1.00×10 <sup>-21</sup>	1.00×10 <sup>-21</sup>
24	Salado Halite	3.73×10 <sup>-16</sup>	3.73×10 <sup>-16</sup>	1.06×10 <sup>-16</sup>	3.72×10 <sup>-17</sup>	1.00×10 <sup>-21</sup>	1.00×10 <sup>-21</sup>
25	Salado Halite	3.74×10 <sup>-16</sup>	3.74×10 <sup>-16</sup>	3.72×10 <sup>-16</sup>	3.69×10 <sup>-16</sup>	3.65×10 <sup>-16</sup>	3.58×10 <sup>-16</sup>
26	Salado Halite	3.76×10 <sup>-16</sup>	3.76×10 <sup>-16</sup>	3.73×10 <sup>-16</sup>	3.70×10 <sup>-16</sup>	3.66×10 <sup>-16</sup>	3.60×10 <sup>-16</sup>
27	Salado Halite	3.78×10 <sup>-16</sup>	3.78×10 <sup>-16</sup>	3.76×10 <sup>-16</sup>	3.73×10 <sup>-16</sup>	3.69×10 <sup>-16</sup>	3.62×10 <sup>-16</sup>
28	Salado Halite	3.83×10 <sup>-16</sup>	3.83×10 <sup>-16</sup>	3.81×10 <sup>-16</sup>	3.78×10 <sup>-16</sup>	3.73×10 <sup>-16</sup>	3.66×10 <sup>-16</sup>
29	Salado Halite	3.86×10 <sup>-16</sup>	3.86×10 <sup>-16</sup>	9.75×10 <sup>-17</sup>	2.87×10 <sup>-17</sup>	1.00×10 <sup>-21</sup>	1.00×10 <sup>-21</sup>
30	Salado Halite	3.88×10 <sup>-16</sup>	3.88×10 <sup>-16</sup>	9.62×10 <sup>-17</sup>	2.74×10 <sup>-17</sup>	1.00×10 <sup>-21</sup>	1.00×10 <sup>-21</sup>
31	Salado Halite	3.90×10 <sup>-16</sup>	1.00×10 <sup>-20</sup>				
32	Salado Halite	3.91×10 <sup>-16</sup>	3.91×10 <sup>-16</sup>	9.47×10 <sup>-17</sup>	2.60×10 <sup>-17</sup>	1.00×10 <sup>-21</sup>	1.00×10 <sup>-21</sup>
33	Salado Halite	3.93×10 <sup>-16</sup>	3.93×10 <sup>-16</sup>	9.33×10 <sup>-17</sup>	2.47×10 <sup>-17</sup>	1.00×10 <sup>-21</sup>	1.00×10 <sup>-21</sup>
34	Combined Unit 1	1.15×10 <sup>-18</sup>	1.15×10 <sup>-18</sup>	1.15×10 <sup>-18</sup>	1.15×10 <sup>-18</sup>	1.15×10 <sup>-18</sup>	1.15×10 <sup>-18</sup>
35	Combined Unit 1	1.15×10 <sup>-18</sup>	1.15×10 <sup>-18</sup>	1.15×10 <sup>-18</sup>	1.15×10 <sup>-18</sup>	1.15×10 <sup>-18</sup>	1.15×10 <sup>-18</sup>
36	Salado Halite	4.00×10 <sup>-16</sup>	4.00×10 <sup>-16</sup>	2.92×10 <sup>-16</sup>	1.97×10 <sup>-16</sup>	1.01×10 <sup>-16</sup>	2.56×10 <sup>-17</sup>
37	Salado Halite	4.05×10 <sup>-16</sup>	4.05×10 <sup>-16</sup>	2.90×10 <sup>-16</sup>	1.91×10 <sup>-16</sup>	9.13×10 <sup>-17</sup>	1.81×10 <sup>-17</sup>
38	Salado Halite	4.13×10 <sup>-16</sup>	4.13×10 <sup>-16</sup>	2.86×10 <sup>-16</sup>	1.81×10 <sup>-16</sup>	7.85×10 <sup>-17</sup>	7.76×10 <sup>-18</sup>
39	Combined Unit 2	1.04×10 <sup>-18</sup>	1.04×10 <sup>-18</sup>	1.04×10 <sup>-18</sup>	1.04×10 <sup>-18</sup>	1.04×10 <sup>-18</sup>	1.04×10 <sup>-18</sup>
40	Salado Halite	4.25×10 <sup>-16</sup>	4.25×10 <sup>-16</sup>	2.75×10 <sup>-16</sup>	1.63×10 <sup>-16</sup>	6.00×10 <sup>-17</sup>	1.00×10 <sup>-21</sup>
41	Salado Halite	4.32×10 <sup>-16</sup>	4.32×10 <sup>-16</sup>	2.66×10 <sup>-16</sup>	1.51×10 <sup>-16</sup>	5.04×10 <sup>-17</sup>	1.00×10 <sup>-21</sup>
42	Salado Halite	4.37×10 <sup>-16</sup>	4.37×10 <sup>-16</sup>	2.61×10 <sup>-16</sup>	1.42×10 <sup>-16</sup>	4.37×10 <sup>-17</sup>	1.00×10 <sup>-21</sup>
43	Combined Unit 3	4.79×10 <sup>-16</sup>	4.79×10 <sup>-16</sup>	4.79×10 <sup>-16</sup>	4.79×10 <sup>-16</sup>	4.79×10 <sup>-16</sup>	4.79×10 <sup>-16</sup>
44	Salado Halite	4.41×10 <sup>-16</sup>	4.41×10 <sup>-16</sup>	2.55×10 <sup>-16</sup>	1.34×10 <sup>-16</sup>	3.73×10 <sup>-17</sup>	1.00×10 <sup>-21</sup>
45	Salado Halite	4.44×10 <sup>-16</sup>	4.44×10 <sup>-16</sup>	2.52×10 <sup>-16</sup>	1.29×10 <sup>-16</sup>	3.35×10 <sup>-17</sup>	1.00×10 <sup>-21</sup>
46	Salado Halite	4.47×10 <sup>-16</sup>	4.47×10 <sup>-16</sup>	2.49×10 <sup>-16</sup>	1.25×10 <sup>-16</sup>	3.00×10 <sup>-17</sup>	1.00×10 <sup>-21</sup>
47	Vaca Triste	1.40×10 <sup>-16</sup>	1.40×10 <sup>-16</sup>	1.40×10 <sup>-16</sup>	1.40×10 <sup>-16</sup>	1.40×10 <sup>-16</sup>	1.40×10 <sup>-16</sup>

C-33

M

Table C-16. Model DRZ Permeability for Base-Case Conceptualization (Corrected for Model DRZ Area)

Row	Unit	Intrinsic Permeability (m <sup>2</sup> )					
		Time=0 Yr	Time=2 Yr	Time=10 Yr	Time=25 Yr	Time=50 Yr	Time=100 Yr
48	Salado Halite	4.49×10 <sup>-16</sup>	4.49×10 <sup>-16</sup>	2.45×10 <sup>-16</sup>	1.20×10 <sup>-16</sup>	2.64×10 <sup>-17</sup>	1.00×10 <sup>-21</sup>
49	Salado Halite	4.50×10 <sup>-16</sup>	4.50×10 <sup>-16</sup>	2.45×10 <sup>-16</sup>	1.19×10 <sup>-16</sup>	2.55×10 <sup>-17</sup>	1.00×10 <sup>-21</sup>
50	Salado Halite	4.52×10 <sup>-16</sup>	4.52×10 <sup>-16</sup>	5.44×10 <sup>-17</sup>	2.94×10 <sup>-18</sup>	1.00×10 <sup>-21</sup>	1.00×10 <sup>-21</sup>
51	Salado Halite	4.53×10 <sup>-16</sup>	4.53×10 <sup>-16</sup>	5.32×10 <sup>-17</sup>	2.64×10 <sup>-18</sup>	1.00×10 <sup>-21</sup>	1.00×10 <sup>-21</sup>
52	Salado Halite	4.54×10 <sup>-16</sup>	1.00×10 <sup>-20</sup>				
53	Salado Halite	4.55×10 <sup>-16</sup>	4.55×10 <sup>-16</sup>	5.19×10 <sup>-17</sup>	2.30×10 <sup>-18</sup>	1.00×10 <sup>-21</sup>	1.00×10 <sup>-21</sup>
54	Salado Halite	4.57×10 <sup>-16</sup>	4.57×10 <sup>-16</sup>	5.07×10 <sup>-17</sup>	2.00×10 <sup>-18</sup>	1.00×10 <sup>-21</sup>	1.00×10 <sup>-21</sup>
55	Salado Halite	4.60×10 <sup>-16</sup>	4.60×10 <sup>-16</sup>	9.88×10 <sup>-17</sup>	7.89×10 <sup>-18</sup>	1.00×10 <sup>-21</sup>	1.00×10 <sup>-21</sup>
56	Salado Halite	4.65×10 <sup>-16</sup>	4.65×10 <sup>-16</sup>	9.40×10 <sup>-17</sup>	3.94×10 <sup>-18</sup>	1.00×10 <sup>-21</sup>	1.00×10 <sup>-21</sup>
57	Combined Unit 4	5.46×10 <sup>-16</sup>	5.46×10 <sup>-16</sup>	1.73×10 <sup>-16</sup>	9.66×10 <sup>-19</sup>	1.90×10 <sup>-20</sup>	1.90×10 <sup>-20</sup>
58	Salado Halite	4.71×10 <sup>-16</sup>	4.71×10 <sup>-16</sup>	8.65×10 <sup>-17</sup>	1.00×10 <sup>-21</sup>	1.00×10 <sup>-21</sup>	1.00×10 <sup>-21</sup>
59	Salado Halite	4.73×10 <sup>-16</sup>	4.73×10 <sup>-16</sup>	8.36×10 <sup>-17</sup>	1.00×10 <sup>-21</sup>	1.00×10 <sup>-21</sup>	1.00×10 <sup>-21</sup>
60	Union Anhydrite	3.86×10 <sup>-16</sup>	3.86×10 <sup>-16</sup>	3.86×10 <sup>-16</sup>	3.86×10 <sup>-16</sup>	3.86×10 <sup>-16</sup>	3.86×10 <sup>-16</sup>
61	Salado Halite	4.76×10 <sup>-16</sup>	4.76×10 <sup>-16</sup>	8.08×10 <sup>-17</sup>	1.00×10 <sup>-21</sup>	1.00×10 <sup>-21</sup>	1.00×10 <sup>-21</sup>
62	Salado Halite	4.78×10 <sup>-16</sup>	4.78×10 <sup>-16</sup>	7.80×10 <sup>-17</sup>	1.00×10 <sup>-21</sup>	1.00×10 <sup>-21</sup>	1.00×10 <sup>-21</sup>
63	Salado Halite	4.81×10 <sup>-16</sup>	4.81×10 <sup>-16</sup>	7.42×10 <sup>-17</sup>	1.00×10 <sup>-21</sup>	1.00×10 <sup>-21</sup>	1.00×10 <sup>-21</sup>
64	Combined Unit 5	3.37×10 <sup>-16</sup>	3.37×10 <sup>-16</sup>	3.37×10 <sup>-16</sup>	3.37×10 <sup>-16</sup>	3.37×10 <sup>-16</sup>	3.37×10 <sup>-16</sup>
65	Salado Halite	4.85×10 <sup>-16</sup>	4.85×10 <sup>-16</sup>	6.91×10 <sup>-17</sup>	1.00×10 <sup>-21</sup>	1.00×10 <sup>-21</sup>	1.00×10 <sup>-21</sup>
66	Salado Halite	4.88×10 <sup>-16</sup>	4.88×10 <sup>-16</sup>	6.62×10 <sup>-17</sup>	1.00×10 <sup>-21</sup>	1.00×10 <sup>-21</sup>	1.00×10 <sup>-21</sup>
67	Salado Halite	4.90×10 <sup>-16</sup>	4.90×10 <sup>-16</sup>	6.34×10 <sup>-17</sup>	1.00×10 <sup>-21</sup>	1.00×10 <sup>-21</sup>	1.00×10 <sup>-21</sup>
68	Combined Unit 6	5.91×10 <sup>-16</sup>	5.91×10 <sup>-16</sup>	7.93×10 <sup>-17</sup>	1.08×10 <sup>-20</sup>	1.08×10 <sup>-20</sup>	1.08×10 <sup>-20</sup>
69	Salado Halite	4.93×10 <sup>-16</sup>	4.93×10 <sup>-16</sup>	5.96×10 <sup>-17</sup>	1.00×10 <sup>-21</sup>	1.00×10 <sup>-21</sup>	1.00×10 <sup>-21</sup>
70	Salado Halite	4.95×10 <sup>-16</sup>	4.95×10 <sup>-16</sup>	5.67×10 <sup>-17</sup>	1.00×10 <sup>-21</sup>	1.00×10 <sup>-21</sup>	1.00×10 <sup>-21</sup>
71	Combined Unit 7	5.94×10 <sup>-16</sup>	5.94×10 <sup>-16</sup>	8.12×10 <sup>-17</sup>	1.33×10 <sup>-20</sup>	1.33×10 <sup>-20</sup>	1.33×10 <sup>-20</sup>
72	Salado Halite	5.03×10 <sup>-16</sup>	5.03×10 <sup>-16</sup>	4.77×10 <sup>-17</sup>	1.00×10 <sup>-21</sup>	1.00×10 <sup>-21</sup>	1.00×10 <sup>-21</sup>
73	Salado Halite	5.05×10 <sup>-16</sup>	5.05×10 <sup>-16</sup>	4.38×10 <sup>-17</sup>	1.00×10 <sup>-21</sup>	1.00×10 <sup>-21</sup>	1.00×10 <sup>-21</sup>

M

C-34



Table C-16. Model DRZ Permeability for Base-Case Conceptualization (Corrected for Model DRZ Area)

Row	Unit	Intrinsic Permeability (m <sup>2</sup> )					
		Time=0 Yr	Time=2 Yr	Time=10 Yr	Time=25 Yr	Time=50 Yr	Time=100 Yr
74	Salado Halite	$5.06 \times 10^{-16}$	$5.06 \times 10^{-16}$	$4.15 \times 10^{-17}$	$1.00 \times 10^{-21}$	$1.00 \times 10^{-21}$	$1.00 \times 10^{-21}$
75	Combined Unit 8	$5.85 \times 10^{-16}$	$5.85 \times 10^{-16}$	$8.42 \times 10^{-17}$	$1.88 \times 10^{-20}$	$1.88 \times 10^{-20}$	$1.88 \times 10^{-20}$
76	Salado Halite	$5.08 \times 10^{-16}$	$5.08 \times 10^{-16}$	$3.89 \times 10^{-17}$	$1.00 \times 10^{-21}$	$1.00 \times 10^{-21}$	$1.00 \times 10^{-21}$
77	Salado Halite	$5.09 \times 10^{-16}$	$5.09 \times 10^{-16}$	$3.61 \times 10^{-17}$	$1.00 \times 10^{-21}$	$1.00 \times 10^{-21}$	$1.00 \times 10^{-21}$
78	Salado Halite	$5.11 \times 10^{-16}$	$5.11 \times 10^{-16}$	$3.31 \times 10^{-17}$	$1.00 \times 10^{-21}$	$1.00 \times 10^{-21}$	$1.00 \times 10^{-21}$
79	Combined Unit 9	$1.29 \times 10^{-19}$	$1.29 \times 10^{-19}$	$1.29 \times 10^{-19}$	$1.29 \times 10^{-19}$	$1.29 \times 10^{-19}$	$1.29 \times 10^{-19}$
80	Combined Unit 9	$1.29 \times 10^{-19}$	$1.29 \times 10^{-19}$	$1.29 \times 10^{-19}$	$1.29 \times 10^{-19}$	$1.29 \times 10^{-19}$	$1.29 \times 10^{-19}$
81	Salado Halite	$5.13 \times 10^{-16}$	$5.13 \times 10^{-16}$	$2.99 \times 10^{-17}$	$1.00 \times 10^{-21}$	$1.00 \times 10^{-21}$	$1.00 \times 10^{-21}$
82	Salado Halite	$5.13 \times 10^{-16}$	$5.13 \times 10^{-16}$	$5.53 \times 10^{-18}$	$1.00 \times 10^{-21}$	$1.00 \times 10^{-21}$	$1.00 \times 10^{-21}$
83	Salado Halite	$5.13 \times 10^{-16}$	$5.13 \times 10^{-16}$	$5.25 \times 10^{-18}$	$1.00 \times 10^{-21}$	$1.00 \times 10^{-21}$	$1.00 \times 10^{-21}$
84	Salado Halite	$5.14 \times 10^{-16}$	$5.14 \times 10^{-16}$	$4.95 \times 10^{-18}$	$1.00 \times 10^{-21}$	$1.00 \times 10^{-21}$	$1.00 \times 10^{-21}$
85	Salado Halite	$5.14 \times 10^{-16}$	$1.00 \times 10^{-20}$				
86	Salado Halite	$5.15 \times 10^{-16}$	$5.15 \times 10^{-16}$	$4.48 \times 10^{-18}$	$1.00 \times 10^{-21}$	$1.00 \times 10^{-21}$	$1.00 \times 10^{-21}$
87	Salado Halite	$5.16 \times 10^{-16}$	$5.16 \times 10^{-16}$	$4.08 \times 10^{-18}$	$1.00 \times 10^{-21}$	$1.00 \times 10^{-21}$	$1.00 \times 10^{-21}$
88	Salado Halite	$5.16 \times 10^{-16}$	$5.16 \times 10^{-16}$	$1.02 \times 10^{-16}$	$1.91 \times 10^{-18}$	$1.00 \times 10^{-21}$	$1.00 \times 10^{-21}$
89	Combined Unit 10	$1.09 \times 10^{-19}$	$1.09 \times 10^{-19}$	$1.09 \times 10^{-19}$	$1.09 \times 10^{-19}$	$1.09 \times 10^{-19}$	$1.09 \times 10^{-19}$
90	Combined Unit 10	$1.09 \times 10^{-19}$	$1.09 \times 10^{-19}$	$1.09 \times 10^{-19}$	$1.09 \times 10^{-19}$	$1.09 \times 10^{-19}$	$1.09 \times 10^{-19}$
91	Salado Halite	$5.18 \times 10^{-16}$	$5.18 \times 10^{-16}$	$9.66 \times 10^{-17}$	$1.43 \times 10^{-18}$	$1.00 \times 10^{-21}$	$1.00 \times 10^{-21}$
92	Salado Halite	$5.19 \times 10^{-16}$	$5.19 \times 10^{-16}$	$9.18 \times 10^{-17}$	$1.01 \times 10^{-18}$	$1.00 \times 10^{-21}$	$1.00 \times 10^{-21}$
93	Salado Halite	$5.21 \times 10^{-16}$	$5.21 \times 10^{-16}$	$8.76 \times 10^{-17}$	$6.34 \times 10^{-19}$	$1.00 \times 10^{-21}$	$1.00 \times 10^{-21}$
94	Salado Halite	$5.21 \times 10^{-16}$	$5.21 \times 10^{-16}$	$8.55 \times 10^{-17}$	$4.47 \times 10^{-19}$	$1.00 \times 10^{-21}$	$1.00 \times 10^{-21}$
95	Salado Halite	$5.22 \times 10^{-16}$	$5.22 \times 10^{-16}$	$8.44 \times 10^{-17}$	$3.53 \times 10^{-19}$	$1.00 \times 10^{-21}$	$1.00 \times 10^{-21}$
96	Combined Unit 11	$2.86 \times 10^{-16}$	$2.86 \times 10^{-16}$	$2.86 \times 10^{-16}$	$2.86 \times 10^{-16}$	$2.86 \times 10^{-16}$	$2.86 \times 10^{-16}$
97	Salado Halite	$5.22 \times 10^{-16}$	$5.22 \times 10^{-16}$	$5.22 \times 10^{-16}$	$5.22 \times 10^{-16}$	$5.22 \times 10^{-16}$	$5.22 \times 10^{-16}$
98	Salado Halite	$5.22 \times 10^{-16}$	$5.22 \times 10^{-16}$	$5.22 \times 10^{-16}$	$5.22 \times 10^{-16}$	$5.22 \times 10^{-16}$	$5.22 \times 10^{-16}$
99	Salado Halite	$5.23 \times 10^{-16}$	$5.23 \times 10^{-16}$	$5.23 \times 10^{-16}$	$5.23 \times 10^{-16}$	$5.23 \times 10^{-16}$	$5.23 \times 10^{-16}$

C-35

- The model was initialized at hydrostatic conditions based on heads in the Rustler Formation.
- The base of the shaft, at the repository horizon, was held at atmospheric conditions. The pressure at the repository horizon will increase after closure in response to far-field pressures and waste-generated gas. This assumption maintains a large downward potential gradient.

Assumptions relevant to all numerical calculations in this appendix are listed in Section C2.

Except for isolated regions, the Rustler Formation will likely resaturate the DRZ and adjacent rock surrounding the shaft liner in a relatively short period. However, performance models show that the lower-shaft seal system will not resaturate with brine and repressurize to ambient pressures for at least 100 years. Under variably saturated conditions along the shaft, brine flow rates are expected to be less than those provided in this analysis.

#### **C4.2.2 Numerical Method**

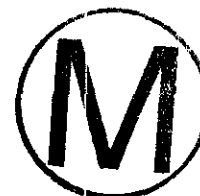
The modeling for this investigation was conducted using SWIFT II (Sandia Waste Isolation, Flow, and Transport Code), Version 2F. SWIFT II is a fully transient three-dimensional, finite-difference code that solves the coupled equations for single-phase flow and transport in porous and fractured geologic media. SWIFT II was selected because it is versatile and has been extensively verified against analytical results.

SWIFT II is supported by comprehensive documentation and an extensive testing history. Reeves et al. (1986a) discuss the theory and implementation of the code and basic limitations of the methodology. A guide to the input data is provided by Reeves et al. (1986b). Comparisons of the results from SWIFT II to analytical solutions appear in Finley and Reeves (1981), Reeves et al. (1987), and Ward et al. (1984).

#### **C4.2.3 Model Geometry and Boundary Conditions**

The full-shaft model was implemented with the cylindrical grid shown in Figures C-3a and C-3b. This grid extends vertically from the shaft station monolith at elevation 387.4 m (1271.0 ft) msl up through the Rustler Formation to an elevation of 872.6 m (2862.7 ft) msl. The grid extends radially from the center of the shaft out to an outer radius of 30.9 m (101.4 ft). It is composed of 19 radial columns and 99 vertical layers. Tables C-14 and C-15 provide details of the grid representing various seal components and host rock units.

Layer thicknesses (Table C-17) and column widths (Table C-18) are chosen so that they will adequately resolve the flow field within each seal component and each unit of the host formation without unduly compromising computational efficiency. Consistent with the first-order analysis of Van Sambeek et al. (1993), the total DRZ width (0.370 m) represents approximately 12% of the shaft radius (3.09 m).



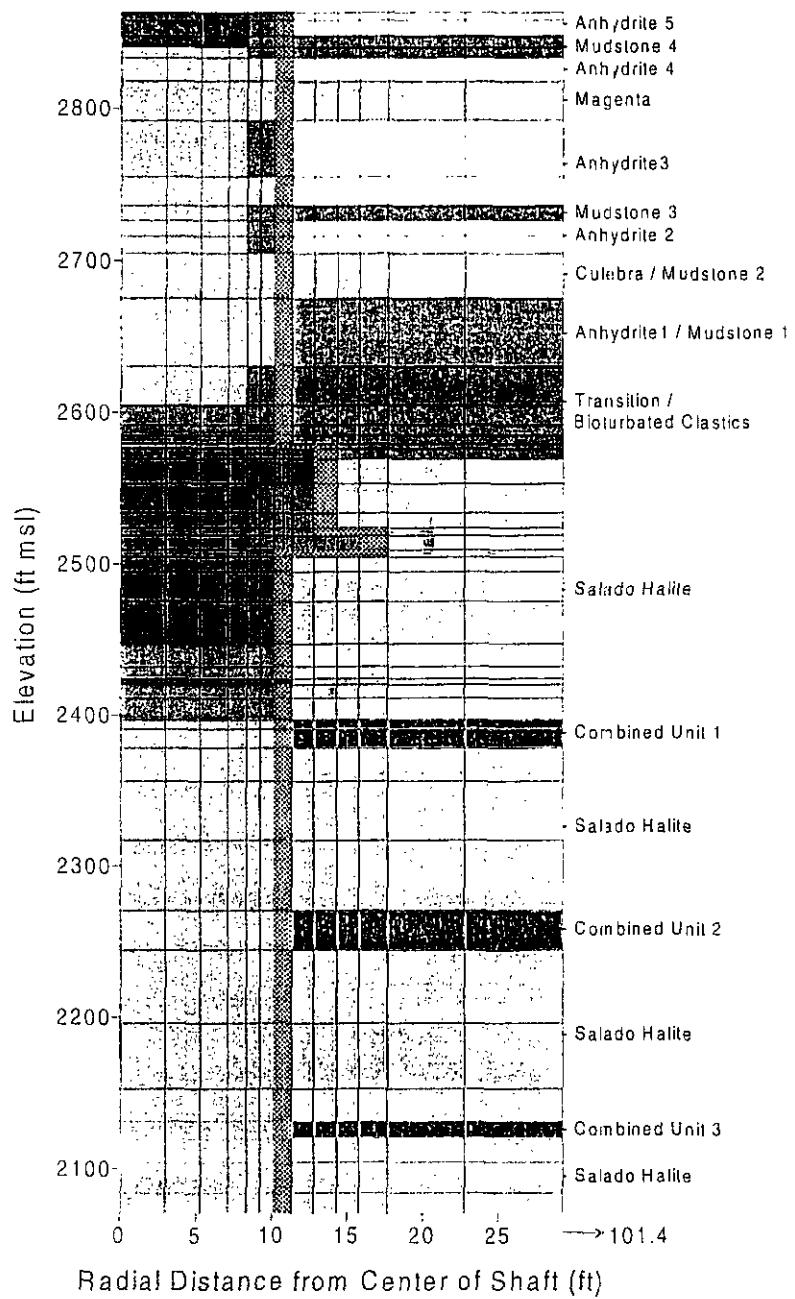


Figure C-3a. Full shaft model grid (top).

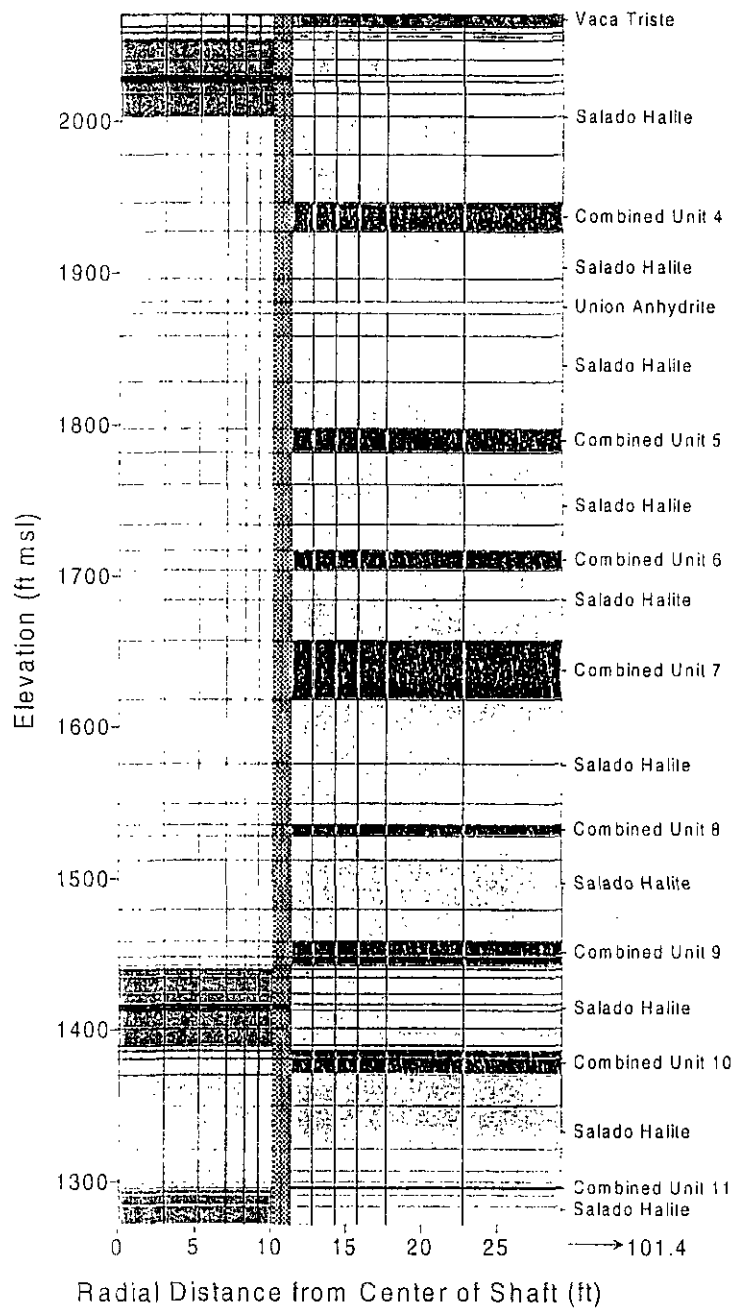
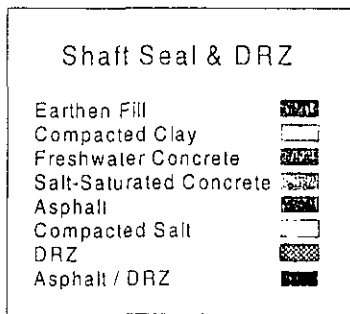


Figure C-3b. Full shaft model grid (bottom).



Table C-17. Full-Shaft Model Vertical Layers

Layer Number	Layer Thickness (m)	Shaft Seal Component	Host Formation Unit
1 (TOP)	1.52	Earthen Fill	Anhydrite 5
2	3.11	Earthen Fill	Anhydrite 5
3	2.29	Earthen Fill	Mudstone 4
4	2.13	Rustler Compacted Clay Column	Mudstone 4
5	4.69	Rustler Compacted Clay Column	Anhydrite 4
6	7.82	Rustler Compacted Clay Column	Magenta
7	11.26	Rustler Compacted Clay Column	Anhydrite 3
8	5.80	Rustler Compacted Clay Column	Anhydrite 3
9	2.90	Rustler Compacted Clay Column	Mudstone 3
10	3.15	Rustler Compacted Clay Column	Anhydrite 2
11	3.41	Rustler Compacted Clay Column	Anhydrite 2
12	8.99	Rustler Compacted Clay Column	Culbera/Mudstone 2
13	13.72	Rustler Compacted Clay Column	Anhydrite 1/Mudstone 1
14	7.76	Rustler Compacted Clay Column	Transition/Bioturbated Clastics
15	4.02	Concrete Plug	Transition/Bioturbated Clastics
16	2.07	Concrete Plug	Transition/Bioturbated Clastics
17	1.72	Asphalt Column	Transition/Bioturbated Clastics
18	1.02	Asphalt Column	Transition/Bioturbated Clastics
19	2.04	Asphalt Column	Transition/Bioturbated Clastics
20	4.97	Asphalt Column	Salado Halite
21	5.86	Asphalt Column	Salado Halite



Table C-17. Full-Shaft Model Vertical Layers

Layer Number	Layer Thickness (m)	Shaft Seal Component	Host Formation Unit
22	3.00	Asphalt Column	Salado Halite
23	1.50	Asphalt Column	Salado Halite
24	2.90	Asphalt Column	Salado Halite
25	1.50	Asphalt Column	Salado Halite
26	3.00	Asphalt Column	Salado Halite
27	6.00	Asphalt Column	Salado Halite
28	8.55	Asphalt Column	Salado Halite
29	4.57	Upper Concrete Plug	Salado Halite
30	2.44	Upper Concrete Plug	Salado Halite
31	1.22	Asphalt Waterstop	Salado Halite
32	2.71	Upper Concrete Plug	Salado Halite
33	4.30	Upper Concrete Plug	Salado Halite
34	1.93	Upper Salado Compacted Clay Column	Combined Unit 1
35	3.86	Upper Salado Compacted Clay Column	Combined Unit 1
36	6.76	Upper Salado Compacted Clay Column	Salado Halite
37	11.92	Upper Salado Compacted Clay Column	Salado Halite
38	14.08	Upper Salado Compacted Clay Column	Salado Halite
39	8.05	Upper Salado Compacted Clay Column	Combined Unit 2
40	14.74	Upper Salado Compacted Clay Column	Salado Halite
41	13.00	Upper Salado Compacted Clay Column	Salado Halite
42	6.50	Upper Salado Compacted Clay Column	Salado Halite
43	3.57	Upper Salado Compacted Clay Column	Combined Unit 3

Table C-17. Full-Shaft Model Vertical Layers

Layer Number	Layer Thickness (m)	Shaft Seal Component	Host Formation Unit
44	4.87	Upper Salado Compacted Clay Column	Salado Halite
45	6.13	Upper Salado Compacted Clay Column	Salado Halite
46	4.27	Upper Salado Compacted Clay Column	Salado Halite
47	2.44	Upper Salado Compacted Clay Column	Vaca Triste
48	1.22	Upper Salado Compacted Clay Column	Salado Halite
49	1.52	Upper Salado Compacted Clay Column	Salado Halite
50	3.90	Middle Concrete Plug	Salado Halite
51	3.12	Middle Concrete Plug	Salado Halite
52	1.22	Asphalt Waterstop	Salado Halite
53	2.44	Middle Concrete Plug	Salado Halite
54	4.57	Middle Concrete Plug	Salado Halite
55	7.65	Compacted Salt Column	Salado Halite
56	9.69	Compacted Salt Column	Salado Halite
57	5.79	Compacted Salt Column	Combined Unit 4
58	9.49	Compacted Salt Column	Salado Halite
59	4.57	Compacted Salt Column	Salado Halite
60	2.29	Compacted Salt Column	Union Anhydrite
61	4.57	Compacted Salt Column	Salado Halite
62	9.17	Compacted Salt Column	Salado Halite
63	9.45	Compacted Salt Column	Salado Halite
64	4.72	Compacted Salt Column	Combined Unit 5
65	6.41	Compacted Salt Column	Salado Halite
66	8.17	Compacted Salt Column	Salado Halite
67	5.24	Compacted Salt Column	Salado Halite
68	3.96	Compacted Salt Column	Combined Unit 6
69	0.00	Compacted Salt Column	Salado Halite

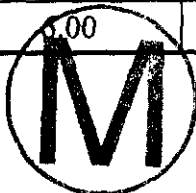


Table C-17. Full-Shaft Model Vertical Layers

Layer Number	Layer Thickness (m)	Shaft Seal Component	Host Formation Unit
70	8.33	Compacted Salt Column	Salado Halite
71	11.83	Compacted Salt Column	Combined Unit 7
72	12.97	Compacted Salt Column	Salado Halite
73	8.00	Compacted Salt Column	Salado Halite
74	4.25	Compacted Salt Column	Salado Halite
75	2.29	Compacted Salt Column	Combined Unit 8
76	4.88	Compacted Salt Column	Salado Halite
77	9.95	Compacted Salt Column	Salado Halite
78	6.52	Compacted Salt Column	Salado Halite
79	3.11	Compacted Salt Column	Combined Unit 9
80	1.65	Compacted Salt Column	Combined Unit 9
81	0.82	Compacted Salt Column	Salado Halite
82	1.65	Lower Concrete Plug	Salado Halite
83	3.23	Lower Concrete Plug	Salado Halite
84	2.13	Lower Concrete Plug	Salado Halite
85	1.22	Asphalt Waterstop	Salado Halite
86	3.63	Lower Concrete Plug	Salado Halite
87	3.38	Lower Concrete Plug	Salado Halite
88	1.13	Lower Salado Compacted Clay Column	Salado Halite
89	1.52	Lower Salado Compacted Clay Column	Combined Unit 10
90	3.18	Lower Salado Compacted Clay Column	Combined Unit 10
91	6.33	Lower Salado Compacted Clay Column	Salado Halite
92	8.66	Lower Salado Compacted Clay Column	Salado Halite
93	4.39	Lower Salado Compacted Clay Column	Salado Halite
94	2.19	Lower Salado Compacted Clay Column	Salado Halite



Table C-17. Full-Shaft Model Vertical Layers

Layer Number	Layer Thickness (m)	Shaft Seal Component	Host Formation Unit
95	1.10	Lower Salado Compacted Clay Column	Salado Halite
96	0.49	Shaft Station Monolith	Combined Unit 11
97	1.16	Shaft Station Monolith	Salado Halite
98	2.19	Shaft Station Monolith	Salado Halite
99 (BOTTOM)	3.78	Shaft Station Monolith	Salado Halite

Table C-18. Full-Shaft Model Radial Gridding

Column Number	Radius to Outer Grid Column Boundary (m)	Model Component(s)
1	0.90	Seal
2	1.60	Seal
3	2.15	Seal
4	2.53	Seal
5	2.80	Liner, Seal
6	3.09	Liner, Seal
7	3.27	DRZ, Liner, Seal
8	3.46	DRZ, Liner, Seal
9	3.90	Host Rock, Liner, DRZ, Seal
10	4.37	Host Rock, Liner, DRZ
11	4.81	Host Rock, Liner, DRZ
12	5.39	Host Rock, DRZ
13	6.94	Host Rock
14	8.90	Host Rock
15	11.42	Host Rock
16	14.66	Host Rock
17	18.81	Host Rock
18	24.14	Host Rock
19	30.9	Host Rock



Because the outer boundary condition accurately characterizes an infinite aquifer, it is unnecessary to extend the radial grid to large distances. The radial boundary was fixed at 30.9 m (10 shaft radii), a distance sufficient to capture any vertical flow components that may arise in the host rock during the shaft resaturation process. Beyond the outermost extent of the seal components (4.81 m), a node-distributed grid is used because it is most appropriate for a radially converging flow field. Here coordinates of the nodal points increase in geometric progression, as recommended by Aziz and Settari (1979, p. 87).

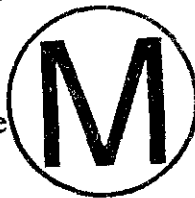
Grid sensitivities are not expected. For liquid flow, flow rates are sufficiently small that the chosen level of refinement can resolve pressure gradients. It is important to resolve such gradients because they control the rates at which groundwater moves downward through seal components and radially inward through host rock.

For gas flow as simulated with a similar grid in Model 2, the situation is quite different. Within seal components lying below the lower seal, gas pressurization times are sufficiently small in comparison to the time required for salt-column reconsolidation that it is unnecessary to resolve gradients in the pressure front with either spatial or temporal discretization. Rather, grid refinement must be focused on the critical lower seal components and the DRZ that surrounds them. Here it is essential to resolve pressure gradients.

After DRZ healing, permeabilities of these components are sufficiently small so that long-term pressure gradients can be maintained, thus limiting gas pressurization of the salt columns as desired. Current results of two-phase simulations indicate that this grid is sufficiently refined to show substantially limited gas flows. Although some level of grid sensitivity could be present for gas flow within the lower seal components and surrounding DRZ, further refinement would yield only steeper pressure gradients and even smaller gas flow rates into the salt column.

For the model to accurately represent formation conditions at the time of closure, a pre-closure period was simulated. Therefore the modeling was conducted in two stages. The pre-closure period extended from the time of shaft excavation to the time of shaft closure. The duration was assumed to be 50 years. The shaft was considered to be instantaneously excavated, and development of the DRZ was considered to occur instantaneously after shaft excavation. The initial pressure conditions, in the portions of the system other than the open shaft, were represented by hydrostatic equilibrium based on an undisturbed head of 927 m msl at the center of the Culebra and a single-density fluid of 1230 kg/m<sup>3</sup>. The pressure in the open shaft was held at 1 atm for the duration of the pre-closure simulation. No-flow boundary conditions were imposed at the top and bottom of the model. Infinite aquifer boundary conditions were set at the outer edge of the modeled region. The model components for the pre-closure simulation were the open shaft, the existing shaft liner, the DRZ, and the undisturbed formation.

The purpose of pre-closure modeling was to develop the pressure distribution in the formations created by the open shaft. For the post-closure period, the shaft was sealed and the initial grid-block pressures were set equal to the final grid-block pressures of the pre-closure simulation. Sealing of the shaft was considered to occur instantaneously. To maximize the driving force between the Rustler Formation and the bottom of the shaft, atmospheric pressure was maintained at the bottom of the shaft and DRZ. Otherwise, no-flow boundary conditions were imposed at the bottom and top of the model and along the vertical boundary at the center of



the shaft. Infinite aquifer boundary conditions were set at the outer edge of the modeled region. The model components for the post-closure simulation were the earthen fill, freshwater concrete, salt-saturated concrete, asphalt, compacted clay, crushed salt, the existing shaft liner, the DRZ, and the undisturbed formation. Freshwater concrete was assigned properties identical to those specified for salt-saturated concrete.

#### C4.2.4 Model Parameters

The model parameters were discussed in detail in Section C3. As reported in that section, permeabilities within the compacted salt column and within the Salado DRZ are transient (see Tables C-5 and C-16). Figures C-4 and C-5 illustrate the model permeabilities for the base-case simulation during the open-shaft period, at closure ( $t = 0$  years), at 2 years ( $t = 2$ ), and at 200 years ( $t = 200$ ). These figures demonstrate the transient nature of the DRZ and compacted salt column permeabilities. These figures offer a method to integrate all of the permeability information provided in the tables in Section C3.

The base-case simulation assumed that the anhydrites in the Rustler Formation and anhydrites greater than 3 m thick in the Salado Formation had no DRZ (based on mechanical modeling results presented in Appendix D). This condition results in a discontinuous DRZ at the time of closure (see Figure C-4, second panel), as discussed in Section C3.5.1. Although this case could be realistic, a second case (Run 2) was considered to allow assessment of the impact of the discontinuous DRZ. The relationship developed for the Salado DRZ (Equation C-3) was applied to all lithologies for Run 2, resulting in a continuous DRZ along the shaft wall. Run 2 included concrete-asphalt waterstops that completely healed the adjacent DRZ after two years.

Run 3 was a sensitivity simulation to examine the impact of the concrete-asphalt waterstops. Run 3 incorporated a continuous DRZ at the time of shaft closure, as in Run 2. However, in contrast to Run 2, the DRZ adjacent to the concrete-asphalt waterstops was allowed to heal at the same rate as the DRZ adjacent to the concrete of the plugs, rather than in two years. Table C-19 summarizes the three simulations, highlighting the principal differences among them.

Table C-19. Performance Model 1 Simulations

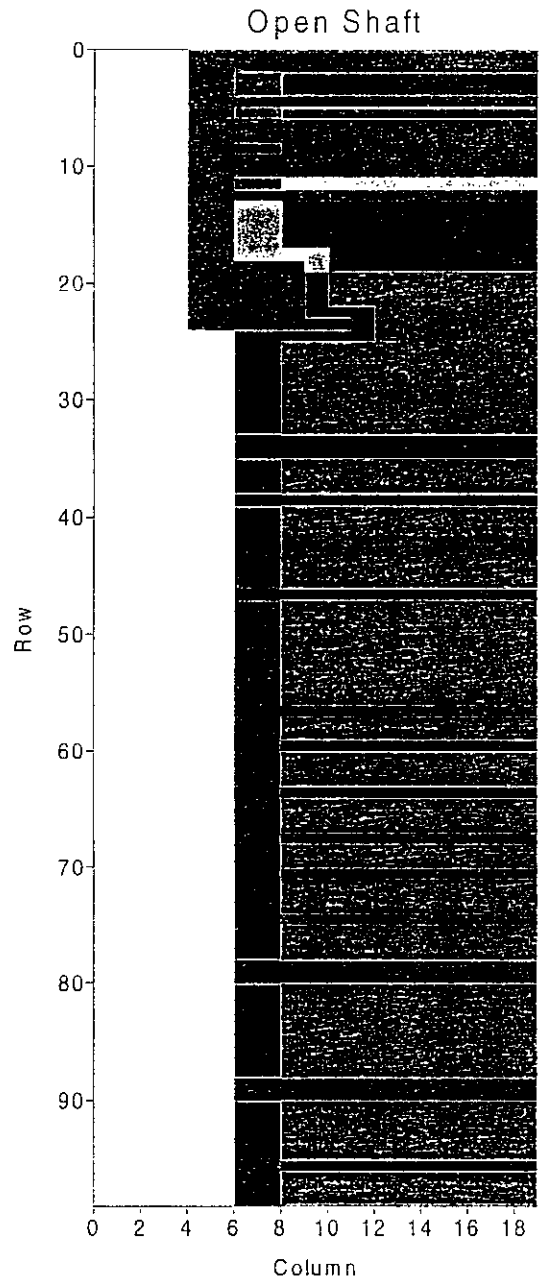
Run	DRZ	Waterstops
1 (Base-Case)	Discontinuous	Yes
2	Continuous	Yes
3	Continuous	No



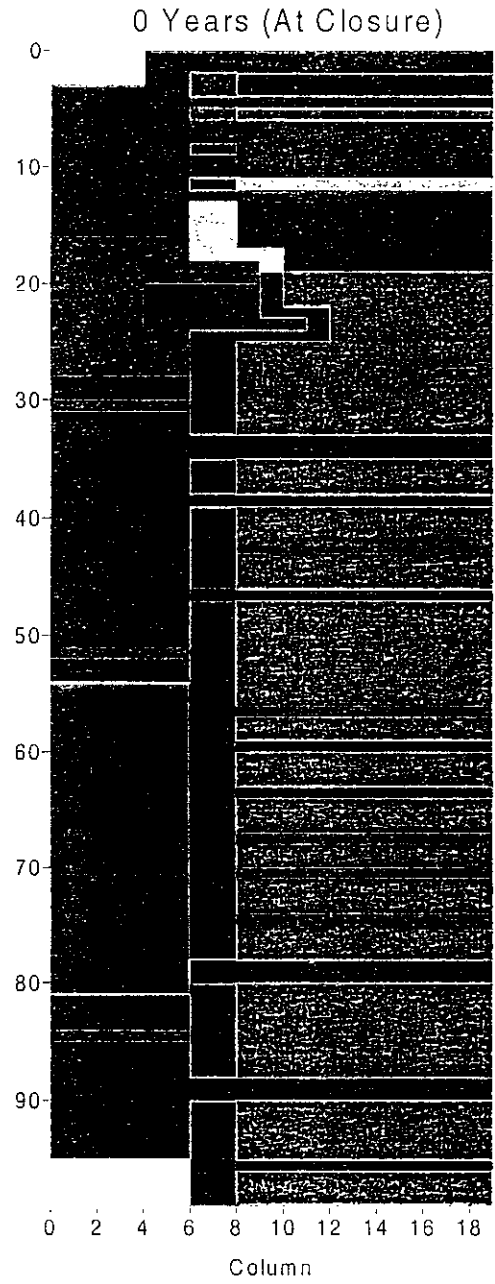
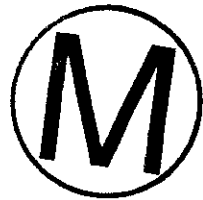
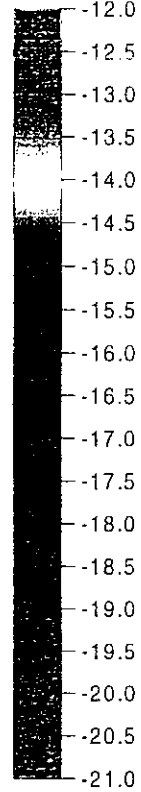
#### C4.3 Performance Model Results

Simulation results for Performance Model 1 are presented in terms of brine flow rates ( $m^3/yr$ ), cumulative flow ( $m^3$ ), and pressure distribution plots. Figure C-6 shows calculated brine flow rates for Runs 1 through 3 measured at the Rustler/Salado contact and at the top and bottom of the compacted salt column. Although the simulations continued out to 1000 years after shaft closure, the brine flow values were plotted to only 50 years because flow rates diminished to less than  $0.03 m^3/yr$  by that time.

C-46



Log k (m<sup>2</sup>)



Log k (m<sup>2</sup>)

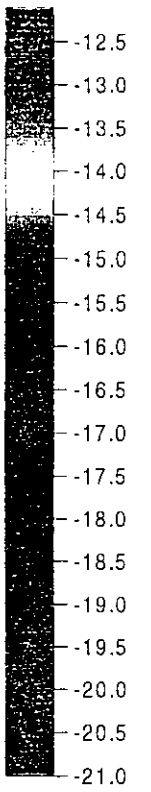


Figure C-4. Permeability fields for Run 1 (base case).

C-47

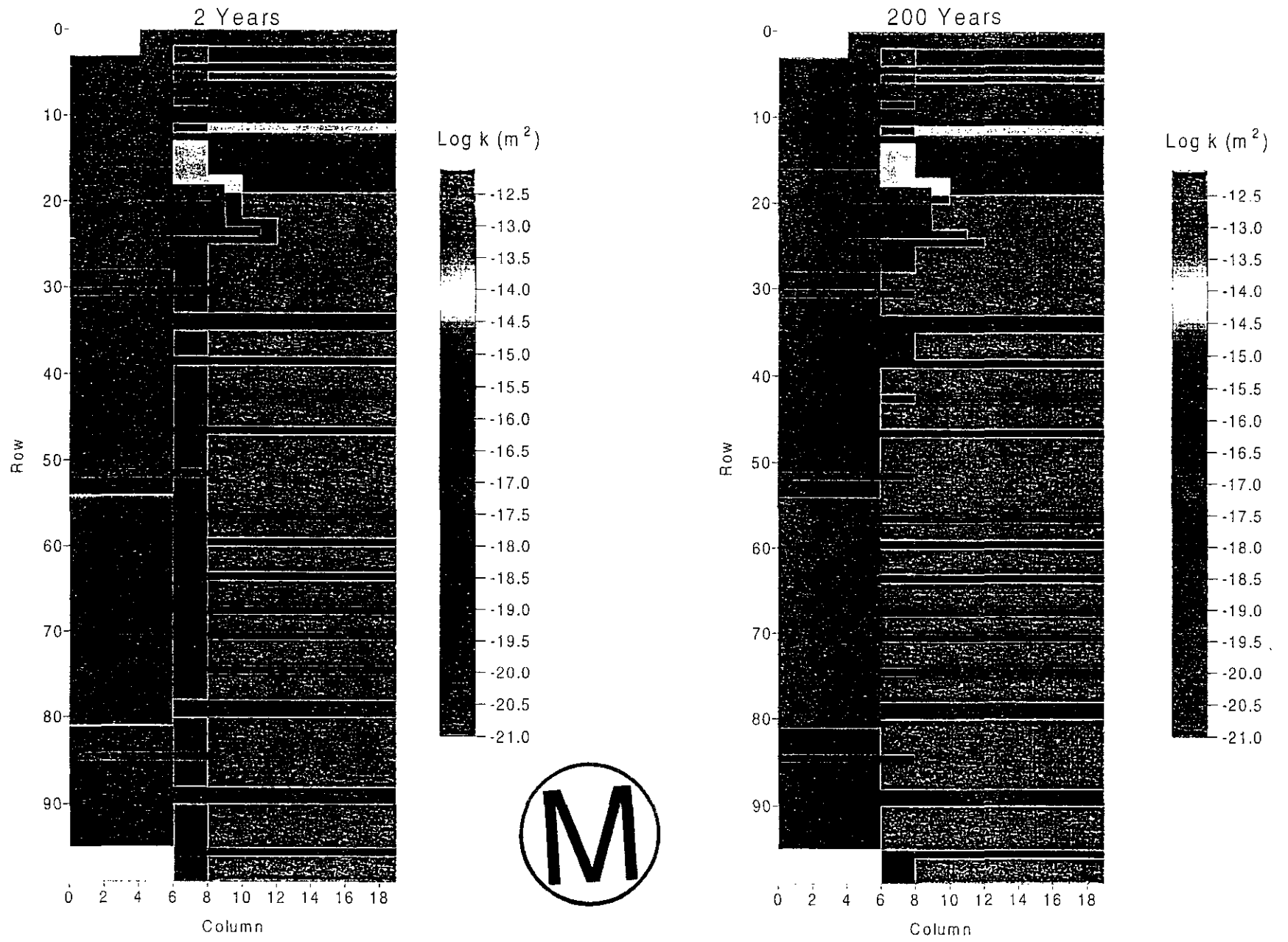


Figure C-5. Permeability fields for Run 1 (base case).

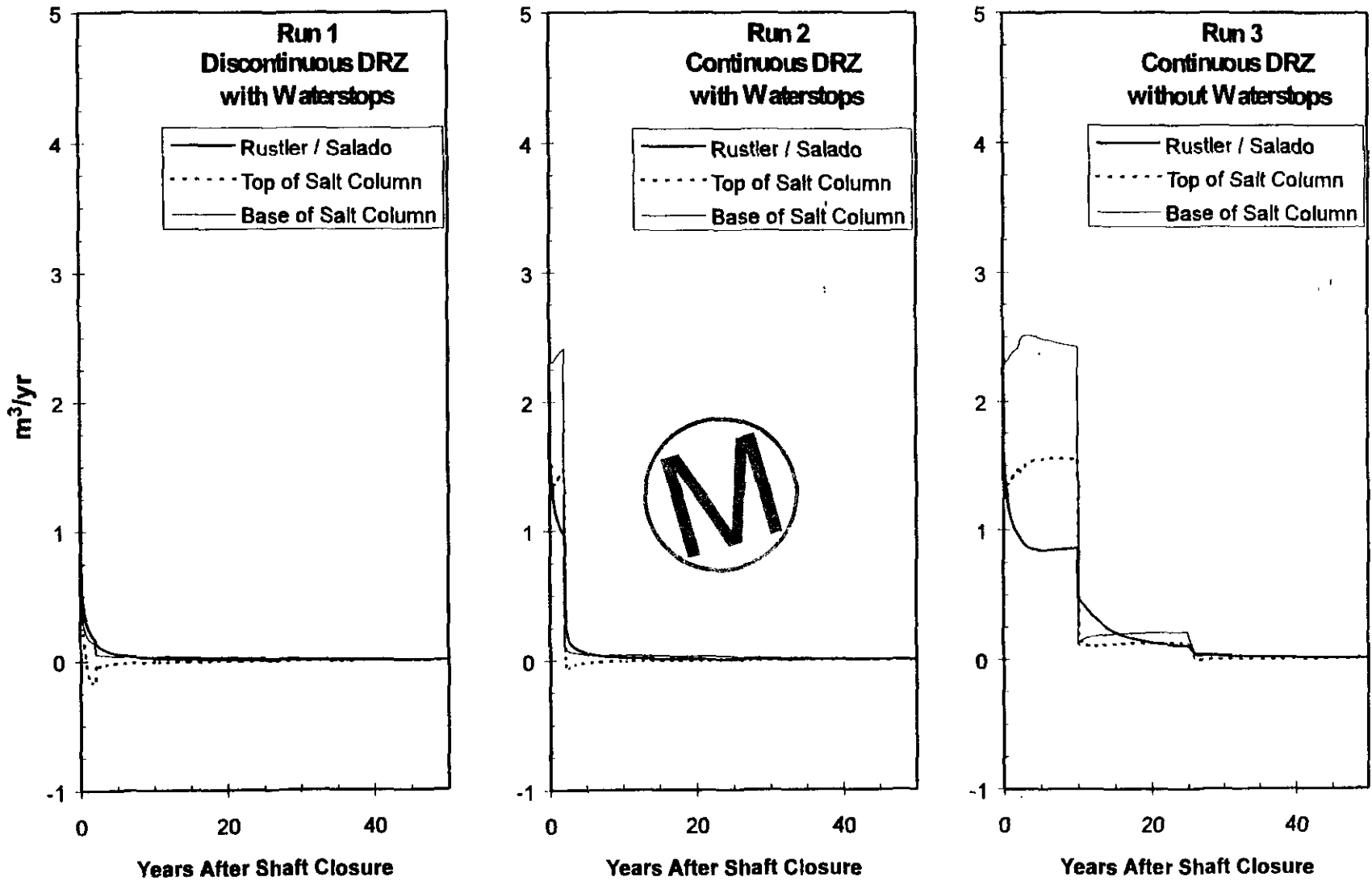


Figure C-6. Model 1 flow rates.

Figure C-7 shows the cumulative flow at 200 years measured at the Rustler/Salado contact and the top and bottom of the compacted salt column. Flow for each level for each run was divided into three components: flow through the shaft seal materials, flow through the DRZ, and flow through the intact host rock out to a radial distance of 10 shaft radii. As expected, flow through the intact rock was minimal for all cases. In Runs 2 and 3, where the DRZ is continuous, the amount of flow moving down through the seal system increased as a function of depth. This was a product of the model boundary conditions that direct formation fluids through the base of the shaft. In Run 1, the combination of a discontinuous DRZ and the waterstops created a pressure sink within and adjacent to the upper Salado compacted clay column. The small amount of flow moving down across the Rustler/Salado contact was used to repressurize the sink and did not migrate past the top of the compacted salt column.

The flow volumes predicted by Model 1 provided an estimate of the number of seal component pore-volumes that will pass through a given seal component. This exercise provides a useful method of quantifying flow estimates and is useful in the evaluation of seal material longevity. The total volume passing across the Rustler/Salado contact, the top of the compacted salt column, and the bottom of the compacted salt column was estimated for a 10,000-year period. Because the simulation did not extend for 10,000 years, the last simulated flow rate was used as a constant for times greater than the simulation time. As discussed in Section C4.2.1, the flow direction will reverse as the system equilibrates. The estimated flow volumes presented here are therefore maximum values.

The flow volumes were estimated for the top of the Salado concrete seal components and the compacted clay components. These flow volumes were then converted to total number of pore-volumes for a given seal component. The largest number of pore volumes predicted to flow through any Salado concrete component was 4. This calculation does not account for the volume of the asphalt waterstop. The largest number of pore volumes that flowed through any Salado compacted clay column was 0.4 for the lower Salado compacted clay column.

Figures C-8 and C-9 illustrate the change in pressure distribution with time for Run 1 (Discontinuous DRZ with Waterstops). All pressures are referenced to the elevation at the base of the model. The first panel of Figure C-8 shows the pressure drawdown at the end of the open shaft period just before shaft closure. The second panel shows the pressure profile just prior to activation of the waterstops. The first of the two panels shown in Figure C-9 illustrates the effect of the waterstops. The final panel in this sequence shows that most of the model has been repressurized by 200 years after shaft closure.

The potential for dissolution of salt in the Salado DRZ was introduced in Section C3.5. The results of Model 1 can be used to estimate the volume of salt that could be dissolved. Run 1 of the performance model predicts a maximum of about 1000 kg ( $1 \text{ m}^3$ ) of groundwater will migrate into the Salado DRZ. A maximum of about  $0.14 \text{ m}^3$  of salt could be dissolved in this quantity of groundwater. The DRZ adjacent to the asphalt column contains approximately  $1700 \text{ m}^3$  of salt. Dissolution of  $0.14 \text{ m}^3$  of salt constitutes less than 0.01% of the DRZ volume. Therefore the probability that dissolutions will impact performance is exceedingly low.





C-50

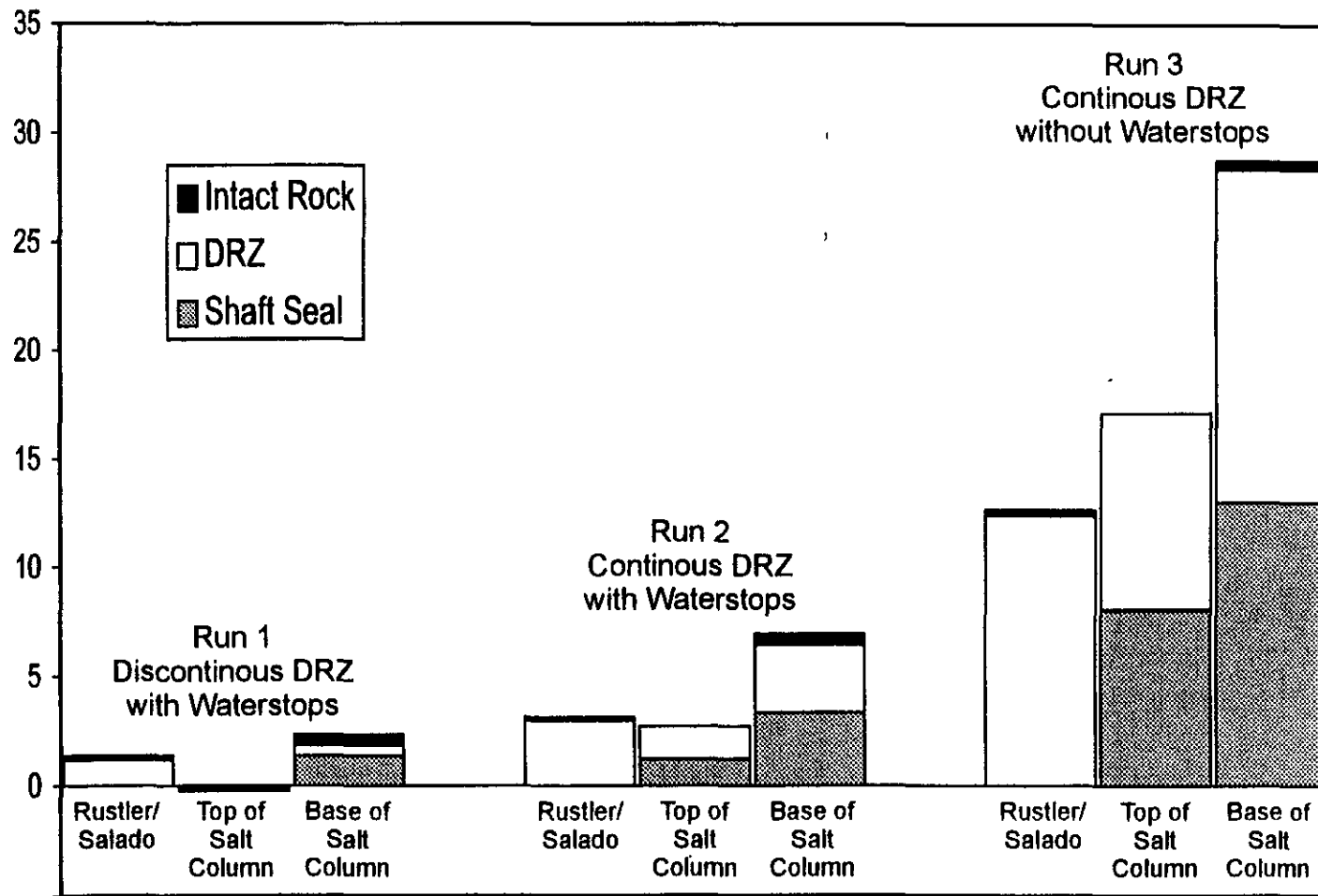


Figure C-7. Cumulative flow at 200 years.

C-51

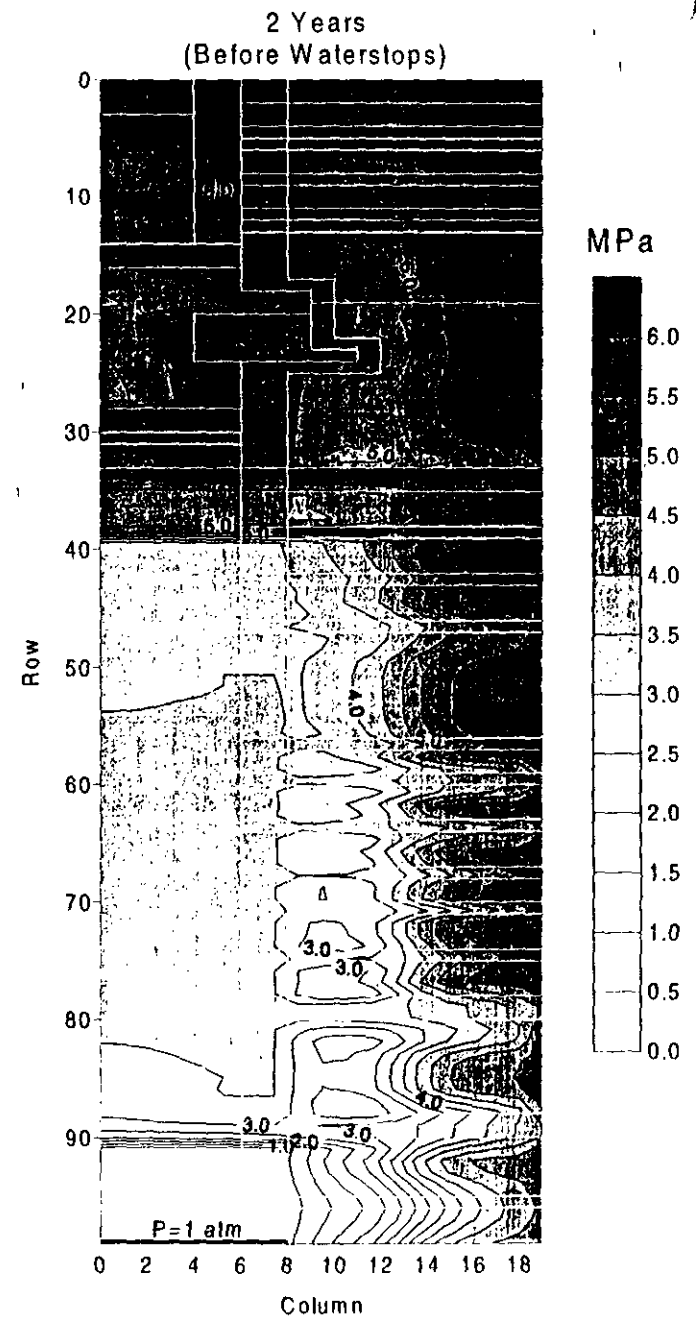
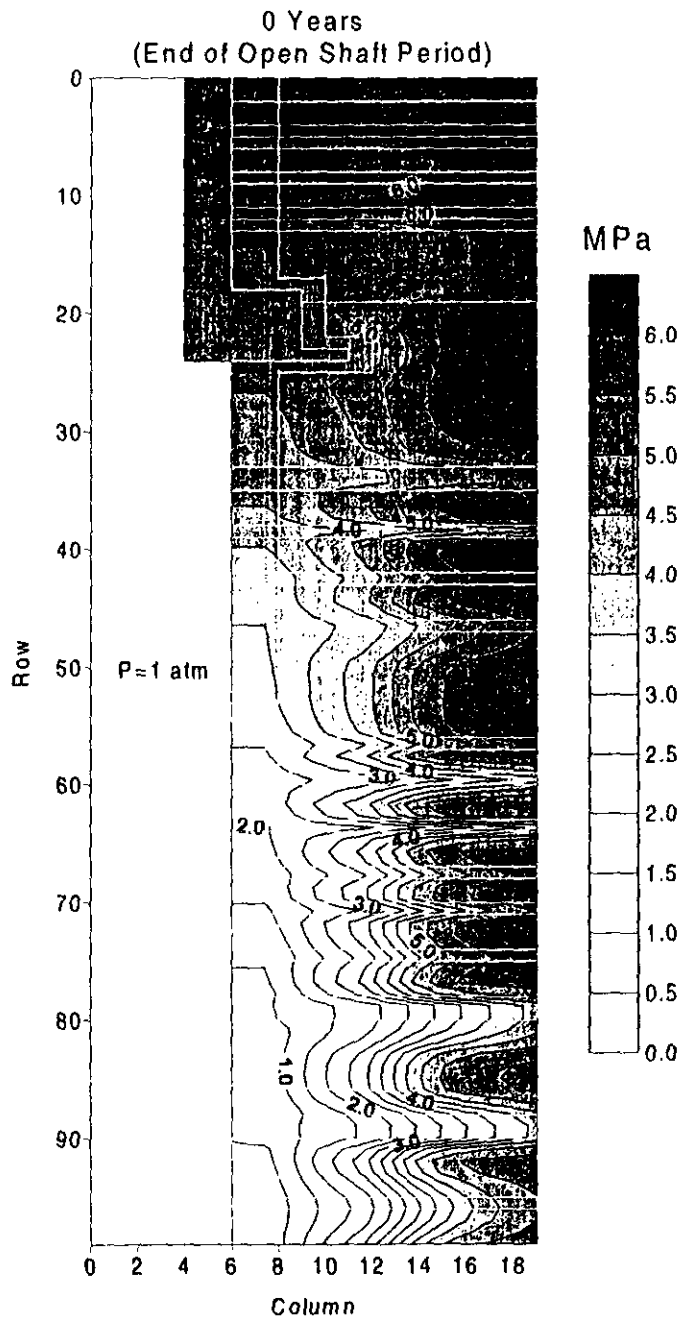


Figure C-8. Pressure distributions for Run 1 (base case).

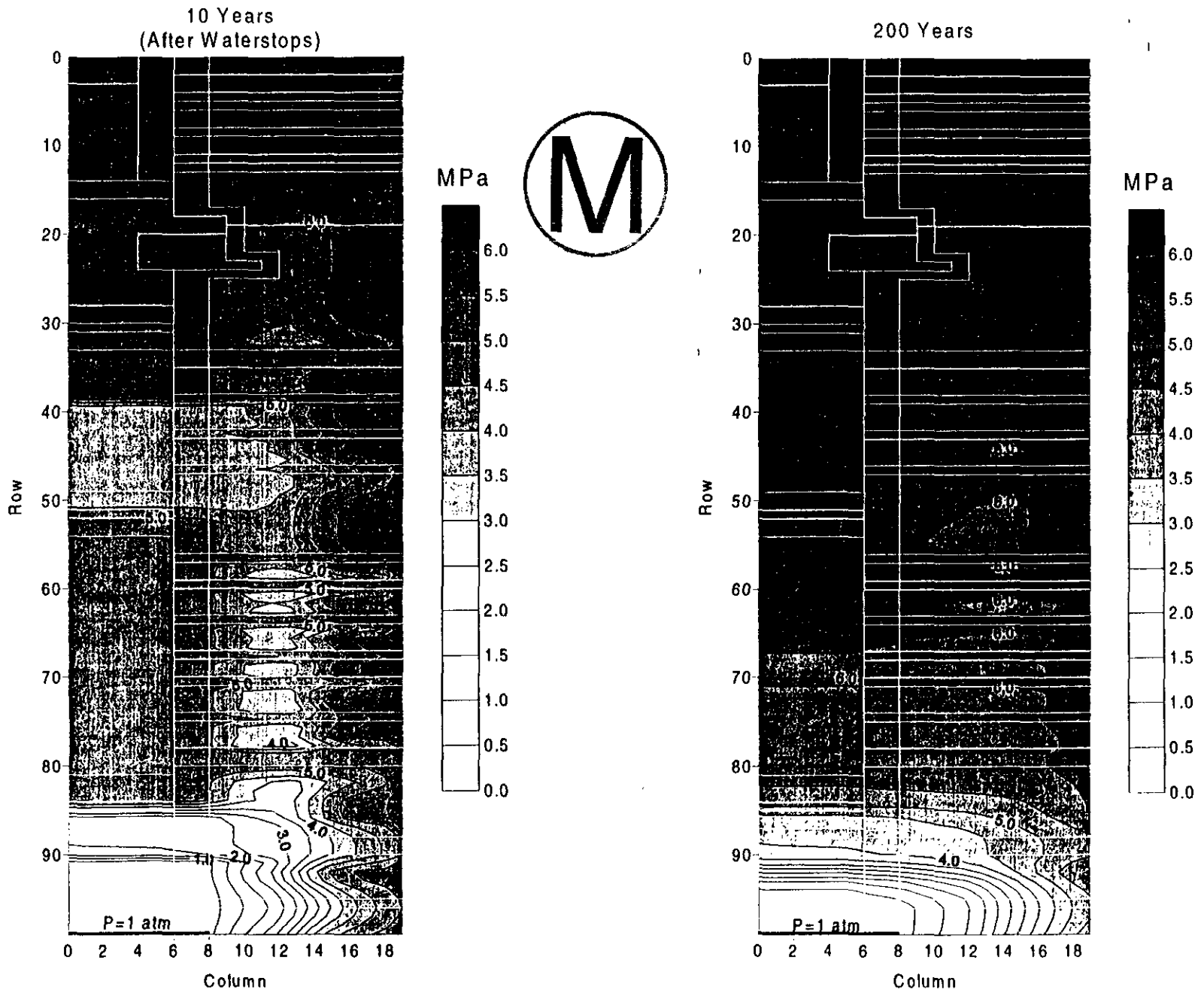


Figure C-9. Pressure distributions for Run 1 (base case).

## **C5. GAS MIGRATION AND CONSOLIDATION OF COMPACTED SALT COLUMN (MODEL 2)**

### **C5.1 Statement of Problem**

The compacted salt column seal component is approximately 172 m (563 ft) long and located between elevations 439 m (1440 ft) msl and 611 m (2003 ft) msl in the proposed seal system design. This seal system component is composed of compacted crushed Salado salt, initially partially saturated with small amounts of water. After closure, as the host formation creeps inward, the crushed salt is expected to consolidate to a density and permeability condition comparable to that of the Salado host rock, thus creating a permanent, chemically compatible, low permeability seal component. The consolidation process can potentially be affected by pore pressures in the salt column. The purpose of this analysis was to predict the effect of pressure increases due to fluid (brine or gas) movement within the lower shaft seal system on compacted salt column permeability during the early time period when consolidation is occurring.

Fluid movement into the salt column could occur from three different sources: (1) brine flow down the shaft from the Rustler Formation above, (2) gas flow up the shaft from the repository below, and (3) brine flow towards the shaft from the host Salado formation due to pressure gradients created during the period the shaft is open to atmospheric pressure. Relationships developed for salt column fractional density (Appendix D) as a function of depth, pressure, and time were combined with estimates for crushed salt permeability as a function of fractional density and used in the analysis to provide an estimate of salt column permeability as a function of depth and time during the first 200 years after seal emplacement. In addition to salt column permeability, model outputs to be analyzed include pressure in the salt column and gas flow from the repository past the lower concrete component into the salt column.

### **C5.2 Performance Model 2 Description**



#### **C5.2.1 Conceptual Model and Assumptions**

The schematic diagram in Figure C-10 shows the conceptualization of the flow system in the lower shaft region and the model components implemented by the compacted salt column performance model. The three sources of fluid flow that could contribute to pressure increases in the compacted salt column are shown in the diagram of the conceptual model (i.e., brine from the Rustler, brine from the host formation, and gas from the repository). Model components include the lower shaft seal components from the repository horizon to the top of the Vaca Triste interbed in the Salado Formation, a DRZ surrounding the shaft, and various anhydrite marker beds within the Salado Formation from the Vaca Triste to the repository horizon.

As discussed in Section C3, the DRZ was assumed to have progressively lower permeability as healing occurs with time after seal emplacement. The crushed salt of the compacted salt column was assumed to consolidate and achieve lower permeability with time at differing rates depending on depth within the column and the amount of pore-pressure back stress within the column.

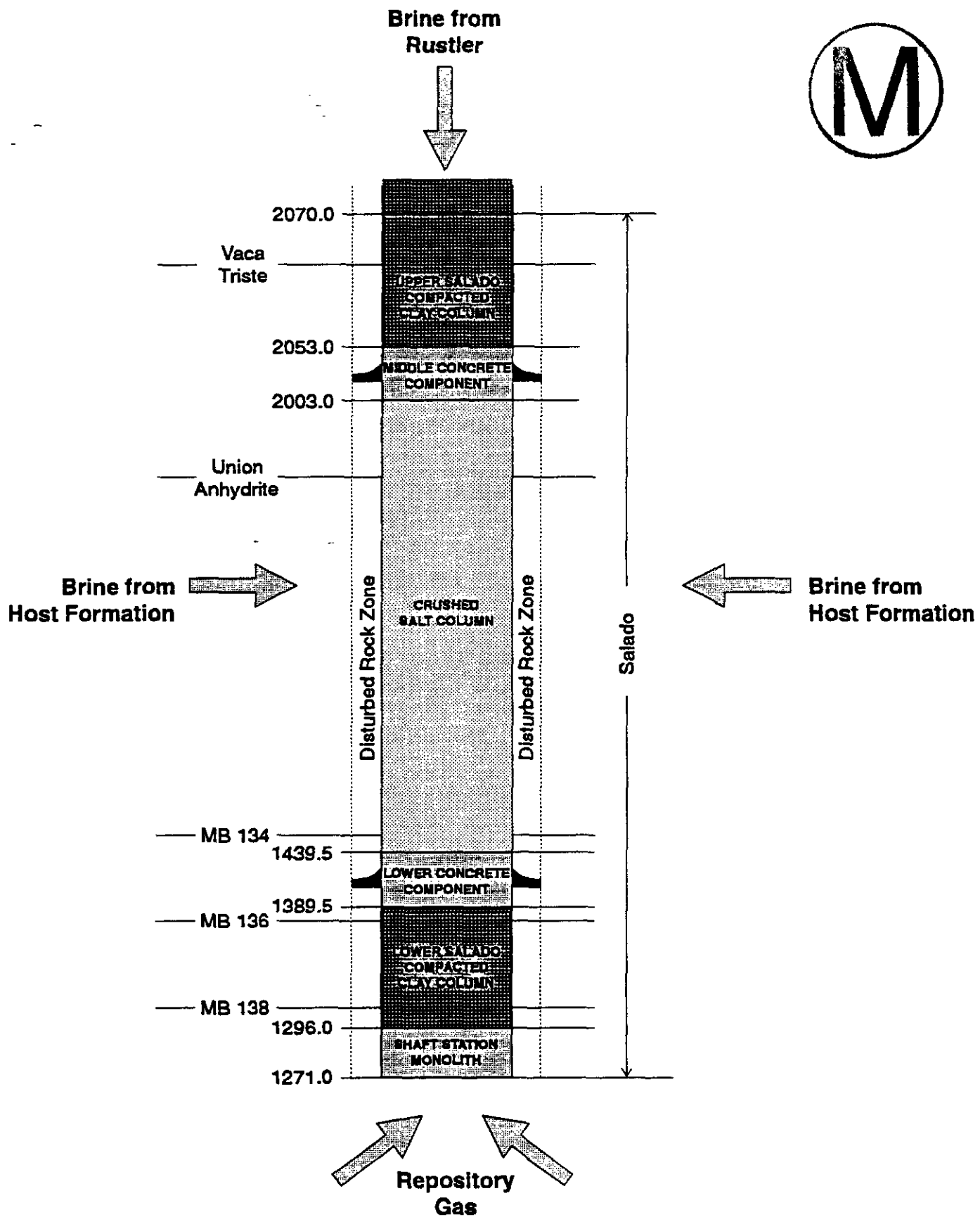


Figure C-10. Conceptual diagram of compacted salt column performance model components.

Results obtained from the full-shaft saturated flow model discussed in Section C4 indicate no brine flow down the shaft into the compacted salt column from the Rustler Formation for the case of a discontinuous DRZ, 2.7 m<sup>3</sup> for a continuous DRZ with waterstops, or 17.2 m<sup>3</sup> for the case of a continuous DRZ without waterstops. This volume of fluid was accounted for in the compacted salt column performance model by including it in the initial brine saturation of the crushed salt. The Rustler flow was distributed evenly throughout the entire pore space of the column by making an appropriate adjustment to initial salt column liquid saturation.

Pressure increase resulting from gas generation within the repository was simulated by applying an increasing gas pressure boundary condition at the base of the shaft. The repository pressure was assumed to increase to 7 MPa in 100 years in one case and 14 MPa in 200 years in a second case. Additional assumptions included in the compacted salt column performance model are discussed in Section C2.

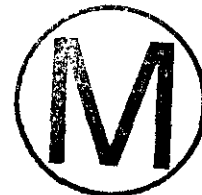
### **C5.2.2 Numerical Model**

The computer code used to implement the compacted salt column performance model is TOUGH28W, Version 2.02 (TOUGH2). TOUGH28W is a numerical simulation program for multi-dimensional coupled fluid and heat flows of multi-phase, multi-component fluid mixtures in porous and fractured media. This code was developed by Karsten Pruess at Lawrence Berkeley National Laboratory and has been used extensively in studies of high-level nuclear waste isolation in partially saturated geologic media (Pruess, 1991). TOUGH28W includes a number of fluid property equation-of-state modules. These modules make the code applicable to a variety of subsurface flow systems, including groundwater aquifers, unsaturated zones, and geothermal reservoirs. The version of the code used for this study incorporates the equation-of-state module EOS8W, which allows for simulation of the three phases water, air, and oil. This version includes a feature which optionally allows for specification of fluid properties representative of WIPP brine instead of water and hydrogen instead of air.

Version 2.02 includes a modification that permits specification of permeability as a function of time for specific model regions. This feature was included to simulate the reduction in permeability of the DRZ around the shaft attributable to healing after seal emplacement. The feature was implemented by allowing the user to provide as input a table specifying permeabilities at different values of the time variable and a rock type (i.e., region) to which the table applies. At each calculational time-step, the code will interpolate a permeability value from the table and apply that value to the specified region.

Version 2.02 also includes a modification to allow specification of permeability as a function of depth and pressure. This feature was included in order to simulate reconsolidation of the compacted salt column at differing rates depending on depth within the column and pore-pressure back stress. This feature was implemented by allowing the user to provide a table as input specifying the rate of change of permeability at different values of pore pressure and elevation for a specific rock type (i.e., region) to which the table applies. At each time-step for each grid element in the specified region, the rate of change in permeability obtained from the table is multiplied by the step size and applied to that grid element subject to specified minimum and maximum permeability values.





### C5.2.3 Model Geometry and Boundary Conditions

The compacted salt column performance model was implemented with the radially symmetric cylindrical grid shown in Figure C-11. The modeled region extends in the vertical direction from the base of the shaft at elevation 387 m (1271 ft) up to the top of the Vaca Triste unit at elevation 631 m (2070 ft). The modeled region extends in the radial direction from the center of the shaft to the outer radial boundary at 282 m (925 ft).

The radial extent of Figure C-11 is truncated at 100 ft in order to show shaft detail. The grid contains 25 columns of grid cells in the radial direction and 59 layers in the vertical direction. The innermost four columns of grid cells represent the shaft and associated seal materials, and the next two columns radially outward represent a DRZ surrounding the shaft. Seal components represented in the model include, from top to bottom:

- a small portion of the upper Salado compacted clay column,
- the middle concrete component including asphalt waterstop,
- the compacted salt column,
- the lower concrete component including asphalt waterstop,
- the lower Salado compacted clay column, and
- the shaft station concrete monolith.

Although the last component is represented in the model grid, no “credit” is taken for its sealing properties; thus the model permeability of the shaft station monolith was set relatively high ( $1 \times 10^{-14} \text{ m}^2$ ) when compared to other model permeabilities.

The host Salado Formation was modeled as layers of halite separated by several layers of anhydrite marker beds. Some of the interbeds that occur close together are combined in the model into single layers, as discussed in Section C3. Table C-20 provides details of the model grid layers representing the various seal components and host formation units. Table C-21 provides details of model gridding in the radial direction.

The leftmost model boundary was considered to be no-flow since this is the line of symmetry at the center of the shaft. The rightmost model boundary (i.e. the outer radial boundary) was assumed to be a constant pressure boundary at hydrostatic equilibrium relative to 12.5 MPa in MB139 near the base of the repository. A boundary radius of 282 m (926 ft) was determined by conducting a series of one-dimensional sensitivity runs to determine at what distance pressure response in the shaft was not sensitive to boundary location. The top and bottom model boundaries were assumed to be no-flow boundaries. This is a reasonable assumption for the time period considered in this model since pressure gradients are primarily directed radially inward because of the open-shaft condition during the repository operational period.

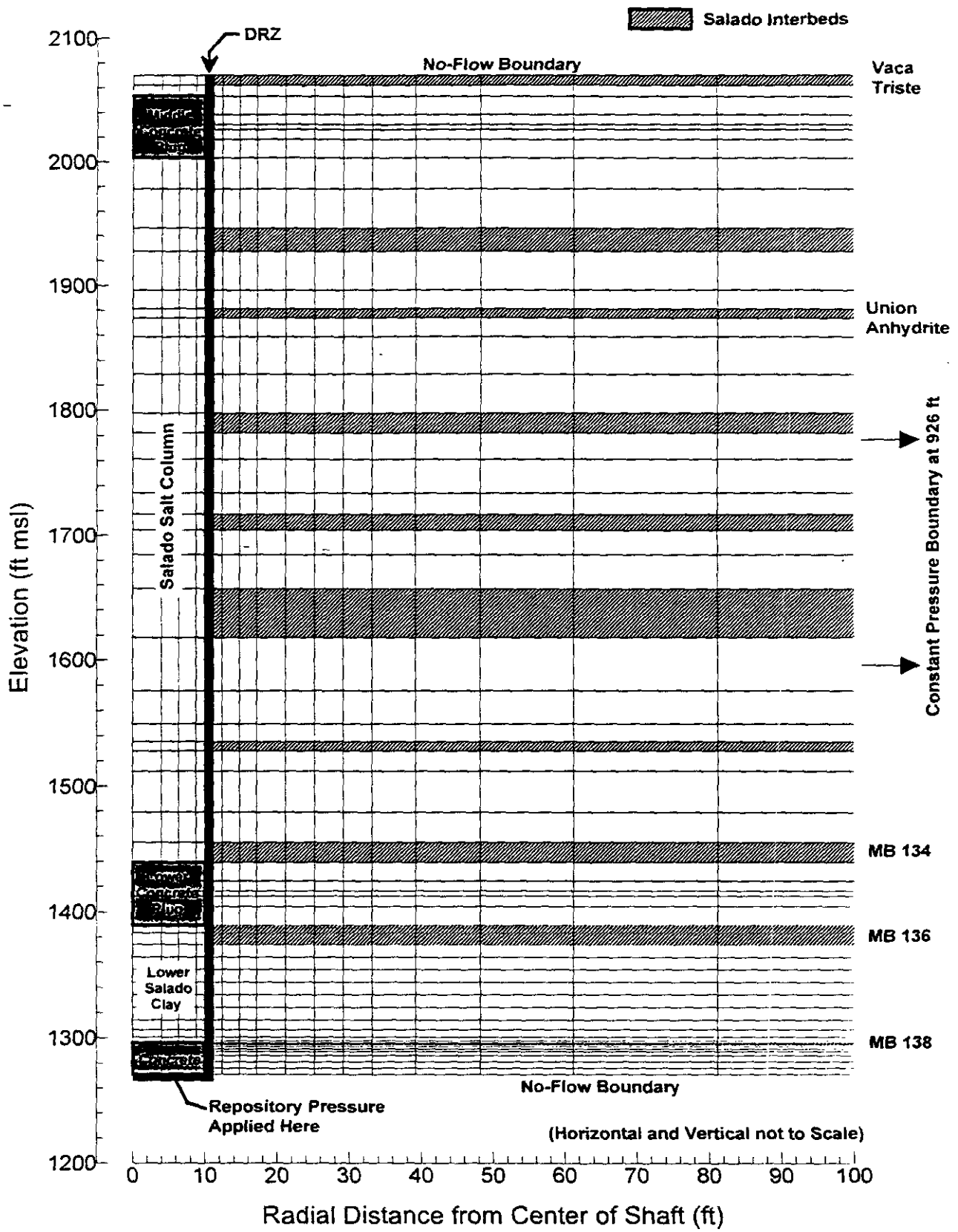


Figure C-11. Grid used by the compacted salt column performance model.





Table C-20. Vertical Layers of the Compacted Salt Column Performance Model

Layer Number	Layer Thickness (m)	Shaft Seal Component	Host Formation Unit
1 (TOP)	2.44	Upper Salado Compacted Clay Column	Vaca Triste
2	2.74	Upper Salado Compacted Clay Column	Salado Halite
3	4.57	Middle Concrete Plug	Salado Halite
4	2.44	Middle Concrete Plug	Salado Halite
5	1.22	Asphalt Waterstop	Salado Halite
6	2.44	Middle Concrete Plug	Salado Halite
7	4.57	Middle Concrete Plug	Salado Halite
8	7.65	Compacted Salt Column	Salado Halite
9	9.69	Compacted Salt Column	Salado Halite
10	5.79	Compacted Salt Column	Combined MB117 - MB122 and Zone A
11	9.49	Compacted Salt Column	Salado Halite
12	4.57	Compacted Salt Column	Salado Halite
13	2.29	Compacted Salt Column	Union Anhydrite
14	4.57	Compacted Salt Column	Salado Halite
15	9.17	Compacted Salt Column	Salado Halite
16	9.45	Compacted Salt Column	Salado Halite
17	4.72	Compacted Salt Column	Combined MB123 - MB124
18	6.41	Compacted Salt Column	Salado Halite
19	8.17	Compacted Salt Column	Salado Halite
20	5.24	Compacted Salt Column	Salado Halite
21	3.96	Compacted Salt Column	Combined Zone B - C and MB126
22	6.00	Compacted Salt Column	Salado Halite
23	8.33	Compacted Salt Column	Salado Halite
24	11.83	Compacted Salt Column	Combined MB127 - MB130 and Zones D - I
25	12.97	Compacted Salt Column	Salado Halite
26	8.00	Compacted Salt Column	Salado Halite

Table C-20. Vertical Layers of the Compacted Salt Column Performance Model

Layer Number	Layer Thickness (m)	Shaft Seal Component	Host Formation Unit
27	4.25	Compacted Salt Column	Salado Halite
28	2.29	Compacted Salt Column	Combined MB131 - MB133 and Zone J
29	4.88	Compacted Salt Column	Salado Halite
30	9.95	Compacted Salt Column	Salado Halite
31	7.35	Compacted Salt Column	Salado Halite
32	4.75	Compacted Salt Column	Combined MB134 - MB135
33	4.57	Lower Concrete Plug	Salado Halite
34	2.44	Lower Concrete Plug	Salado Halite
35	1.22	Asphalt Waterstop	Salado Halite
36	2.44	Lower Concrete Plug	Salado Halite
37	4.57	Lower Concrete Plug	Salado Halite
38	0.61	Lower Salado Compacted Clay Column	Combined MB136-MB137
39	1.22	Lower Salado Compacted Clay Column	Combined MB136-MB137
40	2.87	Lower Salado Compacted Clay Column	Combined MB136-MB137
41	3.05	Lower Salado Compacted Clay Column	Salado Halite
42	3.05	Lower Salado Compacted Clay Column	Salado Halite
43	3.05	Lower Salado Compacted Clay Column	Salado Halite
44	3.05	Lower Salado Compacted Clay Column	Salado Halite
45	3.05	Lower Salado Compacted Clay Column	Salado Halite
46	3.05	Lower Salado Compacted Clay Column	Salado Halite
47	2.32	Lower Salado Compacted Clay Column	Salado Halite
48	1.83	Lower Salado Compacted	Salado Halite





Table C-20. Vertical Layers of the Compacted Salt Column Performance Model

Layer Number	Layer Thickness (m)	Shaft Seal Component	Host Formation Unit
		Clay Column	
49	0.91	Lower Salado Compacted Clay Column	Salado Halite
50	0.46	Lower Salado Compacted Clay Column	Salado Halite
51	0.23	Shaft Station Monolith	Combined MB138 and Anhydrite A/B
52	0.23	Shaft Station Monolith	Combined MB138 and Anhydrite A/B
53	0.46	Shaft Station Monolith	Salado Halite
54	0.61	Shaft Station Monolith	Salado Halite
55	0.61	Shaft Station Monolith	Salado Halite
56	0.91	Shaft Station Monolith	Salado Halite
57	1.52	Shaft Station Monolith	Salado Halite
58	1.52	Shaft Station Monolith	Salado Halite
59 (BOTTOM)	1.52	Shaft Station Monolith	Salado Halite

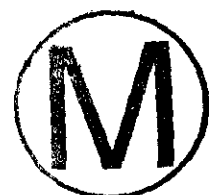
Table C-21. Compacted Salt Column Performance Model Radial Gridding

Column Number	Radius to Outer Grid Column Boundary (m)	Model Component
1	1.22	Shaft
2	1.95	Shaft
3	2.68	Shaft
4	3.05	Shaft
5	3.23	DRZ
6	3.41	DRZ
7	3.78	Host Formation
8	4.51	Host Formation
9	5.24	Host Formation
10	6.46	Host Formation

Table C-21. Compacted Salt Column Performance Model Radial Gridding

Column Number	Radius to Outer Grid Column Boundary (m)	Model Component
11	7.68	Host Formation
12	8.90	Host Formation
13	10.12	Host Formation
14	11.95	Host Formation
15	14.69	Host Formation
16	18.65	Host Formation
17	24.75	Host Formation
18	33.89	Host Formation
19	47.61	Host Formation
20	68.95	Host Formation
21	99.43	Host Formation
22	145.15	Host Formation
23	190.87	Host Formation
24	236.59	Host Formation
25	282.31	Host Formation

Two exceptions to the no-flow top and bottom model boundaries were considered. First, the possibility of brine flow down the shaft from the Rustler Formation was considered by increasing the initial crushed-salt brine saturation as discussed above. Second, gas flow up from the repository was simulated by applying a time varying pressure boundary condition at the base of the shaft. The waste forms in the repository may generate gas (WIPP PA, 1992-1993). Model 2 does not explicitly model the generation of gas in the repository. Rather, it indirectly incorporates repository gas generation by applying a time-varying gas pressure boundary condition at the base of the shaft. Two pressure specifications were considered in the gas flow analysis. In one, the pressure increased to 7 MPa in 100 years and then remained constant for the remaining simulation time (200 years total). In the second, the pressure at the base of the shaft increased steadily for the 200-year simulation period to 14 MPa. These two specifications are representative of results obtained for pressure at the base of the shaft by WIPP PA in the No Migration Variance Petition (NMVP) simulations. The time-varying pressure boundary conditions were chosen to correspond to the quickest pressure increase (i.e., highest gas generation rates) simulated in the NMVP simulations. Figure C-12 shows the pressure condition applied at the base of the shaft in the model runs for these two specifications. Because of limitations in implementing the time-varying boundary condition at the base of the shaft in TOUGH28W, the pressure was "stepped up" to final values in a series of consecutive restarted simulations.



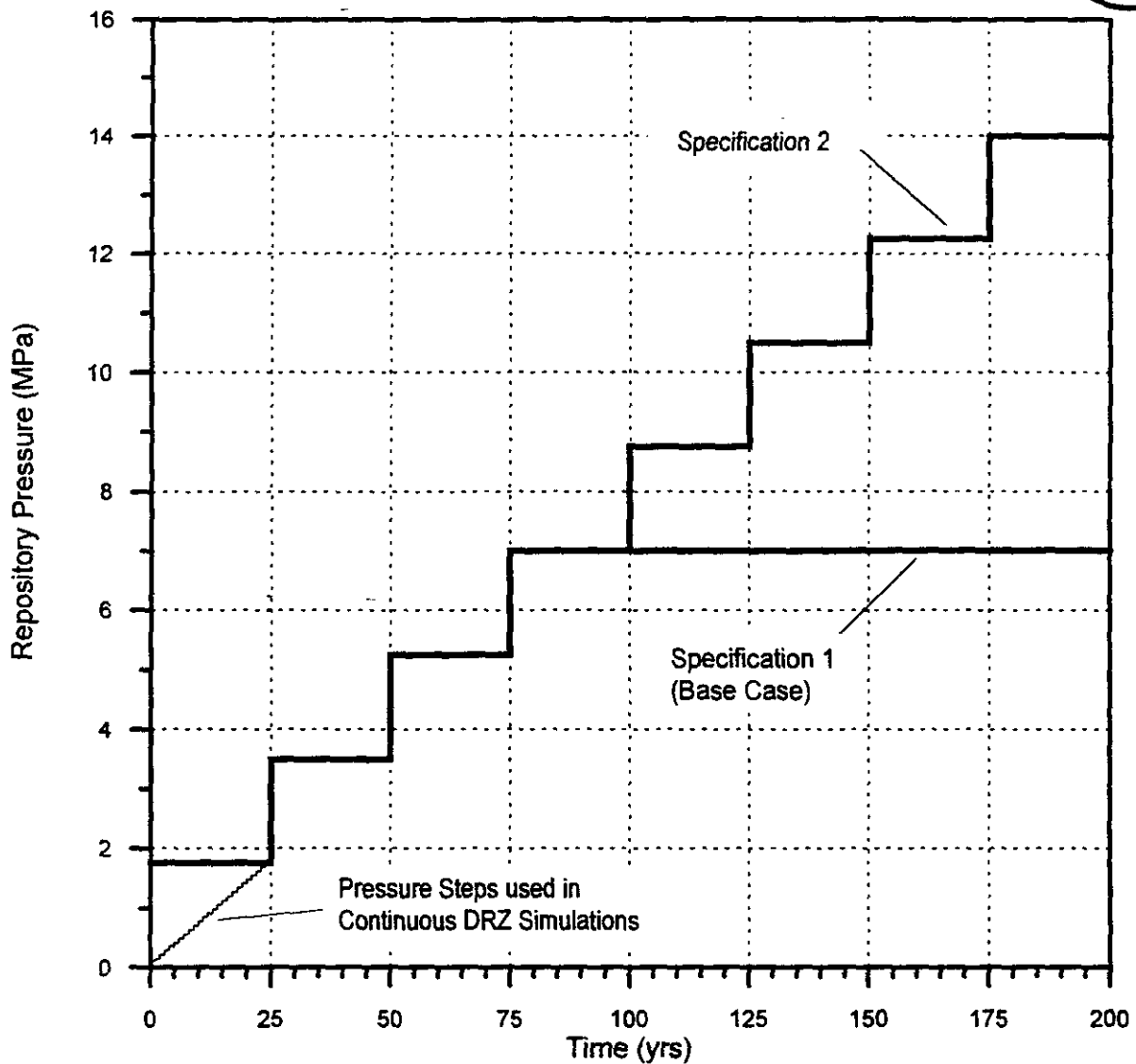


Figure C-12. Two specifications of pressure at the base of the shaft.

For most of the simulations presented here, the pressure was increased in 1.75-MPa steps at 25-year intervals. For continuous DRZ simulations, however, the 1.75 MPa repository pressure at time zero was considered an unrealistic boundary condition to apply to the pre-healed DRZ around the lower concrete component seal. For these cases, the boundary pressure was increased in 1-year steps of 0.07 MPa each. The lighter line between 0 and 25 years in Figure C-12 represents the repository pressure boundary condition used for continuous DRZ simulations.



#### C5.2.4 Model Parameters

Model parameters for the compacted salt column performance model include material properties for shaft seal components, fluid properties, two-phase flow properties, and material properties for Salado halite and anhydrite marker beds. The properties used in this model are discussed in detail in Section C3. Also discussed in Section C3 are the time-varying permeabilities of the DRZ zones surrounding the shaft.

An additional process that must be modeled for the compacted salt column performance model was the consolidation behavior of the crushed salt column. Curves showing salt column fractional density as a function of time at three different depths (430, 515, and 600 m) and three different pore pressures (0, 2, and 4 MPa) are presented in Appendices A and D. The data are replotted in Figure C-13 in terms of the average rate of change in fractional density (on the right axis) versus pressure for the three depths. A relationship has also been developed between crushed salt fractional density and permeability. To account for uncertainty in the permeability versus fractional density relationship, a best fit line through the data, as well as lines through 95th and 5th percentiles, were developed. Using the best fit line between fractional density and permeability, the left axis of Figure C-13 gives the average rate of change for the log of permeability as a function of pressure at the three depths. As shown in the figure, several points were extrapolated from the data to provide model data points up to 10 MPa. The consolidation rate at these higher pressures is not significant to model performance, but the data were required because it was anticipated that salt column pressures could reach these values during late model times.

The “consolidation surface” shown in Figure C-14 was developed by interpolating between the data points shown in Figure C-13. This surface provides the relationship between the rate of change in permeability and depth and pressure within the compacted salt column. In tabular form, this surface is required as input to the compacted salt column performance model. The general shape of this surface shows that the greatest magnitude of the rate of permeability change (i.e., the highest consolidation rate) occurs at the greatest depth (lowest elevation) and lowest pore pressure.

### C5.3 Performance Model Results

Six simulations were run with the compacted salt column performance model, a base-case and five additional runs, to examine the sensitivity of the model to variations in repository pressure, the crushed-salt permeability-fractional density relationship, flow down the shaft from the Rustler Formation, and continuous DRZ with and without waterstops.

Table C-22 summarizes the six simulations and provides information about the combination of parameters used for each. The “Repository Pressure” column in the table refers to the pressure specifications defined in Figure C-12. The “Permeability/Fractional Density Predictor” column in the table refers to either the best fit or the 95th percentile lines through the permeability versus fractional density data. The primary difference between these two permeability specifications is the starting and ending points for salt column permeability. For the best fit line, crushed salt permeability starts at  $2.5 \times 10^{-15} \text{ m}^2$  (90% fractional density) and achieves a minimum possible value of  $6.3 \times 10^{-21} \text{ m}^2$  (100% fractional density). For the “95%” predictor line, crushed salt permeability starts at  $7.9 \times 10^{-13} \text{ m}^2$  and achieves a minimum possible

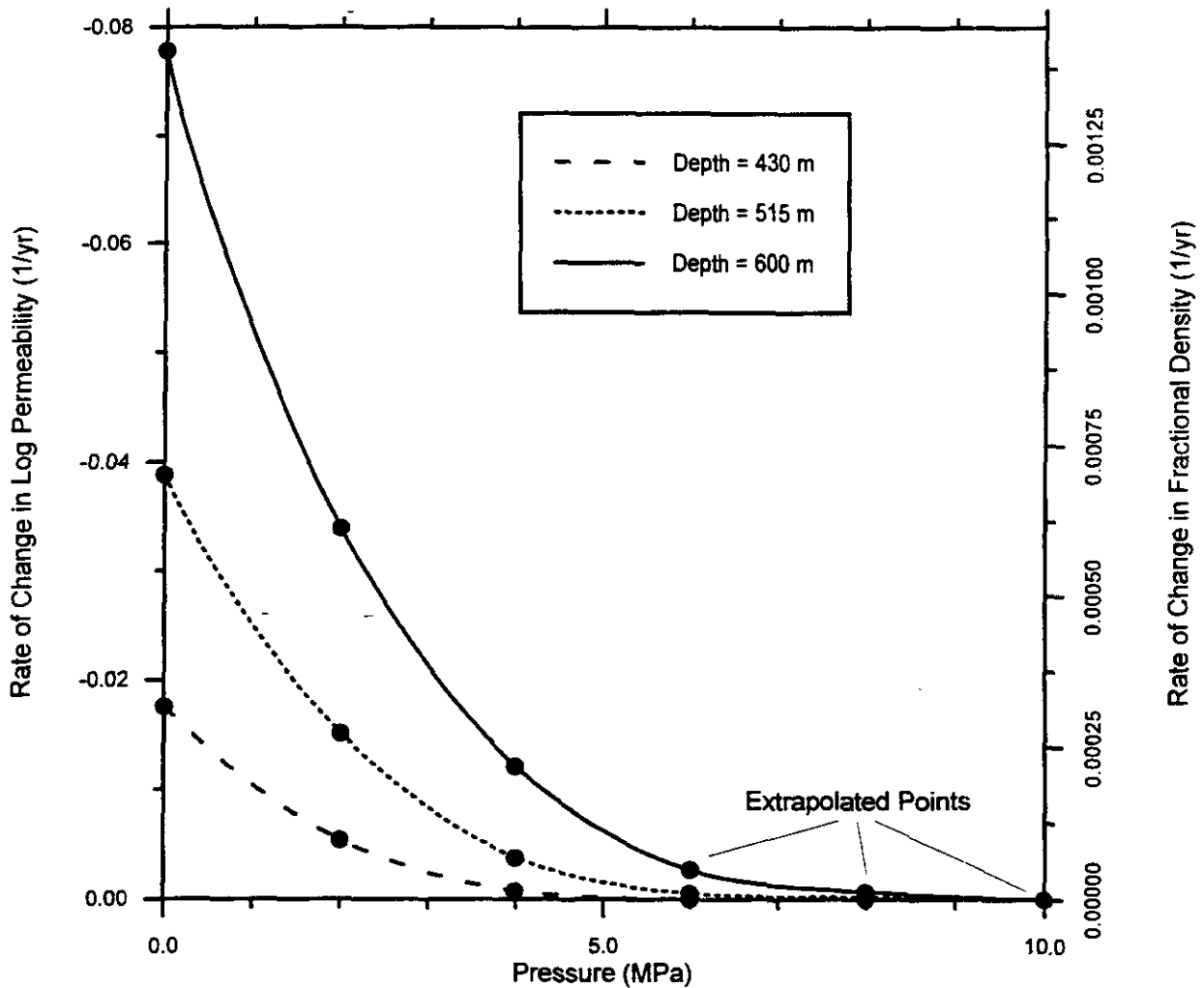


Figure C-13. Rate of change in log permeability (fractional density) with pressure and depth.

value of  $2.0 \times 10^{-18} \text{ m}^2$ . The "Rustler Flow" column in the table indicates the amount by which the salt column initial liquid saturation was increased to account for brine flow down the shaft from the Rustler Formation, predicted by the full-shaft saturated flow model for the case of a continuous DRZ with and without waterstops.

Identical initial pressure conditions were used for each simulation and were established in two steps. First, all grid elements were assigned an initial pressure based on hydrostatic pressure referenced to 12.5 MPa at the elevation of MB139. Next, a conditioning simulation was run in which the shaft was considered to be open to atmospheric pressure for 50 years. Grid-element pressures were captured at the end of this 50-year simulation and used to initialize each of the performance calculations.



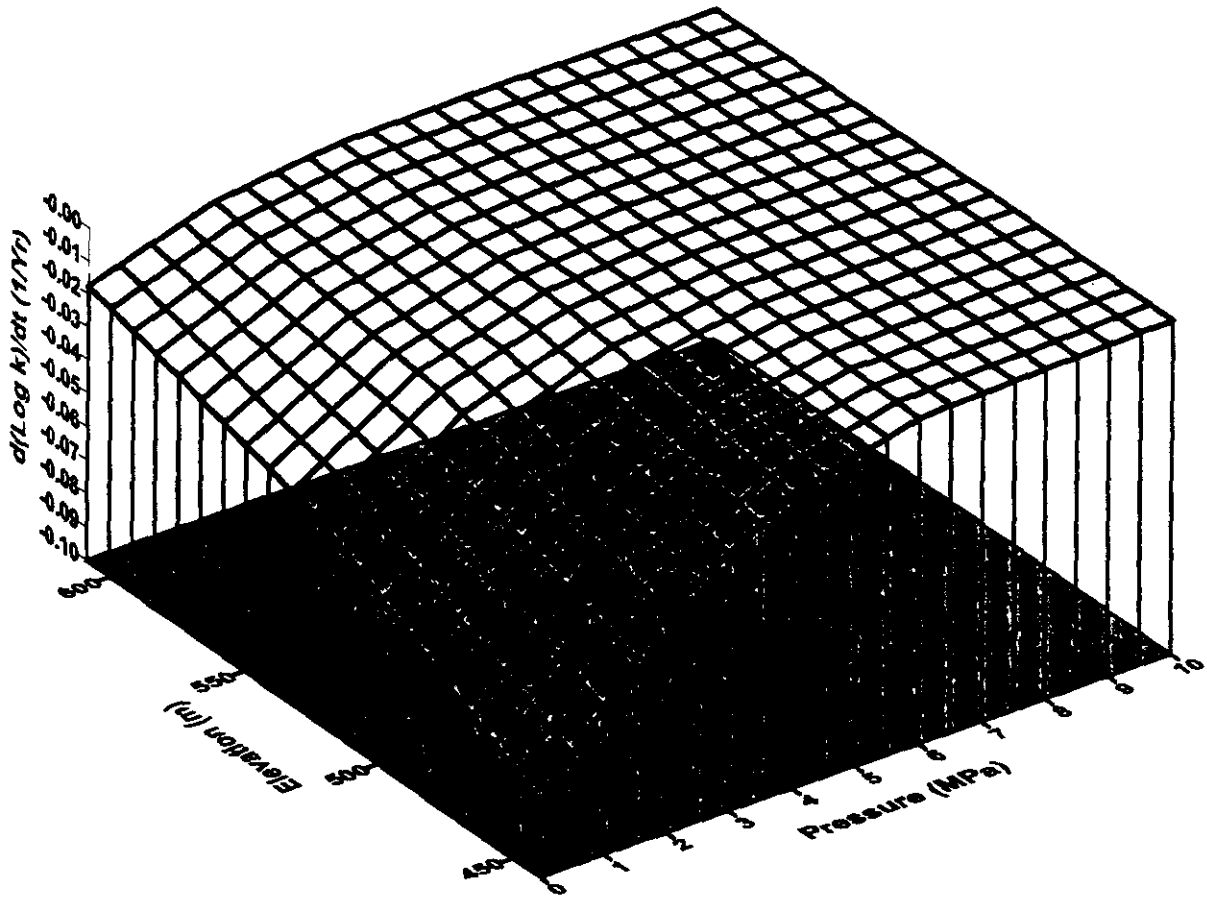


Figure C-14. Reconsolidation surface for the best-fit permeability/fractional density predictor.

Simulation results are presented here in terms of pressure in the compacted salt column, gas flow past the lower concrete component into the compacted salt column, and predicted permeability of the compacted salt column. For the base case of 7 MPa at the repository horizon, Figure C-15 shows calculated pressure in the compacted salt column versus time after seal emplacement at three locations near the top, middle, and bottom of the salt column. The figure shows pressure increased most rapidly at the bottom of the column. Pressure began to increase rapidly at the bottom of the salt column approximately 30 years after seal emplacement. The fact that the pressure in Figure C-15 increased to levels greater than the maximum pressure at the

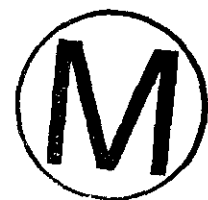




Table C-22. Compacted Salt Column Performance Model Simulations

Run	Repository Pressure*	Permeability/ Fractional Density Predictor	Rustler Flow (m <sup>3</sup> )	Continuous DRZ	Water Stops
1 (Base Case)	7 MPa in 100 Years	Best Fit	0.00	No	Yes
2	7 MPa in 100 Years	95%	0.00	No	Yes
3	14 MPa in 200 Years	Best Fit	0.00	No	Yes
4	14 MPa in 200 Years	95%	0.00	No	Yes
5	7 MPa in 100 Years (Linear First 25 Years)	Best Fit	2.70	Yes	Yes
6	7 MPa in 100 Years (Linear First 25 Years)	Best Fit	17.20	Yes	No

\* Source: NMVP calculations.

base of the shaft (7 MPa) indicates that the far-field pressure boundary was the primary source driving the pressure increase. Figure C-16 shows calculated permeability profiles in the compacted salt column at several points in time following seal emplacement. This figure shows that permeability has decreased to a minimum value of  $6.3 \times 10^{-21} \text{ m}^2$  over a portion of the base of the salt column in 100 years and shows little further reduction of permeability over the period from 100 to 200 years. The figure generally shows lower permeability near the bottom of the salt column where the consolidation rate is higher, and relatively higher permeability near the top of the salt column where the consolidation rate is lower. After 100 years, pressure increases throughout the column have almost completely stopped the consolidation process.

A small region, from elevation 439 m (1440 ft) to about elevation 457 m (1500 ft), at the base of the salt column showed less reconsolidation at times ranging from 50 to 200 years than the region immediately above it due to the pressure influence of the repository. Figure C-16 also shows that for times greater than about 50 years, consolidation in the upper half of the salt column was significantly slowed because of repressurization through the relatively high permeability Union Anhydrite ( $1.0 \times 10^{-18} \text{ m}^2$ ).

The results of Run 2, in terms of pressure and permeability in the compacted salt column, are shown in Figures C-17 and C-18, respectively. Parameter specification for this run was identical to Run 1 except that the 95% permeability-fractional density correlation was used (i.e., the assumed salt column permeability was higher for a given fractional density). These results show that pressurization in the salt column occurred at later times than for the base case. The permeability profiles in Figure C-18 show that, in contrast to the base case, very little crushed salt reconsolidation occurred in the lower half of the salt column after about 75 years. This outcome occurs because the pressure increased throughout the vertical extent of the salt column

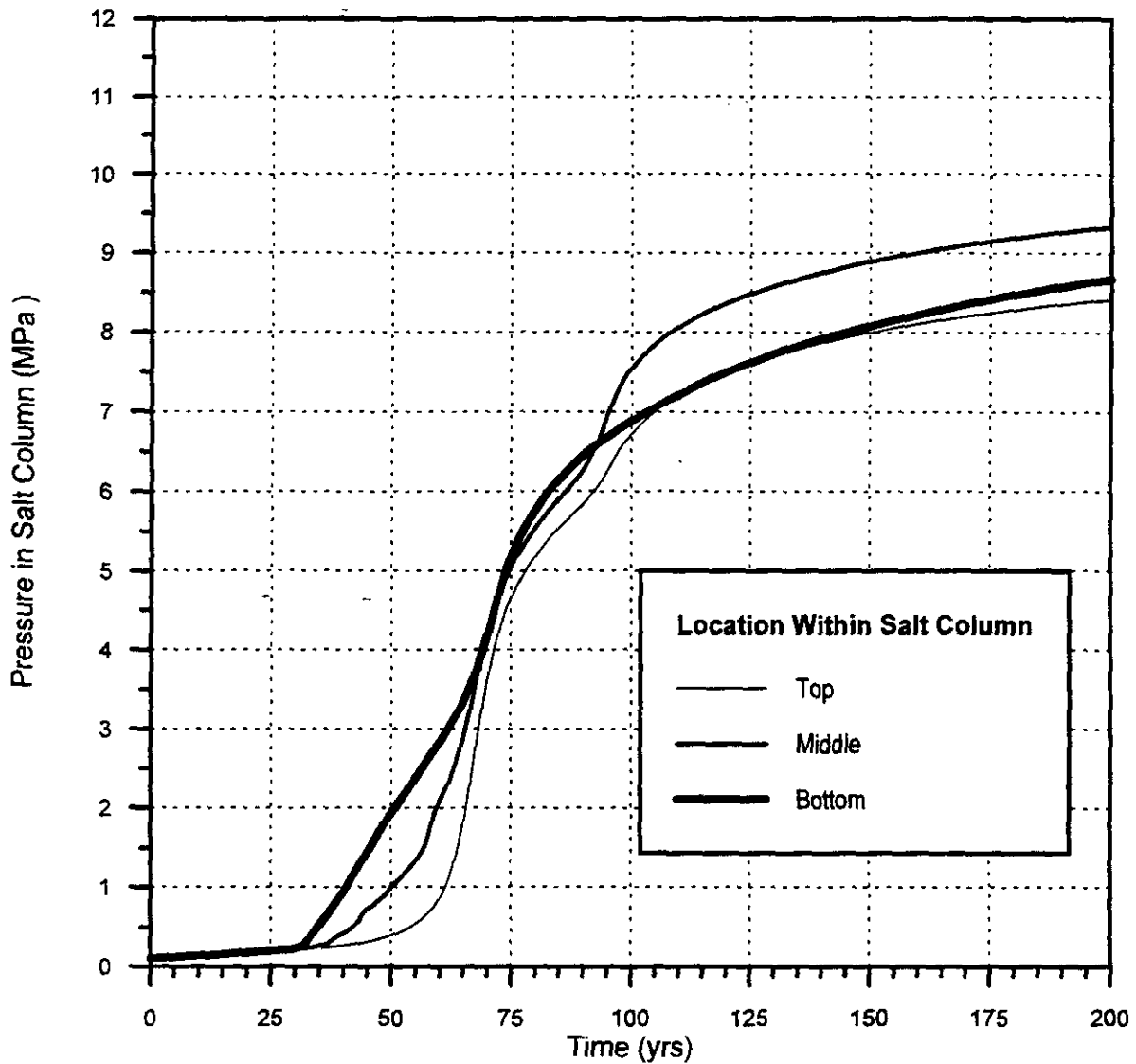


Figure C-15. Calculated pressure versus time after seal emplacement at the top, middle, and bottom of the compacted salt column (base case).

at 75 years in this case, whereas the base case, because of lower permeability of the salt column, retained a region of lower pressure near the base of the column. This can be seen in Figure C-19, which shows pressure contours at 75 years for the base case and for Run 2. In both cases, pressure increases in the salt column due to the influence of the outer pressure boundary through the Union Anhydrite (and to a lesser extent the other interbeds). In the base case, the lower permeability of the reconsolidating crushed salt isolated the area at the base of the column from the Union Anhydrite. For the base case, Figure C-19 shows an area near the base of the column where pressure remained less than 1 MPa at 75 years. In Run 2, the relatively higher permeability of the consolidating crushed salt allowed the pressure to equilibrate along the entire

length of the column, thereby inhibiting consolidation even in the lower half of the column after 75 years.

Runs 3 and 4 in Table C-22 are identical to Runs 1 and 2, respectively, except that the repository pressure was increased from 7 MPa to 14 MPa in the period from 100 to 200 years (see Figure C-12). The results of these two runs in terms of pressure and permeability in the salt column are nearly identical to the results of Runs 1 and 2, and additional plots are not shown. Like those of Runs 1 and 2, these results indicate that, after 100 years, the compacted salt column was sufficiently isolated that salt reconsolidation is not significantly affected by repository-pressure increases.

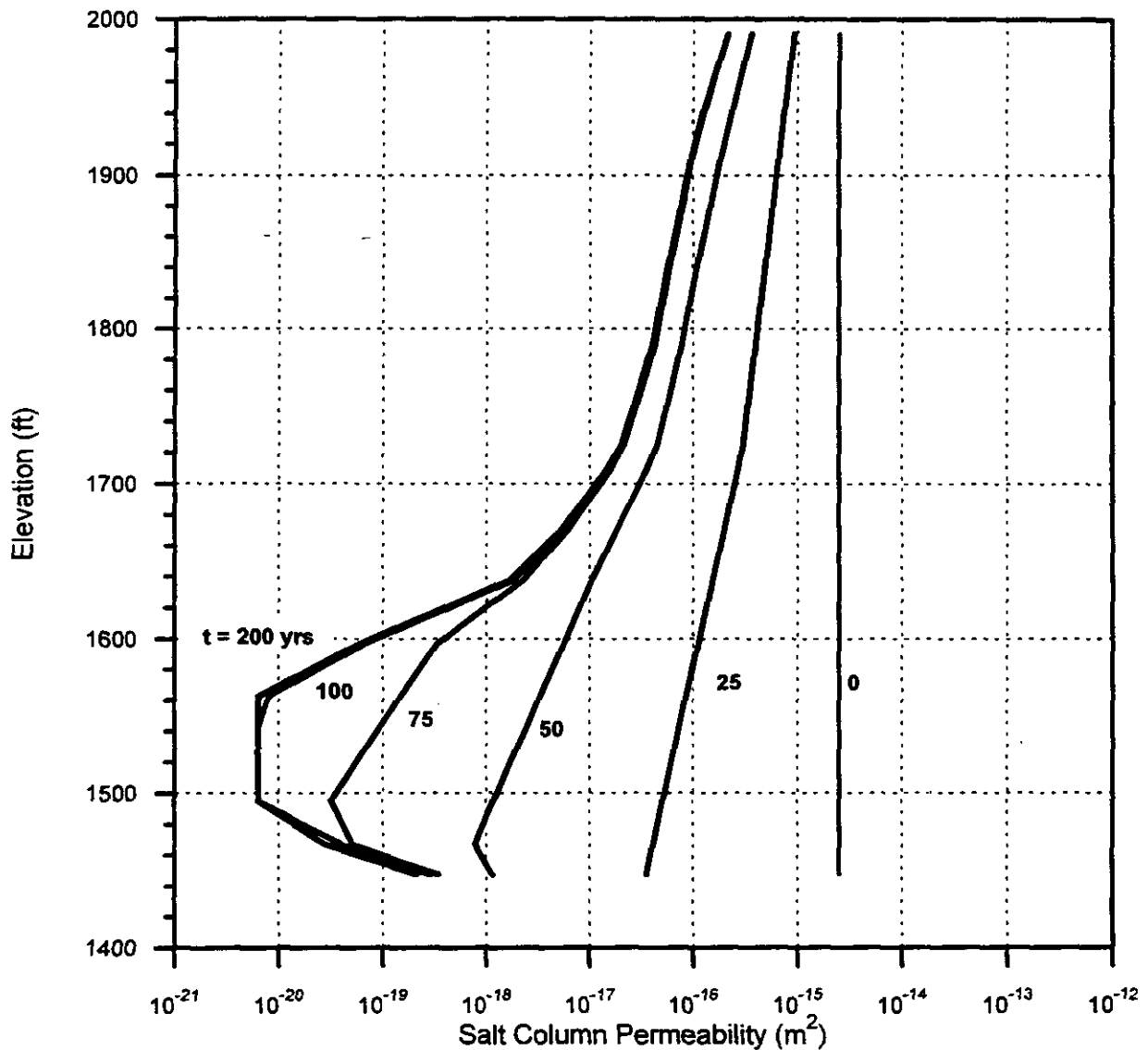


Figure C-16. Calculated salt column permeability versus elevation within the column for several times following seal emplacement (base case).



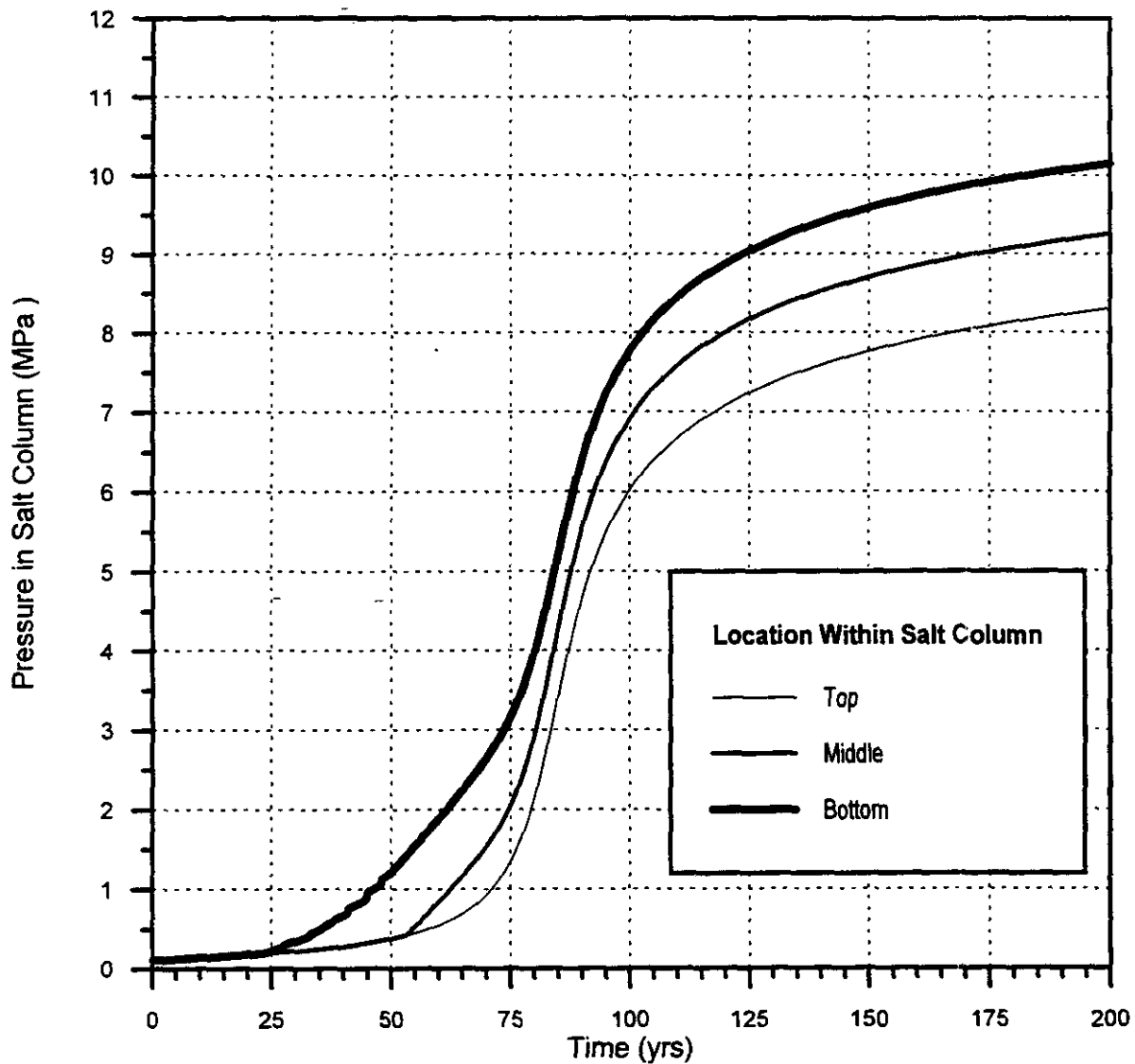


Figure C-17. Calculated pressure versus time after seal emplacement at the top, middle, and bottom of the compacted salt column (Run 2).

Two additional runs (Runs 5 and 6 in Table C-22) were made in which brine flow down the shaft from the Rustler Formation calculated by the full-shaft saturated flow model was included in the initial brine saturation of the compacted salt column. For these two simulations, the permeability of the DRZ adjacent to the shaft at the level of MB134, MB135, MB136, and MB137 was increased to  $2.9 \times 10^{-16} \text{ m}^2$ , thus creating a continuous (prior to healing) DRZ from the gas source at the repository level to the salt column. In the previous simulations, these DRZ units were assumed to be mostly unfractured, with permeability more like the undisturbed host anhydrite of the associated marker beds ( $1.0 \times 10^{-19} \text{ m}^2$ ).

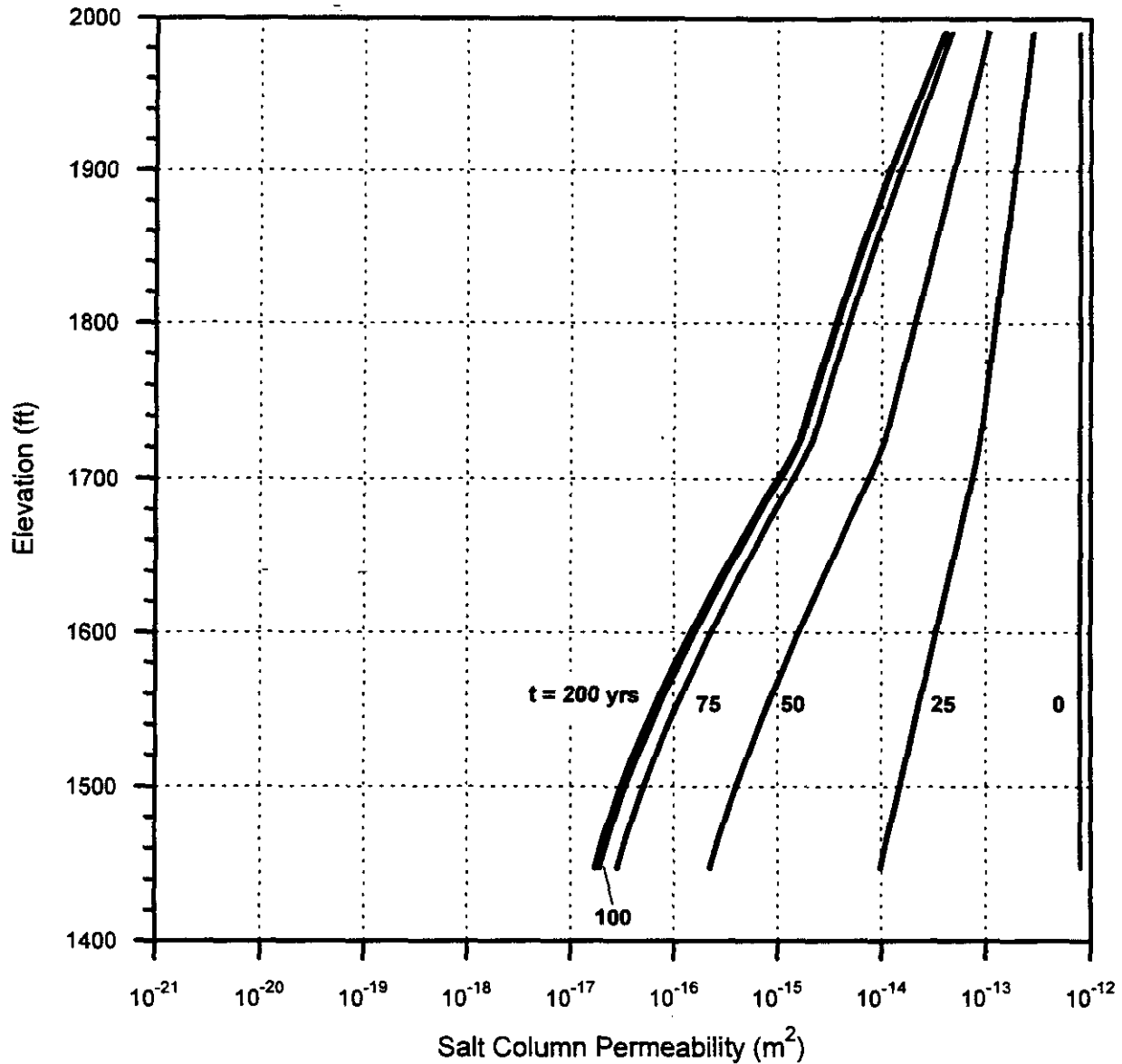


Figure C-18. Calculated salt column permeability versus elevation within the column for several times following seal emplacement (Run 2).

In Run 5 the asphalt waterstops were assumed to be in place as in the previous runs; however, in Run 6 the asphalt waterstops were excluded. The initial brine saturation of the salt column was increased by 2.7 m<sup>3</sup> and 17.2 m<sup>3</sup> for the two runs, respectively, to account for Rustler flow predicted by the full-shaft saturated flow model for these two cases. For the continuous DRZ assumption, with the increased communication between the base of the shaft and the compacted salt column prior to DRZ healing around the rigid concrete components, it was thought that stepping the repository pressure up to 1.75 MPa at time zero would provide unrealistic results. Therefore, for these two runs, the repository boundary pressure was

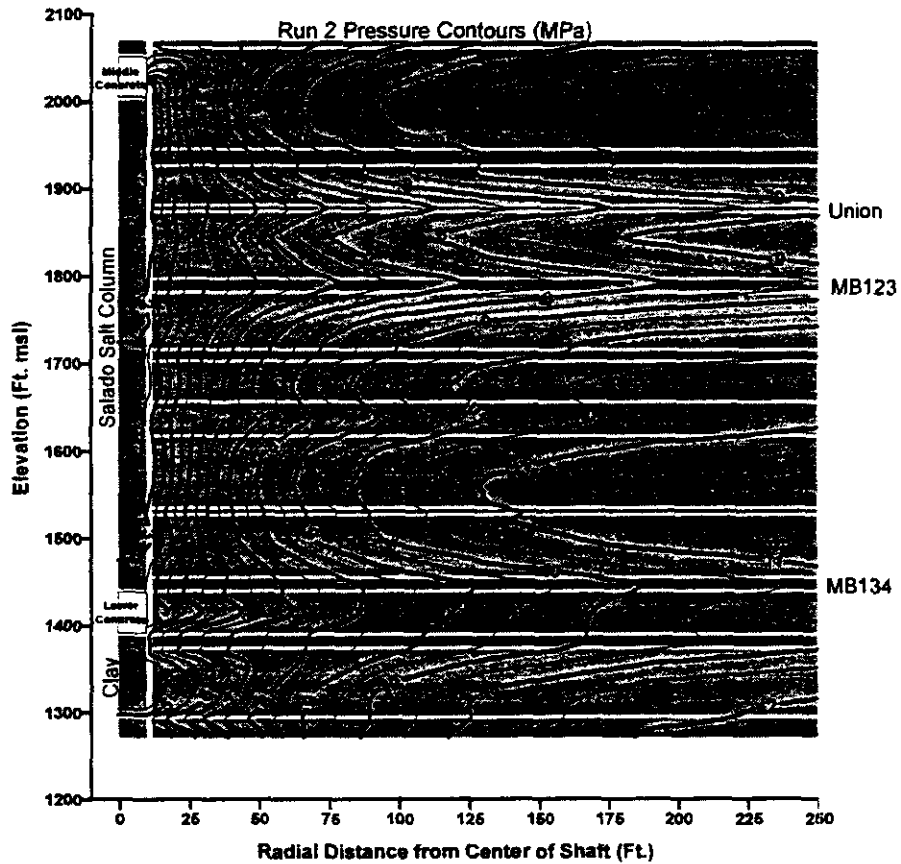
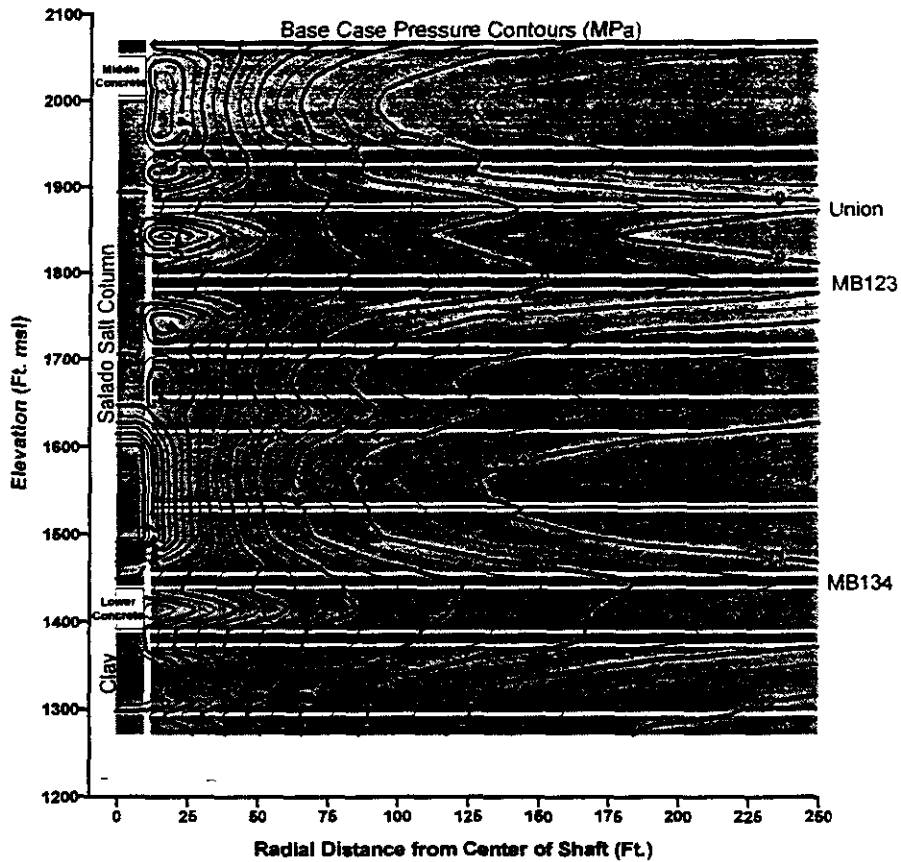


Figure C-19. Pressure contours at 75 years for base case and for 95% permeability/fractional density predictor (Run 2).



increased in 0.07-MPa increments at one-year time intervals (see Figure C-12). This rate of pressure increase is the same for all simulations; however, it is applied in smaller time increments in Runs 5 and 6.

The pressure and permeability results of Run 5 are nearly identical to the results of the base case (Run 1) shown in Figures C-15 and C-16, indicating no sensitivity to the inclusion of a DRZ adjacent to MB134 through MB137. The results of Run 6 do, however, show some sensitivity to the absence of the asphalt waterstops. Figure C-20 shows pressure versus time at the top, middle, and bottom of the salt column for the base case and for Run 6. This figure shows that pressure rose faster than for the base case at early times before the DRZ had fully healed around the lower concrete seal at 25 years. As a result of the faster pressure increase in the salt column, the calculated permeability profiles shown in Figure C-21 for this run show less crushed-salt reconsolidation at 100 years than in the base case shown in Figure C-16. Figure C-21 shows that, without concrete-asphalt waterstops, permeability at the bottom of the salt column for the case does not reach the minimum value of  $6.3 \times 10^{-21} \text{ m}^2$ .

Figure C-22 shows cumulative gas flow up the shaft from the repository past the lower concrete seal for each run. The right axis in the figure gives cumulative mass of gas flow in kg and the left axis translates this mass to a cumulative volume of flow in  $\text{m}^3$  at standard conditions ( $20^\circ\text{C}$  and atmospheric pressure). This figure shows that cumulative gas flow up from the repository was less than  $100 \text{ m}^3$  for all runs, except for Run 6 in which the concrete-asphalt waterstops were omitted. Run 6 predicted that approximately  $600 \text{ m}^3$  of gas reached the salt column in the first 25 years.

The lower Salado compacted clay column provides an effective barrier in shaft cross-section because of its low permeability and its relatively high brine saturation, thus forcing most of the gas to flow through the DRZ. The compacted clay column was initialized at an initial brine saturation of nearly 80%. For all simulations performed, it resaturated to near 100% at top and bottom over the 200-year simulation time.

## **C6.0 FLOW UP FROM THE SALADO (MODEL 3)**

### **C6.1 Statement of Problem**

This calculation examined the potential for brine flow and quantity of brine flow that may be expected to migrate upward through the shaft seal system in response to the ambient pressure conditions that will be present several hundred years after closure. Pressures measured in the Salado at the repository horizon are significantly over-pressured with respect to hydrostatic conditions and to the Rustler (see Table C-2). Because the Salado is very impermeable, any natural component of vertical flow from the Salado upward must be very low. However, with the connection of the Salado and the Rustler Formations through the shaft seal system, the potential for upward flow exists. The performance measure (result) for this model is the steady-state brine flow rate. The performance measure will be provided for the Rustler/Salado contact, the top of the compacted salt column, and the top of combined Unit 8 (composed of MB131, Zone J, MB132, and MB133).

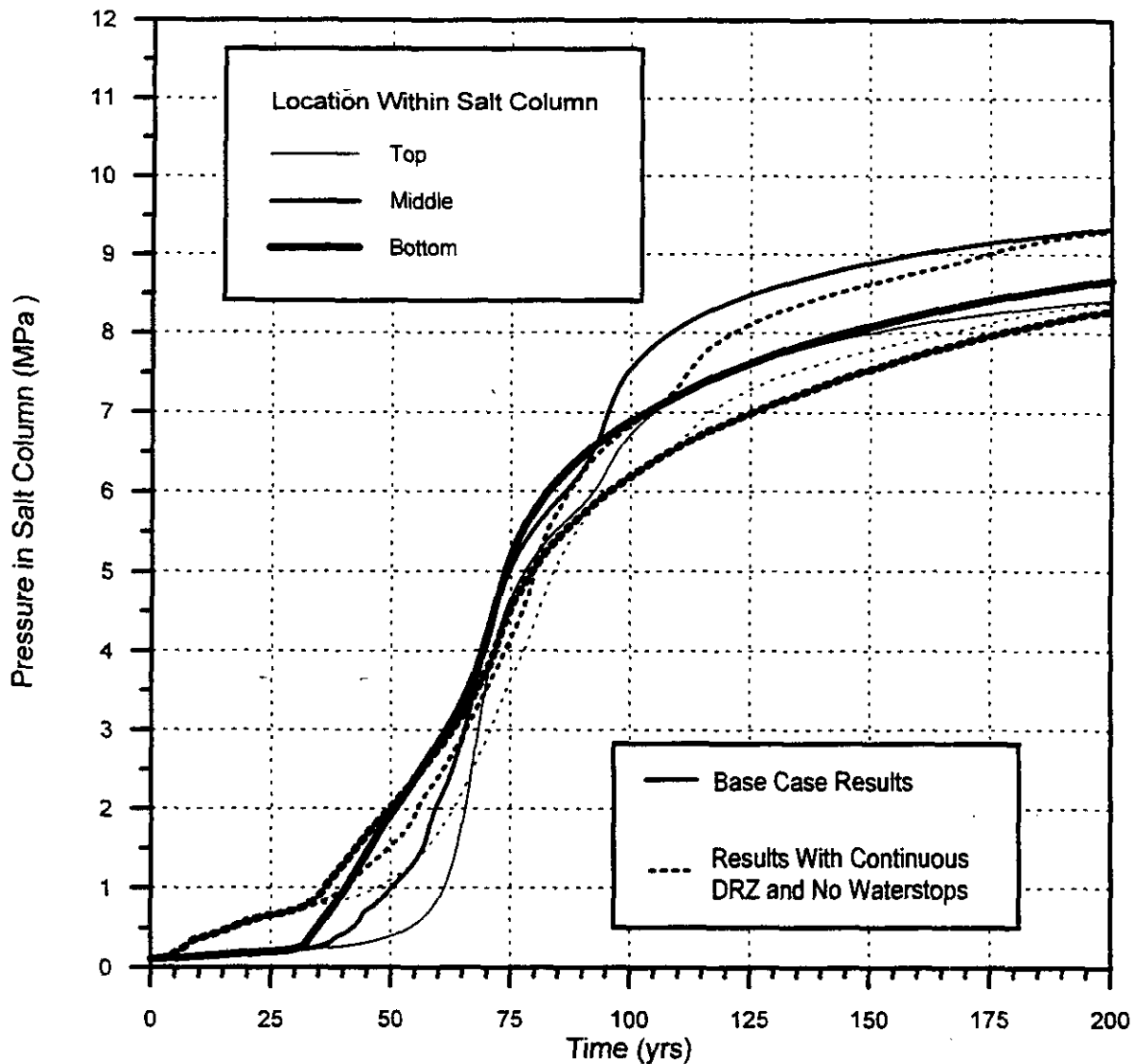


Figure C-20. Comparison of calculated pressure results for base case and continuous DRZ with no waterstops (Run 6).

## C6.2 Performance Model Description

### C6.2.1 Conceptual Model and Assumptions

The model grid and simulation code (SWIFT II) used in this model are identical to those used in Model 1. The primary difference in the conceptual model between Model 1 and Model 3 is the time frame over which this calculation is considered relevant. Model 1 predicted brine flow down the shaft. The Model 1 calculation is considered an early-time calculation before far-field pressures gradients reestablish in the vicinity of the shaft. The Model 1 calculation runs from shaft closure forward to 400 years post-closure. Model 3 assumed that equilibrium pressure gradients have reestablished in the vicinity of the shaft and DRZ healing has taken place within the Salado halite.



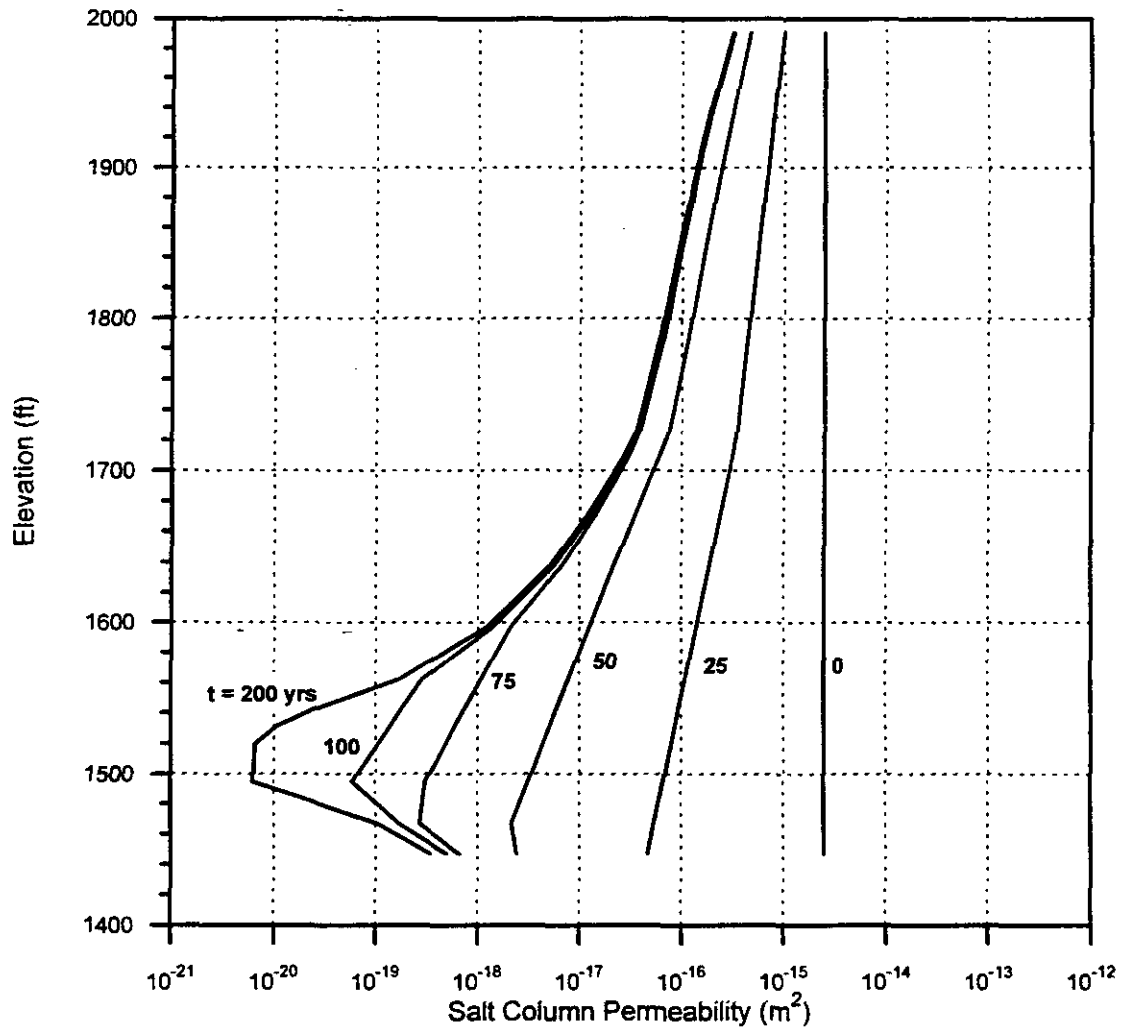


Figure C-21. Calculated salt column permeability versus elevation within the column for several times following seal emplacement (Run 6: Rustler flow included, continuous DRZ, no waterstops).

In Section C2, the primary assumptions common to all numerical calculations in this appendix are listed. In addition to those listed in Section C2, the following list summarizes the primary assumptions specific to Model 3:

- The calculation assumed brine-saturated flow conditions.
- The model is initialized at nonhydrostatic conditions based on undisturbed heads in the Rustler Formation and the maximum estimated formation pressure measured in the Salado Formation (see Table C-2).
- Seal system and DRZ permeabilities are representative of times greater than or equal to 400 years after closure.

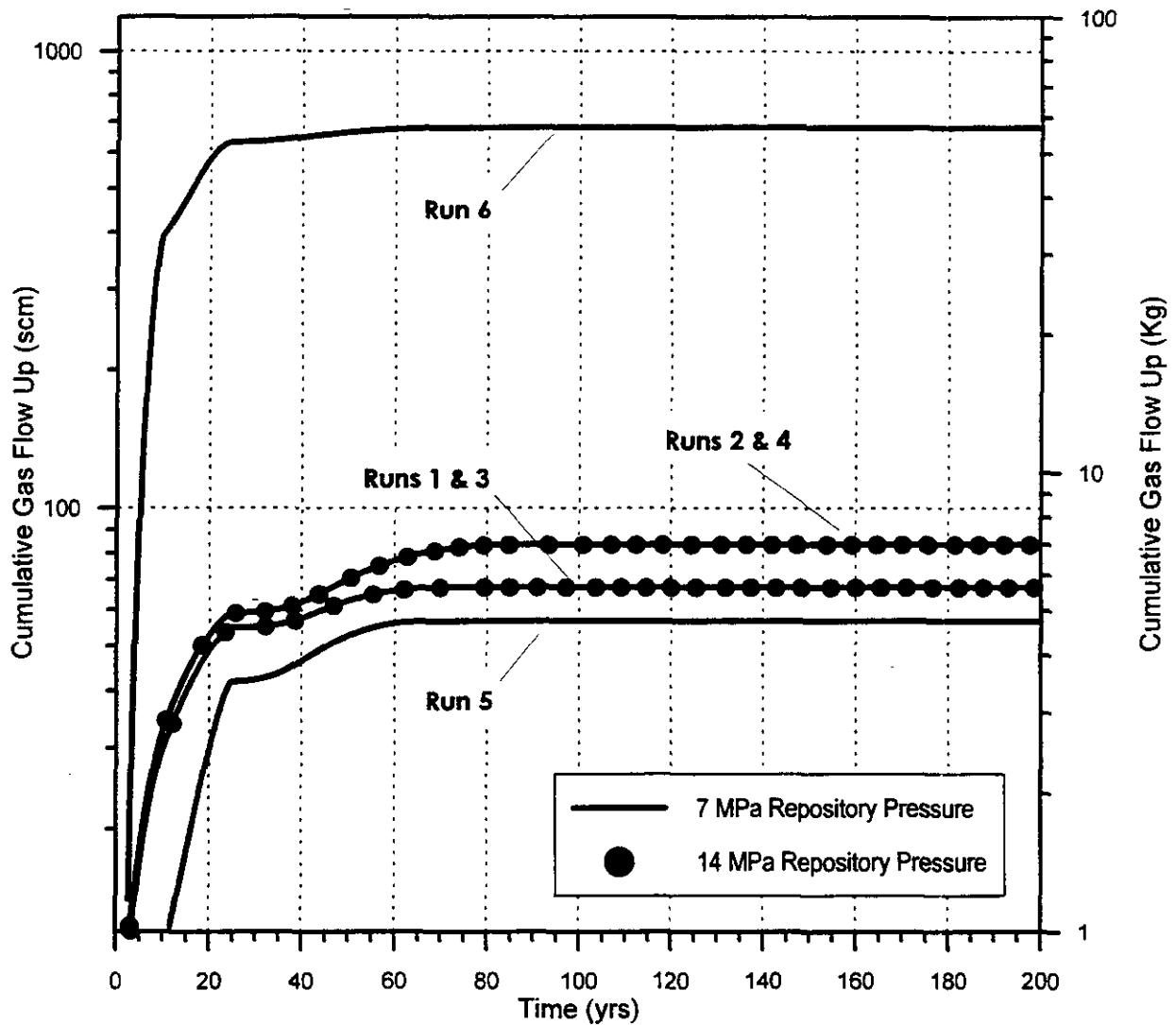


Figure C-22. Cumulative gas flow from the repository to the compacted salt column.

### C6.2.2 Numerical Method

The numerical code used in Model 3 is SWIFT II. This code was also used in Model 1; see Section C4.2.2 for a complete description.

### C6.2.3 Model Geometry and Boundary Conditions

The model geometry and grid are the same as that used in Model 1; see Section C4.2.3 for a complete description. However, the initial conditions and boundary conditions differ from those of Model 1. For Model 3, the shaft is completely sealed, and the DRZ and the compacted salt column permeabilities are no longer transient and have achieved their lowest values. This permeability field was held constant in Model 3.





The lateral boundary and initial grid-block pressures were initialized at nonhydrostatic conditions consistent with the undisturbed heads reported for the Magenta, the Culebra, the Rustler/Salado contact, and MB139 (see Table C-2). No-flow boundary conditions were imposed at the top and bottom of the model. Infinite aquifer boundary conditions were set at the outer edge of the modeled region. The model components for the simulation are concrete, asphalt, compacted clay, crushed salt, shaft liner, DRZ, and undisturbed formation.

#### C6.2.4 Model Parameters

Best case model parameters as specified for Model 1 for the host-rock and seal system have been used. Table C-23 summarizes the three simulations performed in Model 3, highlighting the principal differences among them. This suite of runs is similar to the runs simulated in Model 1.

The base-case simulation (Run 1) assumed that the anhydrites in the Rustler Formation, and anhydrites greater than 3 m thick in the Salado Formation, have no DRZ (based on mechanical modeling results presented in Appendix D). This condition results in a discontinuous DRZ, which is discontinuous initially and remains so throughout the simulations. The second simulation (Run 2) assumes that Rustler members and Salado anhydrites are damaged, and allows healing to occur only in the Salado halite. Runs 1 and 2 include waterstops. The third simulation (Run 3) is a sensitivity simulation to examine the impact of the asphalt waterstops. It is the same as Run 2 except that the concrete-asphalt waterstops were not incorporated into the model. Figure C-23 depicts the permeabilities used in these three simulations.

Table C-23. Performance Model 3 Simulations

Run	Rustler and Anhydrite DRZ	Waterstops
1 (Base-Case)	No	Yes
2	Yes	Yes
3	Yes	No

#### C6.3 Performance Model Results

Results are presented in terms of brine flow rates ( $m^3/s$ ). Because the vertical gradient is directed upward, the flow rates reported are also upward. Table C-24 provides the steady-state upward flow rates measured at the Rustler/Salado contact, the top of the compacted salt column, and the top of combined Unit 8 of the model. The difference between the results of Runs 1 and 2 derives from the increased DRZ permeabilities assumed for the anhydrite units. The lack of a difference between the results of Runs 2 and 3 denotes the negligible effect of the waterstops on long-term saturated flow.

The waterstops were included in the seal system design as an immediate seal for the DRZ. Therefore, their inclusion in Runs 1 and 2 was not really appropriate. However, based on the results from Run 3, it can be concluded that their presence in Runs 1 and 2 did not affect the predicted performance measure of upward steady-state flow rate for these simulations.

C-77

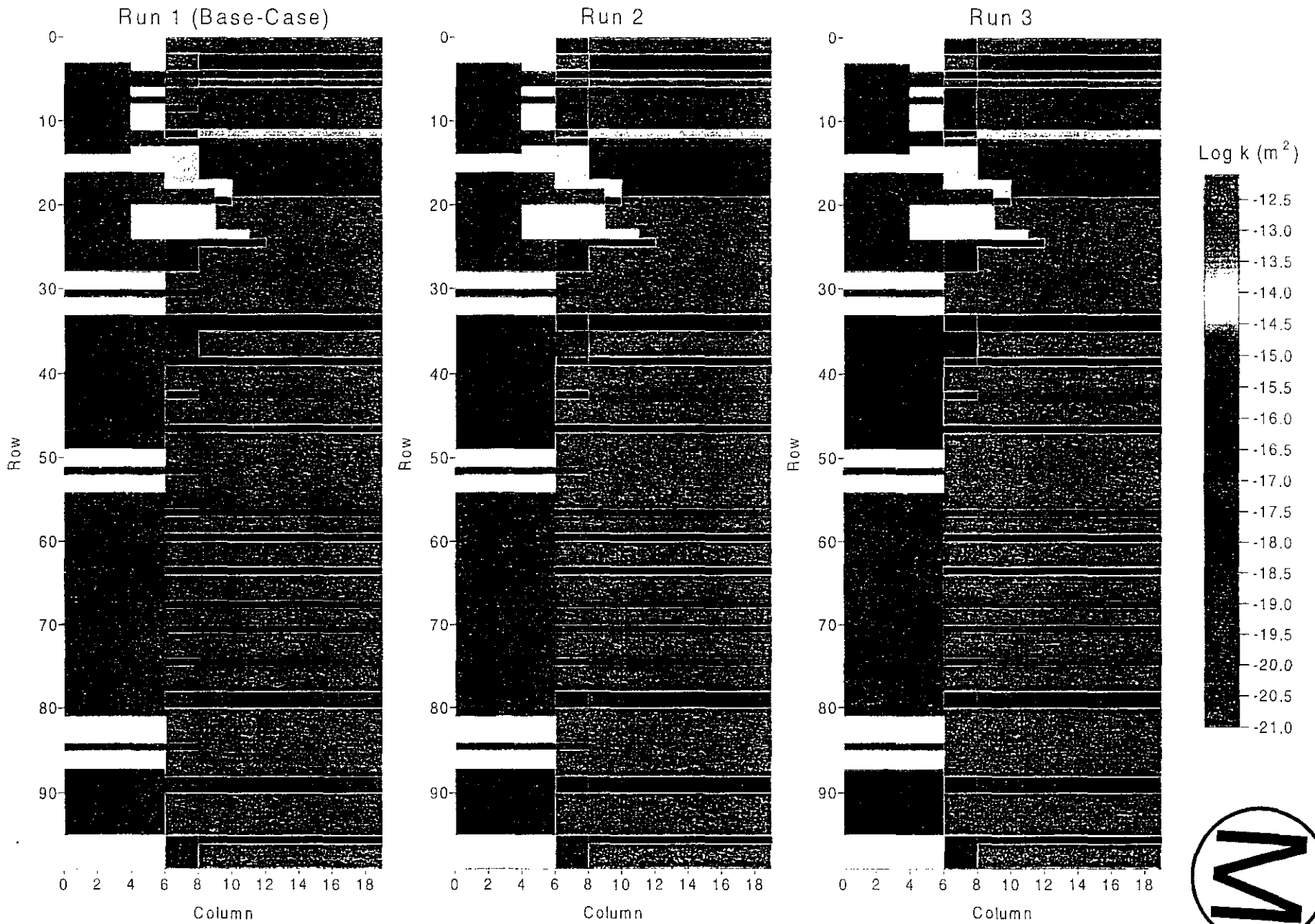


Figure C-23. Permeability fields for Runs 1 through 3 ( $t > 400$  years).

Table C-24. Comparison of Flow Rates Up the Shaft/DRZ from Simulations that Incorporate the Measured Pressure Conditions

Run	Combined Unit 8	Top of Compacted Salt Column	Rustler/Salado Contact
	Flow Rate up the Shaft and DRZ (m <sup>3</sup> /yr)		
1 (base-case)	4.76×10 <sup>-5</sup>	1.68×10 <sup>-4</sup>	8.27×10 <sup>-4</sup>
2	4.76×10 <sup>-5</sup>	1.71×10 <sup>-4</sup>	9.68×10 <sup>-4</sup>
3	4.76×10 <sup>-5</sup>	1.71×10 <sup>-4</sup>	9.68×10 <sup>-4</sup>

## C7. INTRA-RUSTLER FLOW (MODEL 4)

### C7.1 Statement of Problem

The shaft seal system is designed to limit migration of fluids within the sealed shaft. The natural heads within the Rustler Formation are nonhydrostatic indicating the potential for vertical flow (Beauheim, 1989). This calculation examined the potential for, and quantity of brine flow, which, after closure, could be expected to migrate between the Magenta and the Culebra, the two primary water-bearing members of the Rustler Formation.

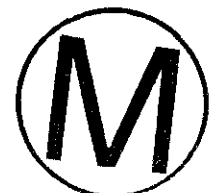
### C7.2 Performance Model Description

The previous models have used sophisticated numerical flow models. This performance model employed simple analytical relationships. The calculation assumptions yielded a relatively simple conceptual model and estimates of intra-Rustler flow rates. The conceptual model, relevant assumptions, and the analysis approach are discussed below.

#### C7.2.1 Conceptual Model and Assumptions

Non-hydrostatic conditions exist within the Rustler Formation based on estimated undisturbed or measured disturbed head differences between the various members of the Rustler Formation (see Table C-1). Relatively low undisturbed permeabilities of the mudstone and anhydrite units separating the Culebra and the Magenta naturally limit crossflow. However, the construction and subsequent closure of the shaft provide a potential permeable vertical conduit connecting water bearing units. In this calculation, the hydraulic conductance of the shaft seal system was used to estimate flow rates between the Magenta and Culebra under various assumptions. Figure C-24 schematically shows the conceptual model for calculating intra-Rustler flow rates. From Figure C-24 one can see that flow was considered through the seal and through the DRZ consistent with Models 1 through 3. The primary assumptions for this analysis are listed below:

- Saturated flow was assumed under isothermal and constant fluid-density conditions.
- Flow-rates were calculated using the steady-state version of Darcy's Law for saturated flow.



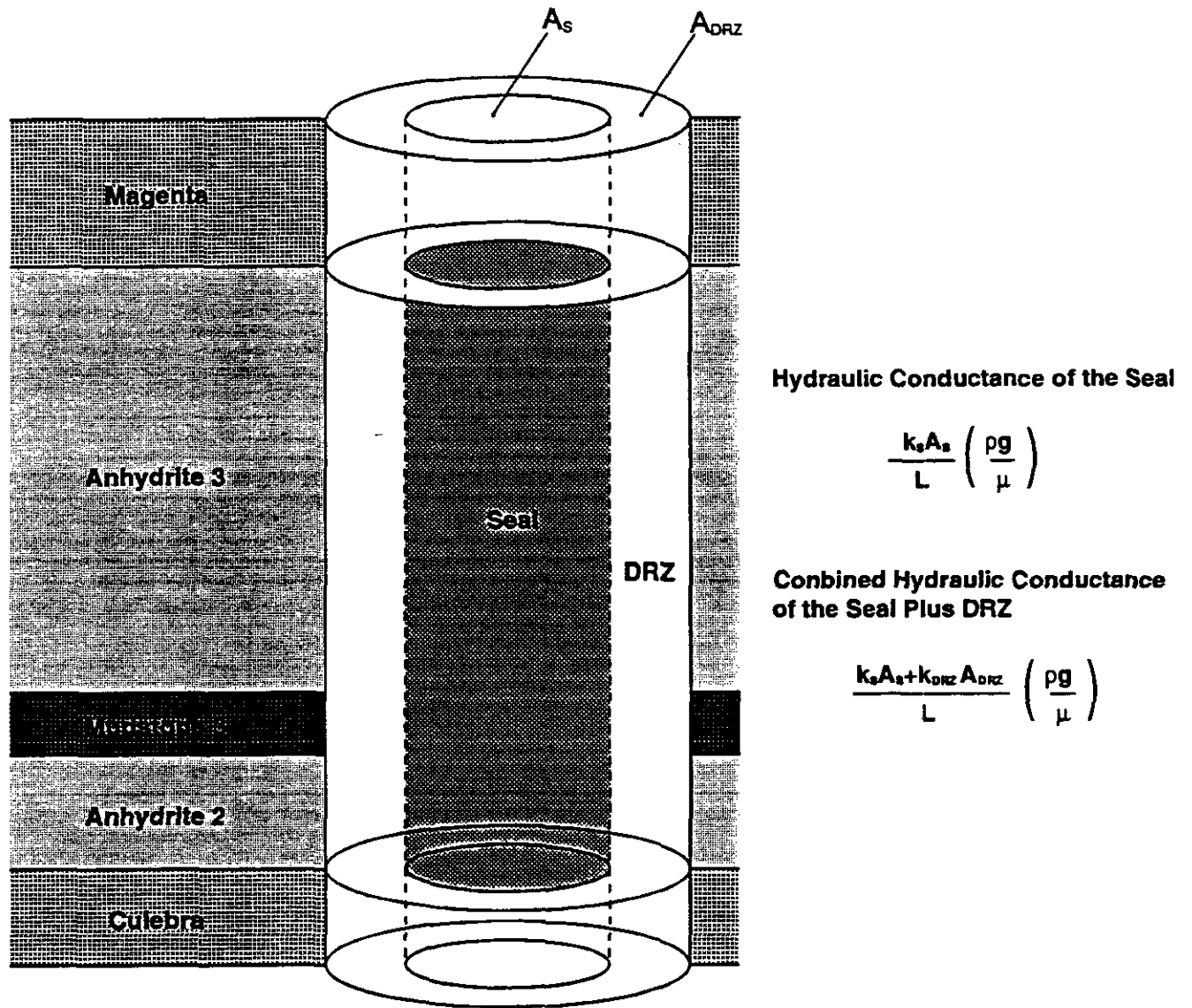


Figure C-24. Intra-Rustler flow conceptual model.





- Resistance to flow was assumed to be only a function of the seal material and DRZ permeabilities. The resistance provided by the geologic members is assumed to be much larger, and the resulting natural vertical crossflow was not considered.
- The driving force (head difference) between water-bearing strata was assumed to be constant and unchanged as a result of flow between units.

### C7.2.2 Analytical Approach

A simple analytical model was used to estimate the potential for brine migration between Rustler members. When two hydraulic units are hydraulically connected and at different heads, flow will occur from the unit with the highest head to the unit with the lowest head. Flow is governed by Darcy's Law, which under the assumptions of single-phase steady-state fluid flow through a porous medium can be expressed as

$$Q = -kA \frac{\Delta h}{\Delta l} \frac{\rho g}{\mu} \quad (\text{C-4})$$

where

- $Q$  = volumetric flow rate with units of ( $\text{m}^3$ )
- $k$  = the intrinsic permeability of the porous medium ( $\text{m}^2$ )
- $\rho$  = the fluid density ( $\text{kg}/\text{m}^3$ )
- $g$  = the acceleration of gravity ( $\text{m}/\text{s}^2$ )
- $\mu$  = the fluid viscosity ( $\text{Pa} \cdot \text{s}$ )
- $\Delta h$  = the head difference between these two units (m)
- $\Delta l$  = the separation of the Culebra and the Magenta (m)
- $A$  = the seal plus DRZ cross-sectional area normal to the flow direction ( $\text{m}^2$ ).

Equation C-4 above can be simplified by using the concept of the hydraulic conductance of a porous medium. The hydraulic conductance of a porous medium is composed of area, length, intrinsic permeability, and the fluid viscosity and density. The hydraulic conductance is the inverse of the hydraulic resistance.

The hydraulic conductance defined in terms of intrinsic permeability can be expressed as

$$C = \frac{kA}{\Delta l} \frac{\rho g}{\mu} \quad (\text{C-5})$$

where  $C$  is the hydraulic conductance ( $\text{m}^2/\text{s}$ ).

In this case Darcy's Law above can be expressed as

$$Q = C \Delta h \quad (\text{C-6})$$

where  $C$  is the effective hydraulic conductance of the seal and DRZ materials separating the Culebra and the Magenta.

Figure C-24 shows the conceptual model for intra-Rustler flow. An effective hydraulic conductance of the seal and DRZ system between the Magenta and the Culebra members can be calculated by analogy to electrical circuit theory. The effective hydraulic conductance is composed of the properties of the DRZ and the seal combined. The seal and DRZ act in parallel, and therefore the hydraulic conductance of these two regions can be directly added to get their combined conductance:

$$C = \frac{k_s A_s + k_{DRZ} A_{DRZ}}{\Delta l} \frac{\rho g}{\mu} \quad (C-7)$$

Because the DRZ permeability is a function of rock type, the effective seal plus DRZ hydraulic conductance must also be combined vertically in series between the Magenta and the Culebra. Using the hydraulic conductance of the seal system and the DRZ, a volumetric flow rate can be estimated from the potential head difference.

To put the calculated volumetric flow rates into perspective, the flow rate can be used to calculate the width of the hydraulic disturbance which is created in the water-bearing unit receiving the interflow. Figure C-25 depicts the case of a point injection into a linear flow field. The injected fluid displaces a certain volume of the receiving aquifer fluid and this volume can be expressed as the maximum plume width (measured in plan view, Figure C-25). Within this maximum plume width, the fluid in the receiving aquifer is composed entirely of injected fluid. Outside of this width, the fluid is composed of the resident aquifer fluid. The equation describing the half plume width is:

$$W = \frac{Q_w}{2u_o b} \quad (C-8)$$

where

$Q_w$  = the intra-Rustler fluid flow rate

$u_o$  = the Darcy velocity of the stratigraphic unit being injected into

$b$  = the thickness of the stratigraphic unit being injected into.

### C7.2.3 Model Parameters

Model parameters having to do with the seal system and the Rustler rocks have been previously defined (Section C3). Using the base case seal and DRZ conceptualization and parameters, the flow rate between the Magenta and the Culebra was calculated considering a range of head differences. The calculated flow rates are used to estimate plume half widths in both the Culebra or the Magenta. The flow rate between the Magenta and the Culebra was also calculated considering a continuous DRZ of variable normalized radius and considering a constant head difference of similar magnitude to that which is currently estimated for undisturbed conditions (see Table C-2).



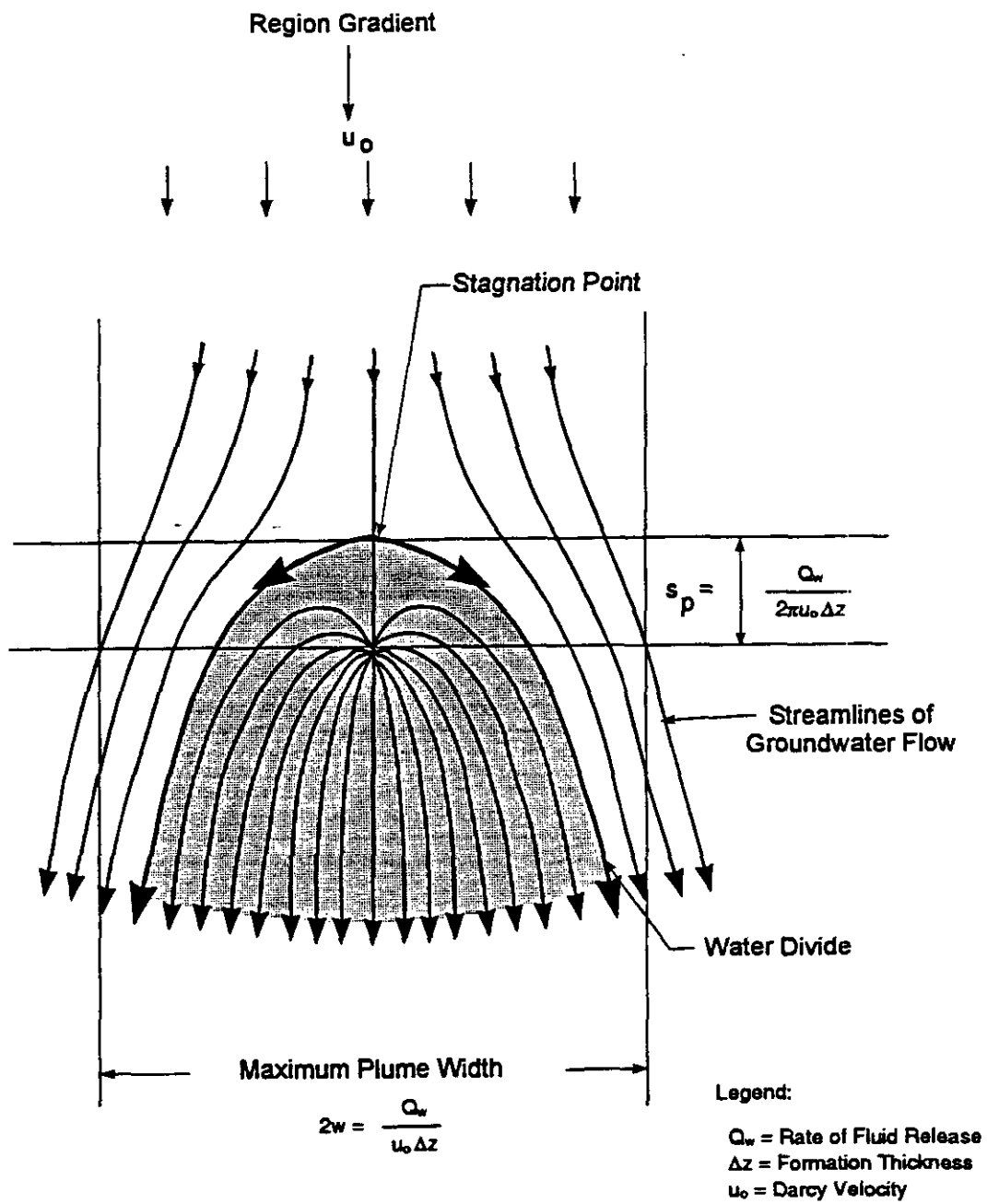
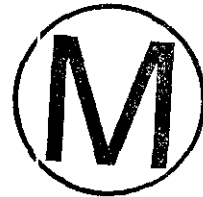


Figure C-25. Effect of an injection well on a unidirectional flow field.

The only parameters unique to Model 4 are the Darcy velocities in the Magenta and the Culebra. These velocities were calculated assuming steady-state Darcy flow and using the minimum regional hydraulic gradient for the Culebra and a regional hydraulic gradient for the Magenta reported by Lambert (1996). The Culebra Darcy velocity was chosen to predict the largest plume half width for a given flow rate (see Equation C-8 above). Table C-25 lists the gradients and Darcy velocities calculated from them using the Culebra and Magenta hydraulic conductivities reported in Section C3.

Table C-25. Regional Darcy Velocities for Culebra and Magenta Members of the Rustler Formation

Rustler Member	Hydraulic Gradient <sup>(1)</sup>	Darcy Velocity (m/s)
Magenta	0.003788	$3.788 \times 10^{-11}$
Culebra	0.001894	$2.652 \times 10^{-10}$

(1) After Lambert, 1996.

### C7.3 Performance Model Results

Table C-2 shows that the approximate undisturbed head difference between the Magenta and the Culebra is 33.2 m (109 ft). Presently, this head difference would direct flow from the Magenta to the Culebra. However, the true head difference is uncertain, especially temporally. Using the base case conceptualization for the DRZ, the flow-rate between the Magenta and the Culebra was calculated for head differences ranging from 3.1 to 121.9 m (10 to 400 ft). Figure C-26 plots the resulting flow rates, which range from 0.002 to 0.096 m<sup>3</sup>/yr. Figure C-27 plots the resulting plume-half width assuming flow was directed into either the Magenta or the Culebra. As can be seen in Figure C-27, the plume half width did not extend past one shaft radius for head differences less than approximately 76 m (250 ft).

The base-case conceptualization assumed that no anhydrite DRZ exists in the Rustler. The next calculation examined the sensitivity of interflow to a continuous DRZ (in both anhydrite and mudstone) for the estimated undisturbed head difference between the Magenta and Culebra.

Figure C-28 plots the flow rate between the Magenta and the Culebra assuming a head difference of 33.5 m (110 ft) and assuming the DRZ is continuous and has a normalized radius of extent varying from 1.0 (no DRZ) to 3.0 (three shaft radii). Flow rates range from 0.003 to 2.93 m<sup>3</sup>/yr. Figure C-29 plots the calculated plume half-width for these flow rates assuming flow is directed into either the Magenta or the Culebra. For a continuous DRZ normalized radius of less than 1.5, the hydraulic disturbance caused by Culebra-Magenta interflow is minimal. Because the flow-rate and plume half-width are linearly correlated to the head difference, results from Figures C-28 and C-29 can be easily scaled to consider any head difference of interest.



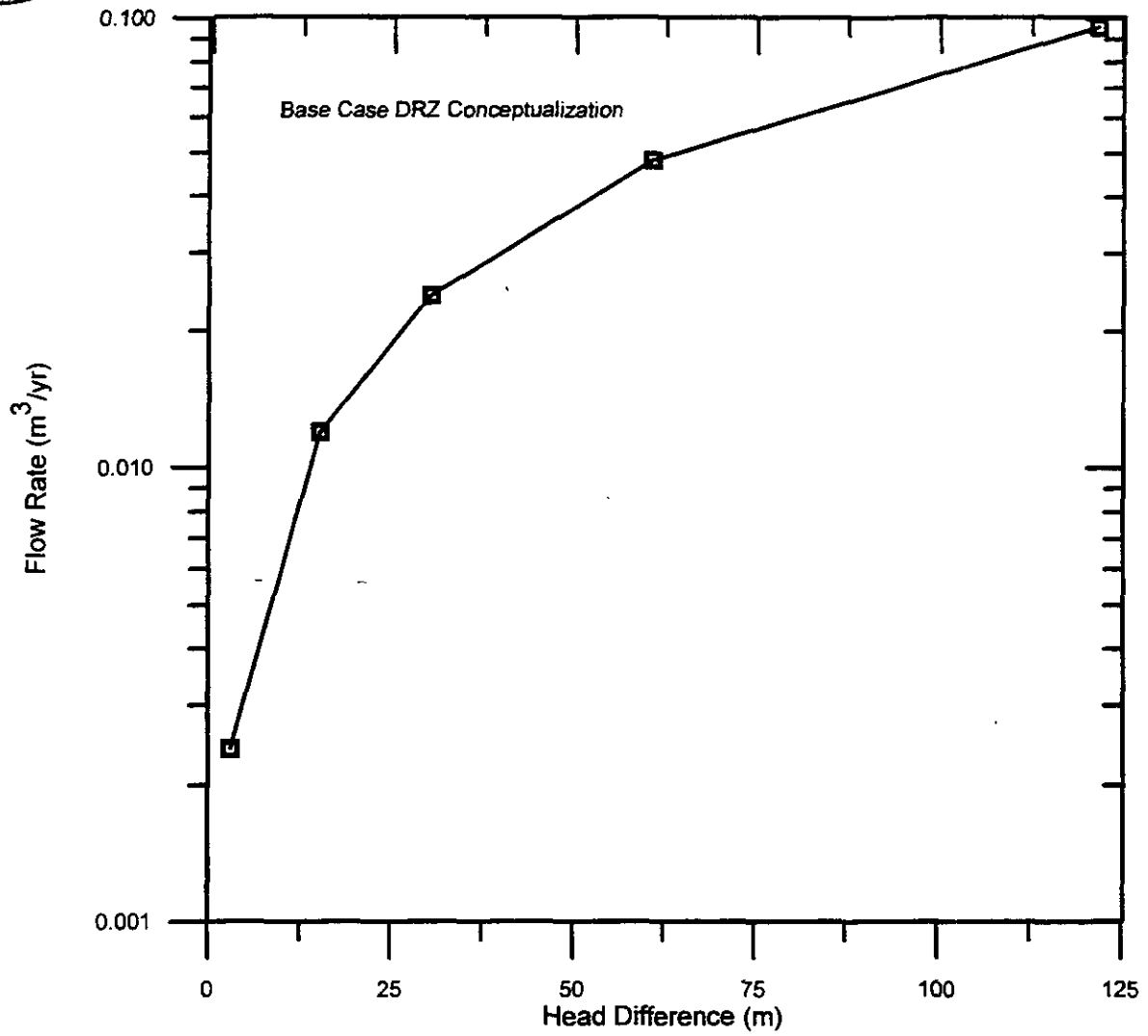
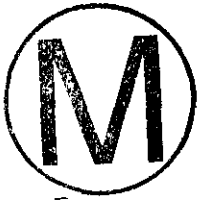


Figure C-26. Sensitivity of flow rate between Culebra and Magenta to head difference (base case).

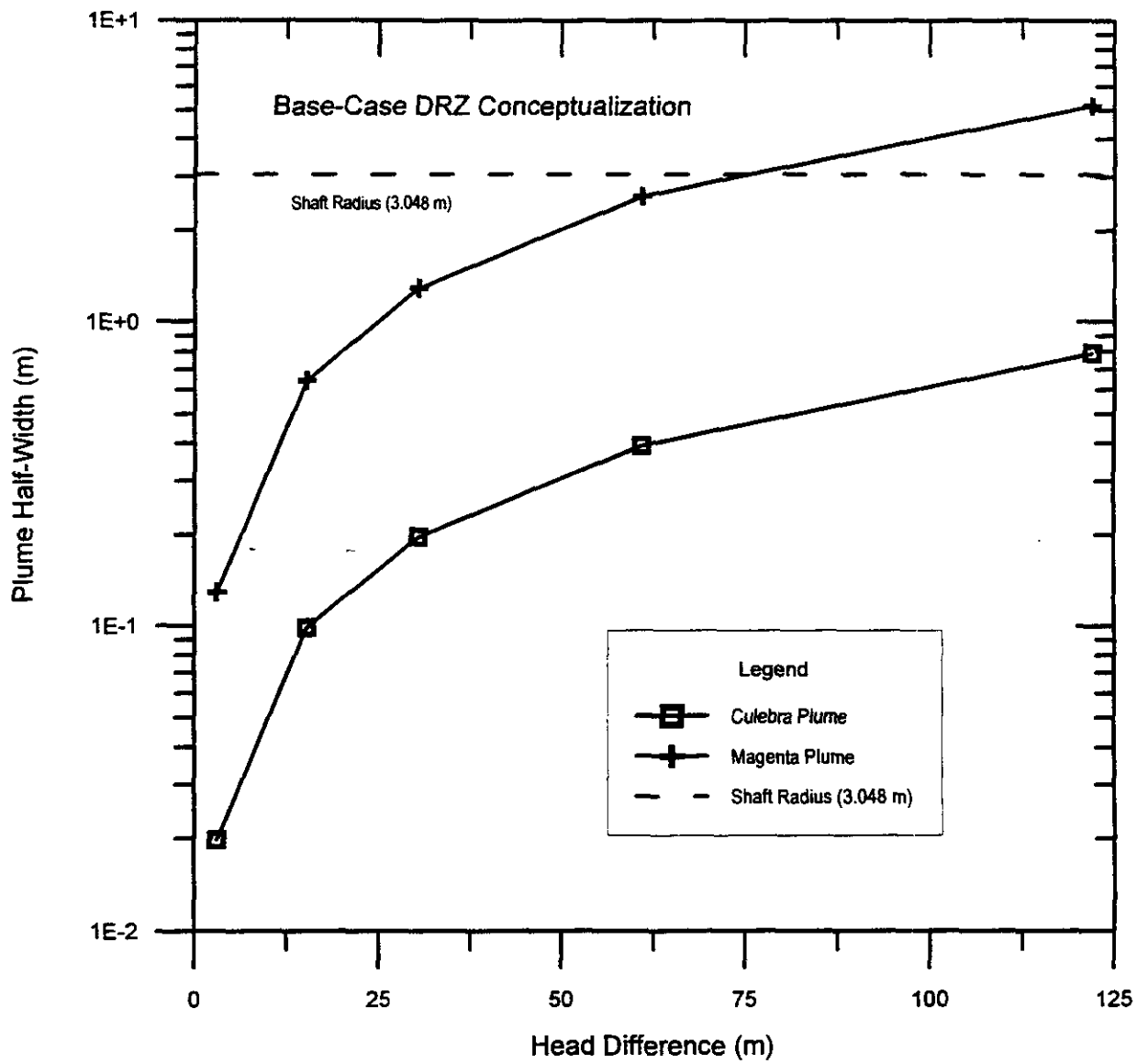
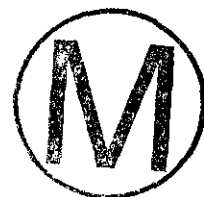


Figure C-27. Sensitivity of flow-field disturbance to head difference (base case).



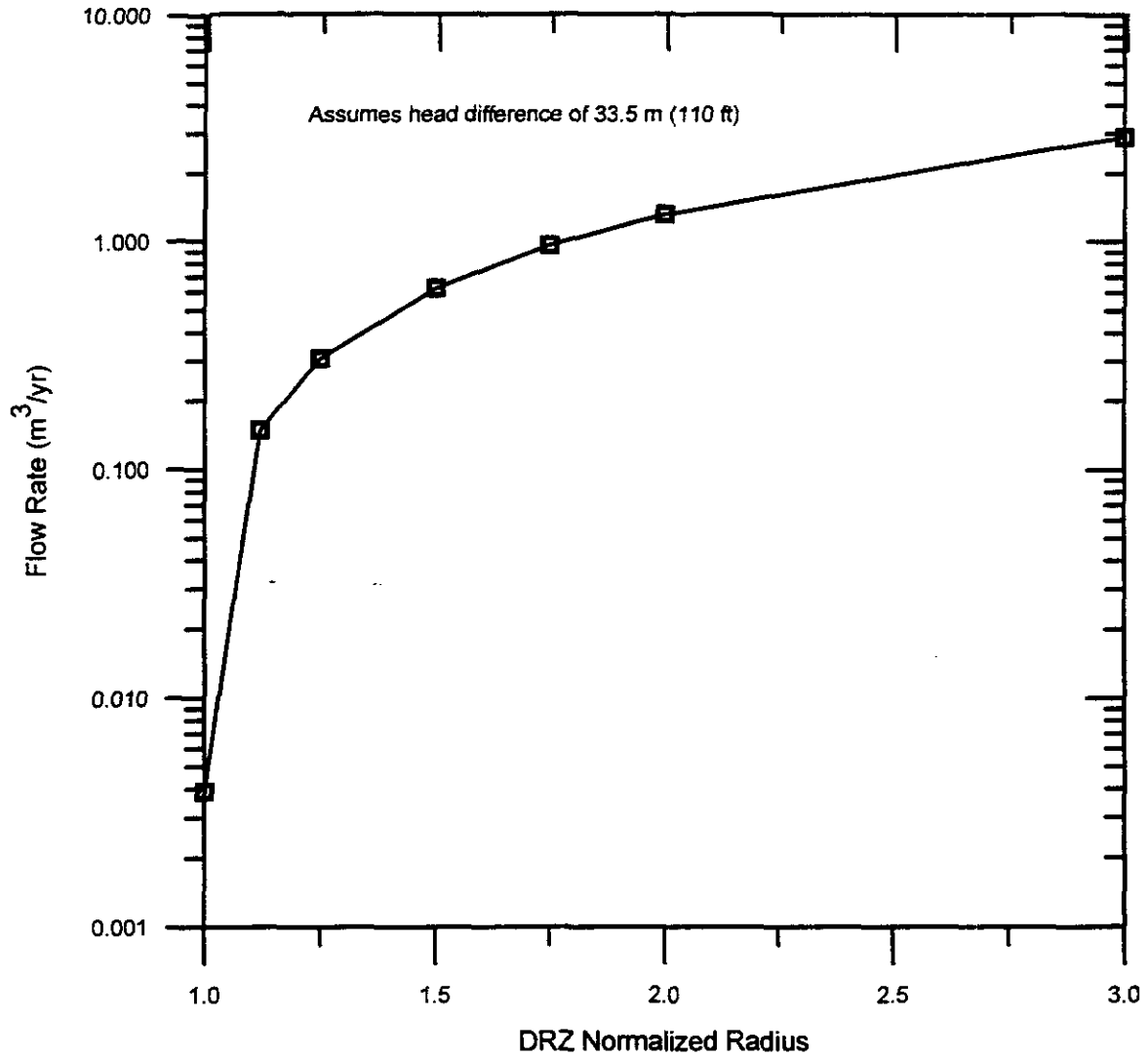
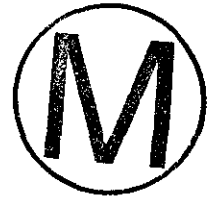


Figure C-28. Sensitivity of flow rate between Culebra and Magenta to DRZ radius (continuous DRZ).

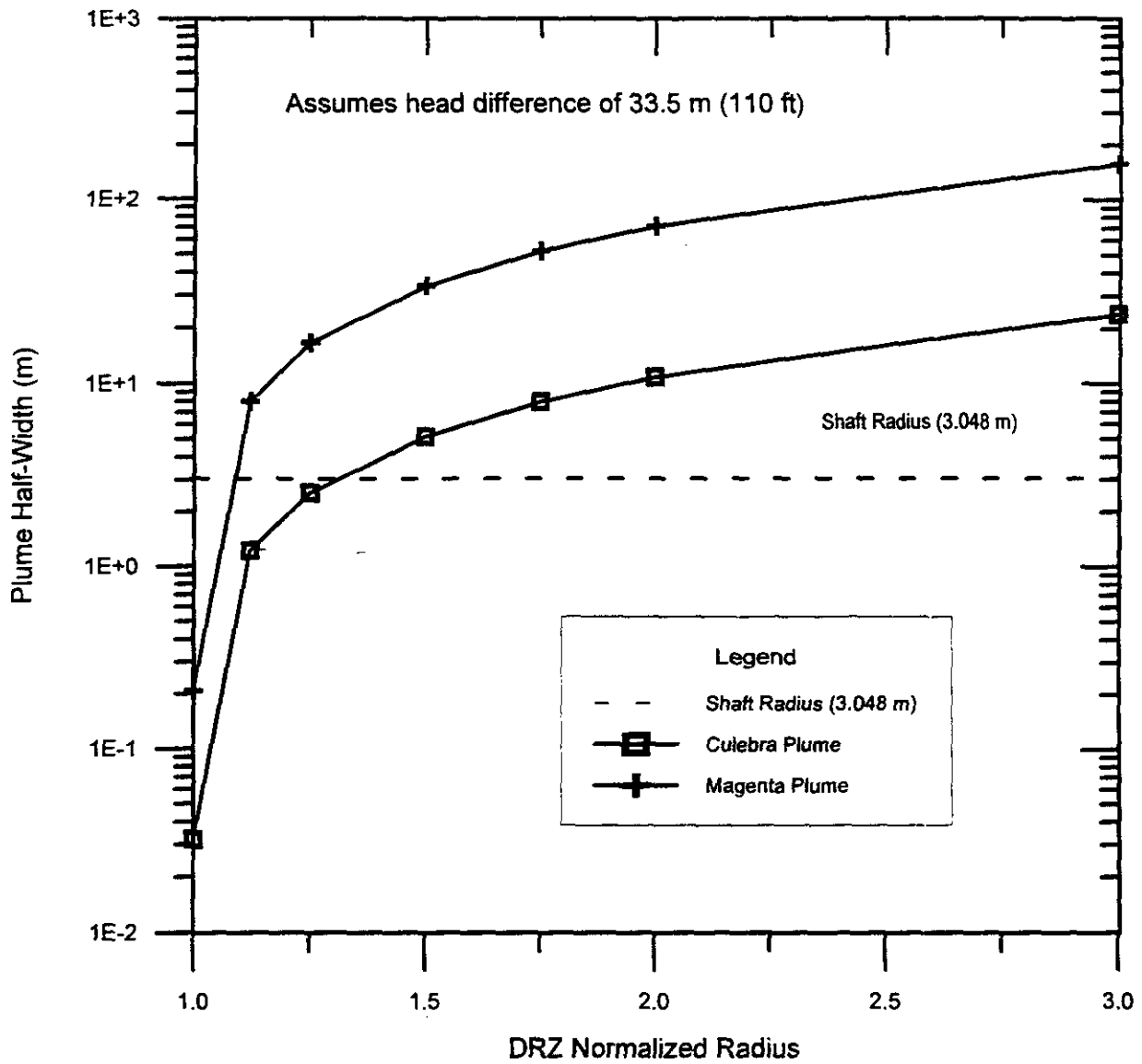


Figure C-29. Sensitivity of flow-field disturbance to DRZ radius (continuous DRZ).

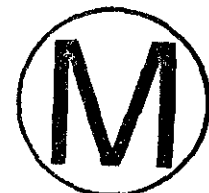




## C8. REFERENCES

- Avis, J.D., and G.J. Saulnier, Jr. 1990. Analysis of the Fluid-Pressure Responses of the Rustler Formation at H-16 to the Construction of the Air-Intake Shaft at the Waste Isolation Pilot Plant (WIPP) Site. SAND89-7067. Albuquerque, NM: Sandia National Laboratories. (Copy on file in the Sandia WIPP Central Files, Sandia National Laboratories, Albuquerque, NM [SWCF] as WPO24168.)
- Aziz, K., and A. Settari. 1979. Petroleum Reservoir Simulation. New York, NY: Elsevier Applied Science Publishers.
- Beauheim, R.L. 1987. Interpretations of Single-Well Hydraulic Tests Conducted at and Near the Waste Isolation Pilot Plant (WIPP) Site, 1983-1987. SAND87-0039. Albuquerque, NM: Sandia National Laboratories. (Copy on file in the SWCF as WPO27679.)
- Beauheim, R.L. 1989. Interpretation of H-11b4 Hydraulic Tests and the H-11 Multipad Pumping Test of the Culebra Dolomite at the Waste Isolation Pilot Plant (WIPP) Site. SAND89-0536. Albuquerque, NM: Sandia National Laboratories. (Copy on file in the SWCF as WPO24154.)
- Beauheim, R.L., G.J. Saulnier, Jr., and J.D. Avis. 1991. Interpretation of Brine-Permeability Tests of the Salado Formation at the Waste Isolation Pilot Plant Site: First Interim Report. SAND90-0083. Albuquerque, NM: Sandia National Laboratories. (Copy on file in the SWCF as WPO26003.)
- Beauheim, R.L., R.M. Roberts, T.F. Dale, M.D. Fort, and W.A. Stensrud. 1993. Hydraulic Testing of Salado Formation Evaporites at the Waste Isolation Pilot Plant Site: Second Interpretive Report. SAND92-0533. Albuquerque, NM: Sandia National Laboratories. (Copy on file in the SWCF as WPO23378.)
- Borns, D.J., and J.C. Stormont. 1988. An Interim Report on Excavation Effect Studies at the Waste Isolation Pilot Plant: The Delineation of the Disturbed Rock Zone. SAND87-1375. Albuquerque, NM: Sandia National Laboratories. (Copy on file in the SWCF as WPO24694.)
- Brinster, K.F. 1991. Preliminary Geohydrologic Conceptual Model of the Los Medaños Region Near the Waste Isolation Pilot Plant for the Purpose of Performance Assessment. SAND89-7147. Albuquerque, NM: Sandia National Laboratories. (Copy on file in the SWCF as WPO27781.)
- Brodsky, N.S. 1990. Crack Closure and Healing Studies in WIPP Salt Using Compressional Wave Velocity and Attenuation Measurements: Test Methods and Results. SAND90-7076. Albuquerque, NM: Sandia National Laboratories. (Copy on file in the SWCF as WPO25755.)
- Brooks, R.H., and A.T. Corey. 1966. "Properties of Porous Media Affecting Fluid Flow," Journal of the Irrigation and Drainage Division, Proceedings of the American Society of Civil Engineers (ASCE). Vol. 92, no. IR2, 61-88. (Copy on file in the SWCF.)

- Dale, T., and L.D. Hurtado. 1996. "WIPP Air-Intake Shaft Disturbed-Rock Zone Study," 4th International Conference on the Mechanical Behavior of Salt, Montreal, Quebec, June 17-18, 1996. SAND96-1327C. Albuquerque, NM: Sandia National Laboratories. (Copy on file in the SWCF.)
- Davies, P.B. 1991. Evaluation of the Role of Threshold Pressure in Controlling Flow of Waste-Generated Gas into Bedded Salt at the Waste Isolation Pilot Plant. SAND90-3246. Albuquerque, NM: Sandia National Laboratories. (Copy on file in the SWCF as WPO26169.)
- DOE (U.S. Department of Energy). 1995. Waste Isolation Pilot Plant Sealing System Design Report. DOE/WIPP-95-3117. Carlsbad, NM: U.S. Department of Energy, Waste Isolation Pilot Plant. (Copy on file in the SWCF as WPO29062.)
- DOE (U.S. Department of Energy). 1996. Compliance Certification Application for the Waste Isolation Pilot Plant. DOE/CAO-96-2184. Carlsbad, NM: U.S. Department of Energy, Carlsbad Area Office.
- Finley, N.C., and M. Reeves. 1981. SWIFT Self-Teaching Curriculum: Illustrative Problems to Supplement the User's Manual for the Sandia Waste-Isolation Flow and Transport Model (SWIFT). SAND81-0410. Albuquerque, NM: Sandia National Laboratories. (Copy on file in the SWCF as WPO30254.)
- Freeze, R.A., and J.A. Cherry. 1979. Groundwater. Englewood Cliffs, NJ: Prentice-Hall, Inc. (Copy on file in the Nuclear Waste Management Library, Sandia National Laboratories, Albuquerque, NM as GB1003.2 .F73 1979.)
- Gorham, E., R. Beauheim, P. Davies, S. Howarth, and S. Webb. 1992. "Recommendations to PA on Salado Formation Intrinsic Permeability and Pore Pressure for 40 CFR 191 Subpart B Calculations," Preliminary Performance Assessment for the Waste Isolation Pilot Plant, December 1992. Volume 3: Model Parameters. Sandia WIPP Project. SAND92-0700/3. Albuquerque, NM: Sandia National Laboratories. A-47 through A-66. (In Appendix A of SAND92-0700/3, which is on file in the SWCF as WPO23529.)
- Hansen, F.D., and K.D. Mellegard. 1979. Creep Behavior of Bedded Salt from Southeastern New Mexico at Elevated Temperature. SAND79-7030; RSI-0062. Albuquerque, NM: Sandia National Laboratories. (Copy on file in the SWCF as WPO27369.)
- Haug, A., V.A. Kelley, A.M. LaVenue, and J.F. Pickens. 1987. Modeling of Ground-Water Flow in the Culebra Dolomite at the Waste Isolation Pilot Plant (WIPP) Site: Interim Report. SAND86-7167. Albuquerque, NM: Sandia National Laboratories. (Copy on file in the SWCF as WPO28486.)
- Holcomb, D.J. 1988. "Cross-Hole Measurements of Velocity and Attenuation to Detect a Disturbed Zone in Salt at the Waste Isolation Pilot Plant," Key Questions in Rock Mechanics, Proceedings of the 29th U.S. Symposium, University of Minnesota, Minneapolis, MN, June 13-15, 1988. Eds. P.A. Cundall, R.L. Sterling, and A.M. Starfield. SAND87-3016C. Brookfield, VT: A.A. Balkema. 633-640. (Copy on file in the SWCF as WPO29992.)





- Holt, R.M., and D.W. Powers. 1990. Geologic Mapping of the Air Intake Shaft at the Waste Isolation Pilot Plant. DOE-WIPP 90-051. Carlsbad, NM: Westinghouse Electric Corporation. (Copy on file in the Nuclear Waste Management Library, Sandia National Laboratories, Albuquerque, NM.)
- Knowles, M.K., D. Borns, J. Fredrich, D. Holcomb, R. Price, D. Zeuch, T. Dale, and R.S. Van Pelt. 1996. "Testing the Disturbed Zone Around a Rigid Inclusion in Salt," 4th Conference on the Mechanical Behavior of Salt, Montreal, Quebec, June 17-18, 1996. SAND95-1151C. Albuquerque, NM: Sandia National Laboratories. (Copy on file in the SWCF.)
- Lambert, S.J. In preparation. Sources of Natural Brines at the Waste Isolation Pilot Plant and Implications for the Seal System. SAND94-0091. Albuquerque, NM: Sandia National Laboratories (Copy on file in the SWCF.)
- Lappin, A.R., R.L. Hunter, D.P. Garber, and P.B. Davies, eds. 1989. Systems Analysis, Long-Term Radionuclide Transport, and Dose Assessments, Waste Isolation Pilot Plant (WIPP), Southeastern New Mexico; March 1989. SAND89-0462. Albuquerque, NM: Sandia National Laboratories. (Copy on file in the SWCF as WPO24125.)
- LaVenue, A.M., T.L. Cauffman, and J.F. Pickens. 1990. Ground-Water Flow Modeling of the Culebra Dolomite. Volume I: Model Calibration. SAND89-7068/1. Albuquerque, NM: Sandia National Laboratories. (Copy on file in the SWCF as WPO24085.)
- Mercer, J.W. 1983. Geohydrology of the Proposed Waste Isolation Pilot Plant Site, Los Medanos Area, Southeastern New Mexico. Water-Resources Investigations Report 83-4016. Albuquerque, NM: U.S. Geological Survey, Water Resources Division. (Copy on file in the SWCF.)
- Parker, J.C., R.L. Lenhard, and T. Kuppasamy. 1987. "A Parametric Model for Constitutive Properties Regarding Multiphase Flow in Porous Media," Water Resource Research, Vol. 23, no. 4.
- Peterson, E.W., P.L. Lagus, and K. Lie. 1987. Fluid Flow Measurements of Test Series A and B for the Small Scale Seal Performance Tests. SAND87-7041. Albuquerque, NM: Sandia National Laboratories. (Copy on file in the SWCF as WPO24430.)
- Pruess, K. 1991. TOUGH2 - A General-Purpose Numerical Simulator for Multiphase Fluid and Heat Flow. LBL-29400. Berkeley, CA: Earth Sciences Division, Lawrence Berkeley Laboratory. (Copy on file in the SWCF.)
- Reeves, M., D.S. Ward, N.D. Johns, and R.M. Cranwell. 1986a. Theory and Implementation for SWIFT II, The Sandia Waste-Isolation Flow and Transport Model for Fractured Media, Release 4.84. SAND83-1159, NUREG/CR-3328. Albuquerque, NM: Sandia National Laboratories. (Copy on file in the SWCF as WPO28363.)
- Reeves, M., D.S. Ward, N.D. Johns, and R.M. Cranwell. 1986b. Data Input Guide for SWIFT II, The Sandia Waste-Isolation Flow and Transport Model for Fractured Media, Release 4.84. SAND83-0242, NUREG/CR-3162. Albuquerque, NM: Sandia National Laboratories. (Copy on file in the SWCF as WPO29686.)

- Reeves, M., D.S. Ward, P.A. Davis, and E.J. Bonano. 1987. SWIFT II Self-Teaching Curriculum: Illustrative Problems for the Sandia Waste-Isolation Flow and Transport Model for Fractured Media. SAND84-1586 Revision, NUREG/CR-3925. Albuquerque, NM: Sandia National Laboratories. (Copy on file in the SWCF as WPO30179.)
- Sandia WIPP Project. 1992. Preliminary Performance Assessment for the Waste Isolation Pilot Plant, December 1992. Volume 3: Model Parameters. SAND92-0700/3. Albuquerque, NM: Sandia National Laboratories. (Copy on file in the SWCF as WPO20910.)
- Saulnier, G.J., Jr., and J.D. Avis. 1988. Interpretation of Hydraulic Tests Conducted in the Waste-Handling Shaft at the Waste Isolation Pilot Plant (WIPP) Site. SAND88-7001. Albuquerque, NM: Sandia National Laboratories. (Copy on file in the SWCF as WPO24164.)
- Siegel, M.D., S.J. Lambert, and K.L. Robinson, eds. 1991. Hydrogeochemical Studies of the Rustler Formation and Related Rocks in the Waste Isolation Pilot Plant Area, Southeastern New Mexico. SAND88-0196. Albuquerque, NM: Sandia National Laboratories. (Copy on file in the SWCF as WPO25624.)
- Stormont, J.C. 1990. Summary of 1988 WIPP Facility Horizon Gas Flow Measurements. SAND89-2497. Albuquerque, NM: Sandia National Laboratories. (Copy on file in the SWCF as WPO24044.)
- Stormont, J.C., E.W. Peterson, and P.L. Lagus. 1987. Summary of and Observations About WIPP Facility Horizon Flow Measurements Through 1986. SAND87-0176. Albuquerque, NM: Sandia National Laboratories. (Copy on file in the SWCF as WPO24698.)
- Touloukian, Y.S., C.Y. Ho, W.R. Judd, and R.F. Roy. 1981. Physical Properties of Rocks and Minerals. McGraw-Hill/Cindas Data Series on Material Properties ; Vol. II-2. New York, NY: McGraw-Hill. (Copies available at Technical Library, Sandia National Laboratories, Albuquerque, NM and at Centennial Science and Engineering Library, University of New Mexico, Albuquerque, NM.)
- van Genuchten, M. Th. 1980. "A Closed-Form Equation for Predicting the Hydraulic Conductivity of Unsaturated Soils," Soil Science Society of America Journal. Vol. 44, no. 5, 892-898. (Copy on file in the SWCF.)
- Van Sambeek,, L.L., D.D. Luo, M.S. Lin, W. Ostrowski, and D. Oyenuga. 1993. Seal Design Alternatives Study. SAND92-7340. Albuquerque, NM: Sandia National Laboratories. (Copy on file in the SWCF as WPO23445.)
- Ward, D.S., M. Reeves, and L.E. Duda. 1984. Verification and Field Comparison of the Sandia Waste-Isolation Flow and Transport Model (SWIFT). SAND83-1154, NUREG/CR-3316. Albuquerque, NM: Sandia National Laboratories. (Copy on file in the SWCF as WPO29695.)
- Webb, S. W. 1996. Review of Two-Phase Characteristic Curves for Porous Media and Application to the WIPP. SAND93-3912. Albuquerque, NM: Sandia National Laboratories. (WPO# 37539)



WIPP PA. 1992-1993. Preliminary Performance Assessment for the Waste Isolation Pilot Plant, December 1992. SAND92-0700. Albuquerque, NM: Sandia National Laboratories. (Vol. 1 on file in the SWCF as WPO20762; Vol. 2 filed as WPO20805; Vol. 3 filed as WPO20910; Vol. 4 filed as WPO20958; Vol. 5 filed as WPO20929.)

